



TECHNISCHE
UNIVERSITÄT
WIEN

DISSERTATION

Quantification of the 3D elemental distribution using X-ray fluorescence

ausgeführt zum Zwecke der Erlangung des akademischen Grades eines
Doktors der technischen Wissenschaften
am

Atominstitut
der Technischen Universität Wien
Stadionallee 2
1020 Wien

unter der Anleitung von
Ao.Univ.Prof. Dipl.-Ing. Dr.techn. Christina Strel
und
Univ. Ass. Dipl.-Ing. Dr.techn. Dieter Ingerle

durch
Dipl.-Ing. Michael Iro, BSc.

Unterschrift Student

Unterschrift Betreuerin
Wien, am 12. Oktober 2023

Abstract

The quantitative interpretation of confocal Micro-X-ray fluorescence (CMXRF) measurements is still a challenge in current research, despite the techniques common use for the non-destructive investigation of the three-dimensional elemental distribution in samples from fields of study as diverse as geology, biology and cultural-heritage science. This thesis tries to tackle the challenge of quantitative interpretation of CMXRF measurements in three ways:

- **Investigation of the transmission properties of polycapillary half-lens optics:** Establishing the correct parameters of transmission intensity and beam shape of polycapillary half-lenses, commonly used in CMXRF setups, is vital for quantification. Experiments investigating those properties for three different polycapillary optics were conducted at the X-ray laboratory of the Atominstitut of the TU Wien and at the BAMline beamline at the BESSY II Synchrotron of the Helmholtz-Zentrum-Berlin. Experimental results and analytical models are compared to the existing simulation software *polycap* [1], to verify the use of the software in the simulation process. The measurement results are in good agreement with simulations and analytical models.
- **Development of a new fundamental Monte-Carlo ray-tracing software:** Different approaches for calculating line intensities for CMXRF measurements exist, using analytical models for the investigated confocal volume, or backward ray-tracing. *voxTrace* is a full forward Monte-Carlo ray-tracing software, to simulate energy-dispersive CMXRF spectra. This computationally expensive simulation is made feasible with the use of general purpose computation on graphics processing units (GPGPU). The software is implemented using the NVIDIA CUDA C++ interface. *voxTrace* traces the path of individual X-rays through a sample, simulating the possible interactions of X-rays with matter. The software was tested on a regular workstation with a sufficiently powerful GPU and the Vienna Scientific Cluster, a powerful high performance cluster. Simulated depth scans are in good agreement with measurement results.
- **Development and investigation of standard reference materials with a three dimensional structure of well-known composition:** Together with partners *S. Hampel* and *U. Fittschen* from TU Clausthal standard reference materials of well known composition with a three-dimensional structure were developed using different 3D-printing techniques. First attempts using a filament based 3D printer with metal-doped filaments were classified inadequate in terms of grain size of the doping material, as

well as roughness of the sample after investigations of the printed samples in a beamtime at the XRF beamline at the Elettra Sincrotrone in Trieste. A second set of SRM structures were printed with a resin-based 3D printer. The samples with a much lower doping concentration were investigated in a beamtime at the B16 Test Beamline at the Diamond Light Source. Area- and depth scans of the printed samples showed good properties in terms of roughness and grain size, making the printing method an interesting path to follow for the development of well classified SRMs with a 3D structure.

Kurzfassung

Die quantitative Interpretation von confokalen Mikro-Röntgenfluoreszenz (CMXRF) Messungen ist eine Herausforderung der aktuellen Forschung, trotz des weit verbreiteten Einsatzes der Methode für die zerstörungsfreie Untersuchung der dreidimensionalen elementaren Verteilung in Proben aus so unterschiedlichen Disziplinen wie Geologie, Biologie und Kunst- und Kulturwissenschaften. Diese Arbeit verfolgt die Lösung verschiedener Herausforderungen der quantitativen Interpretation von CMXRF Messungen auf drei Arten:

- **Untersuchung der Transmissionseigenschaften von polycapillaren Halb-Linsen:**
Die Bestimmung der korrekten Parameter für die Transmissionsintensität und die Strahlform von polykapillaren Halblinsen, die häufig in CMXRF-Anordnungen Verwendung finden, ist für die Quantifizierung von entscheidender Bedeutung. Am Röntgenlabor des Atominstutts der TU Wien und an der BAMline-Beamline am BESSY II-Synchrotron des Helmholtz-Zentrums Berlin wurden Experimente zur Untersuchung dieser Eigenschaften für drei verschiedene Polykapillaroptiken durchgeführt. Experimentelle Ergebnisse und analytische Modelle werden mit der bestehenden Simulationssoftware *polycap* [1] verglichen, um die Verwendung der Software im Simulationsprozess zu legitimieren. Die Messergebnisse stimmen gut mit den Simulationen und analytischen Modellen überein.
- **Entwicklung einer neuen fundamentalen Monte-Carlo Ray-tracing Software:**
Verschiedene Ansätze für die Berechnung von Linienintensitäten für CMXRF-Messungen sind derzeit verbreitet: analytische Modelle für das untersuchte konfokale Volumen oder rückwärts gerichtete Strahlenverfolgung. *voxTrace* ist eine vollständige vorwärts gerichtete Monte-Carlo-Strahlenverfolgungssoftware zur Simulation von energiedispersiven CMXRF-Spektren. Diese rechenintensive Simulation wird durch den Einsatz von Grafikprozessoren für allgemeine Berechnungen (GPGPU) ermöglicht. Die Software ist unter Verwendung der NVIDIA CUDA C++ Schnittstelle implementiert. *voxTrace* verfolgt den Weg einzelner Röntgenstrahlen durch eine Probe und simuliert die möglichen Wechselwirkungen der Röntgenstrahlen mit Materie. Die Software wurde auf einem üblichen Workstation PC mit ausreichend leistungsfähiger GPU und dem Vienna Scientific Cluster, einem leistungsstarken Hochleistungscluster, getestet. Die simulierten Tiefenscans stimmen gut mit Messergebnissen überein.
- **Entwicklung und Untersuchung von Standardreferenzmaterialien bekannter**

Zusammensetzung mit einer dreidimensionalen Struktur: Gemeinsam mit Partnern von der TU Clausthal *S. Hampel und U. Fittschen* wurden Standardreferenzmaterialien mit bekannter Zusammensetzung und dreidimensionaler Struktur unter Verwendung verschiedener 3D-Drucktechniken entwickelt. Erste Versuche mit einem filamentbasierten 3D-Drucker mit metalledierten Filamenten wurden nach Untersuchungen der gedruckten Proben in einer Strahlzeit an der XRF-Beamline am Elettra Synchrotrone in Triest als unzureichend in Bezug auf die Korngröße des Dotiermaterials sowie die Rauheit der Probe eingestuft. Ein zweiter Satz von SRM-Strukturen wurde mit einem harzbasierten 3D-Drucker gedruckt. Die Proben mit einer viel niedrigeren Dotierungskonzentration wurden in einer Strahlzeit an der B16 Test Beamline an der Diamond Light Source untersucht. Flächen- und Tiefenscans der gedruckten Proben zeigten gute Eigenschaften in Bezug auf Rauheit und Korngröße, was die Druckmethode zu einer interessanten Option für die Entwicklung gut klassifizierter SRMs mit einer 3D-Struktur macht.

Acknowledgements

I would like to thank Dr. Christina Streli, Dr. Peter Wobrauschek, Dr. Dieter Ingerle and Dr. Peter Kregsamer for their supervision and help during the work for my thesis. Also I want to thank all other members of the X-ray-physics group during my time at the Atominstitut of the TU Wien for their support and for the good working atmosphere in the group.

Further I want to thank all of the colleagues and friends who supported me and helped making my time at university a productive and enjoyable time. From this group I want to thank some people in particular: Felix Linhardt for his support in the first semesters and Andrea Tröstl for hours of help learning and encouragement in times of need.

I would like to thank TU Wien for financial support through its Innovative Projekte Funding Programme for the project GIP141000XRF.

I would like to thank Diamond Light Source for beamtime (proposal MM29861), and the staff of the beamline B16 for assistance with setting up the equipment and data collection.

I would like to acknowledge Elettra Sincrotrone Trieste for providing access to its synchrotron radiation facilities and thank Ilaria Carlomagno and Giuliana Aquilanti for assistance in using beamline XRF beamline.

I would like to acknowledge the HZB for providing beamtime for the proposal 202-09699. Special thanks to Martin Radtke and Ana Guilherme Buzanich for their support during the experiments.

The computational results presented have been achieved in part using the Vienna Scientific Cluster (VSC). Special thanks goes to to Markus Hickel, for his support in getting the code up and running.

Parts of this work have been published in the following publications:

- **M. Iro**, D. Ingerle, S. Hampel, U. Fittschen, V. Dhamgaye, O. Fox and C. Strel: *voxTrace: A Voxel-Based Monte-Carlo Ray-Tracing code for the simulation of X-ray fluorescence spectra*, *SoftwareX*, Volume 23, 101481 (2023); doi:10.1016/j.softx.2023.101481
- **M. Iro**, D. Ingerle, M. Radtke, A. Guilherme Buzanich, P. Kregsamer and C. Strel: *Investigation of polycapillary half lenses for quantitative confocal micro-X-ray fluorescence analysis*, *J. Synchrotron Rad.*, 29, 2022, p. 1376-1384; doi:10.1107/S1600577522009699
- D. Ingerle, J. Swies, **M. Iro**, P. Wobrauschek, C. Strel, and K. Hradil: *A monochromatic confocal micro-x-ray fluorescence (μ XRF) spectrometer for the lab.*, *Rev. Sci. Instrum.* 91, 123107 (2020); doi:10.1063/5.0028830

Conference contributions related to parts of this work have been presented as

Talks:

- **M. Iro**, D. Ingerle, P. Kregsamer, S. Hampel, U. Fittschen and C. Strel: *voxTrace: A voxel-based Monte-Carlo raytracing code for the simulation of confocal Micro-X-ray fluorescence measurements*, 72nd Annual Denver X-ray Conference 2023, Lombard, Illinois, U.S.A 2023, Invited Talk
- **M. Iro**, S. Hampel, D. Ingerle, P. Kregsamer, M. Radtke, A.G. Buzanich, I. Carlomagno, G. Aquilanti, O. Fox, K. Sawhney, U. Fittschen and C. Strel: *Steps towards the quantitative interpretation of confocal micro-X-ray fluorescence measurements (QCMXRF)*, 71st Annual Denver X-ray Conference 2022, Washington D.C., U.S.A 2022, Invited Talk

- **M. Iro**, S. Hampel, D. Ingerle, P. Kregsamer, M. Radtke, A.G. Buzanich, I. Carlo-magno, G. Aquilanti, O. Fox, K. Sawhney, U. Fittschen and C. Strel: *Steps towards quantitative confocal micro X-ray fluorescence analysis (QCMXRF)*, European Conference on X-ray Spectrometry, Bruges, Belgium, 2022, Talk
- D. Ingerle, **M. Iro**, J. Swies, K. Hradil, P. Wobrauschek and C. Strel: *A monochromatic confocal micro X-ray Fluorescence (μ XRF) spectrometer using polycapillaries for the lab*, European Conference on X-ray Spectrometry, Bruges, Belgium, 2022, Talk

Posters:

- **M. Iro**, D. Ingerle and C. Strel: *jGiXa 2.0 and further advances in GIXA Software*, European Conference on X-ray Spectrometry, Bruges, Belgium, 2022
- **M. Iro**, D. Ingerle, M. Radtke, K. Tsuji, S. Hampel, U. Fittschen and C. Strel: *Investigation of the transmission properties of a polycapillary half-lens and their effect on quantification for CMXRF*, 70th Annual Denver X-ray Conference 2021, Online

Contents

1	Introduction	1
2	X-ray fluorescence analysis (XRF)	2
2.1	X-ray sources	2
2.1.1	X-ray tubes	3
2.1.2	Synchrotron sources	5
2.2	X-ray optics	6
2.2.1	Monochromators	7
2.2.2	Capillary optics	9
2.3	Interactions of photons with matter	11
2.3.1	Photoelectric effect	12
2.3.2	Rayleigh scattering	14
2.3.3	Compton scattering	15
2.4	X-ray detectors	16
2.5	Confocal micro X-ray fluorescence analysis (CMXRF)	17
2.6	Quantitative X-ray fluorescence analysis	18
3	State of the art	20
4	voxTrace	23
4.1	Algorithm	24
4.2	Implementation	29
4.3	How to use voxTrace	31
5	Experimental work	36
5.1	A monochromatic confocal micro-x-ray fluorescence spectrometer	36
5.2	Investigation of polycapillary half-lenses	42
5.2.1	Knife-edge scans	42
5.2.2	Images and Pinhole-Scans	55
5.2.3	Transmission	64
5.3	Investigation of standard reference materials with a three-dimensional structure	67
5.3.1	Filament based standard reference materials	67
5.3.2	Resin based standard reference materials	73
5.3.3	Simulation of the measured results with voxTrace	81
6	Conclusion and Outlook	83
	References	85

1 Introduction

Micro X-ray fluorescence analysis (μ XRF) and confocal micro X-ray fluorescence analysis (CMXRF) using polycapillary optics are well established techniques for the investigation of the 2D- and 3D-elemental composition of samples. Polycapillary optics, first developed by Kumakhov in the 1990s [2, 3], are used to limit the irradiated area of the sample. Investigated samples reach from the fields of geology [4, 5], biology [6], failure analysis of industrial products [7] to cultural heritage science [8] and the investigation of paintings [9]. Confocal setups can be realized limiting the field of vision of the detector in an XRF setup with a second polycapillary optic. Thus a small volume irradiated and visible to the detector can be investigated, making a three-dimensional elemental mapping of the sample possible. While the technique is commonly used for imaging purposes, quantitative interpretations of CMXRF measurements are still a challenge in current research.

This is due to the complex nature of CMXRF setups. Energy dependent transmission properties of polycapillary half-lens optics have to be considered as well as absorption and scattering effects inside often inhomogeneous sample. Common approaches for the quantitative interpretation of CMXRF measurements include analytical estimations for the energy dependent confocal volume and transmission properties of polycapillary optics and Monte-Carlo ray-tracing approaches using variance reduction techniques (see 3). To fully include second and higher order effects [10] inside the sample a full "brute force" ray-tracing approach inside the sample and the capillary optic [11, 12, 1] would be interesting. The recent developments in hardware buildt for ray-tracing, namely graphics processing units (GPUs) make an implementation of such an approach with reasonable simulation times feasible.

Furthermore the lack of suitable generally applicable standard reference materials of well known composition and with a three-dimensional structure complicates the fast validation of quantitative CMXRF measurements. The development and production of standard reference materials of similar composition to the sample is a difficult and often time-consuming procedure. The use of 3D printing for the development of suitable standard reference materials with a well-defined three-dimensional structure could address this challenge.

2 X-ray fluorescence analysis (XRF)

X-ray fluorescence analysis (XRF) is a commonly employed method for the non-destructive qualitative and quantitative investigation of the elemental composition of samples from various fields of study (geology, biology, cultural heritage science, etc.). The effect of characteristic radiation, see below, is utilized to gain knowledge, of the elemental composition of a sample. Depending on the properties of the sample and the desired information about it, different experimental setups are used. As the explanation of the numerous experimental realizations of XRF setups (TXRF, GIXRF, GEXRF, etc.) applicable for different measurement problems would go beyond the scope of this thesis, the following section only gives a short overview over the necessary fundamental processes and involved technical equipment necessary for understanding CMXRF measurements.

2.1 X-ray sources

Typically, X-rays can be produced as *bremsstrahlung*, by deflecting charged particles or as *characteristic radiation*, the radiation emitted during the transition of an outer-shell electron of a previously ionized atom to a lower energy state.

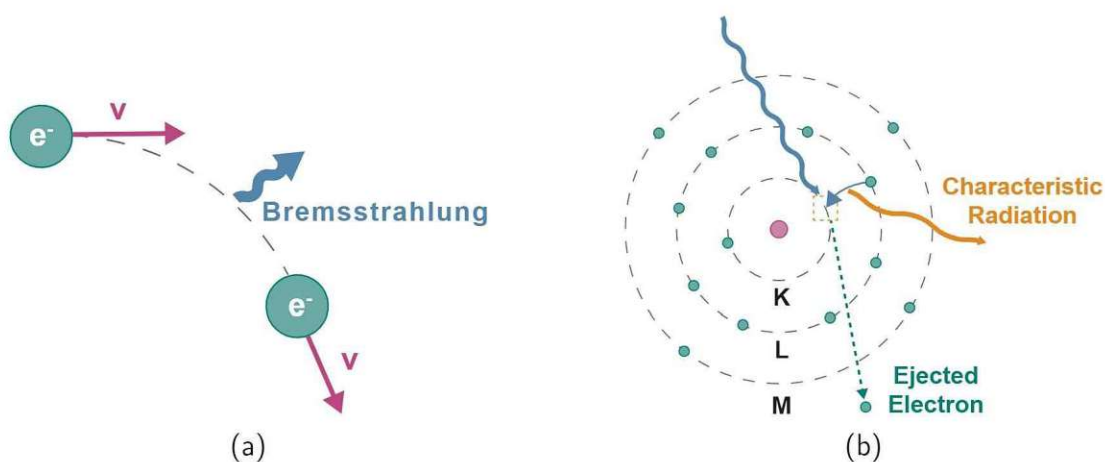


Figure 1: Schematic drawing of the generation of (a) Bremsstrahlung and (b) Characteristic radiation

While *bremsstrahlung* is emitted as a continuous energy spectrum *characteristic radiation* has clearly defined lines, with an energy characteristic to the energy gap between the involved bound electron states of the emitting atom.

Historically nomenclature for characteristic X-ray lines was introduced by Siegbahn, but later replaced by the more systematic IUPAC nomenclature [13], where a line is characterized by the shells between which the electron transitions, e.g. K-L₃ for a photon emitted during the transition of an electron from the L₃ orbital to the K shell of an atom. Nevertheless, as Siegbahn notation is still commonly used in X-ray physics it is beneficial to know that typically used lines K_α corresponds to the transition between K and L shells (K-L₃ and K-L₂) and K_β corresponds to the transitions between K shell and the shells M and N (K-M₃, K-N₃, K-N₂, K-M₂, K-N₅, K-N₄, K-M₅ and K-M₄). As energies of these transitions are very close they are often hard to discern, and thus treated as one line K_α or K_β.

X-ray sources are usually characterized by the energy spectrum they produce, i.e. the energy dependent radiation **intensity** $I(E)$, measured in $\frac{\text{photons}}{\text{s}}$. Further important parameters are the **spectral flux** $\phi(E)$

$$\phi(E) = \frac{I(E)}{0.1\% \text{ energy bandwidth}} = \frac{\text{photons}}{\text{s} \cdot 0.1\% \cdot \frac{\Delta E}{E}} \quad (1)$$

the **brightness** $\phi(E, \psi, \theta)$, considering the angular divergence in both direction ψ and θ

$$\phi(E, \psi, \theta) = \frac{\phi(E)}{\text{beam divergence}} = \frac{\text{photons}}{\text{s} \cdot 0.1\% \cdot \frac{\Delta E}{E} \cdot \text{mrad}^2} \quad (2)$$

and introducing the size of the source the **brilliance** $\phi(E, \psi, \theta, x, z)$

$$\phi(E, \psi, \theta, x, z) = \frac{\phi(E, \psi, \theta)}{\text{source size}} = \frac{\text{photons}}{\text{s} \cdot 0.1\% \cdot \frac{\Delta E}{E} \cdot \text{mrad}^2 \cdot \text{mm}^2} \quad (3)$$

with x and z being the horizontal and vertical dimensions of the source. A high brilliance, i.e. a small spot size, small angular divergence and high photon flux can be considered ideal for many XRF measurements.

2.1.1 X-ray tubes

Classical X-ray tubes (see figure 2) utilize both previously mentioned effects, *bremstrahlung* and *characteristic radiation*, for the production of X-rays. Electrons are accelerated towards a water cooled anode inside an evacuated cylinder. Decelerating electrons produce a continuous spectrum (*bremstrahlung*), while atoms from the anode material are first ionized by the electrons and later relax into a lower energy state, emitting *characteristic radiation* with an energy characteristic to the anode material.

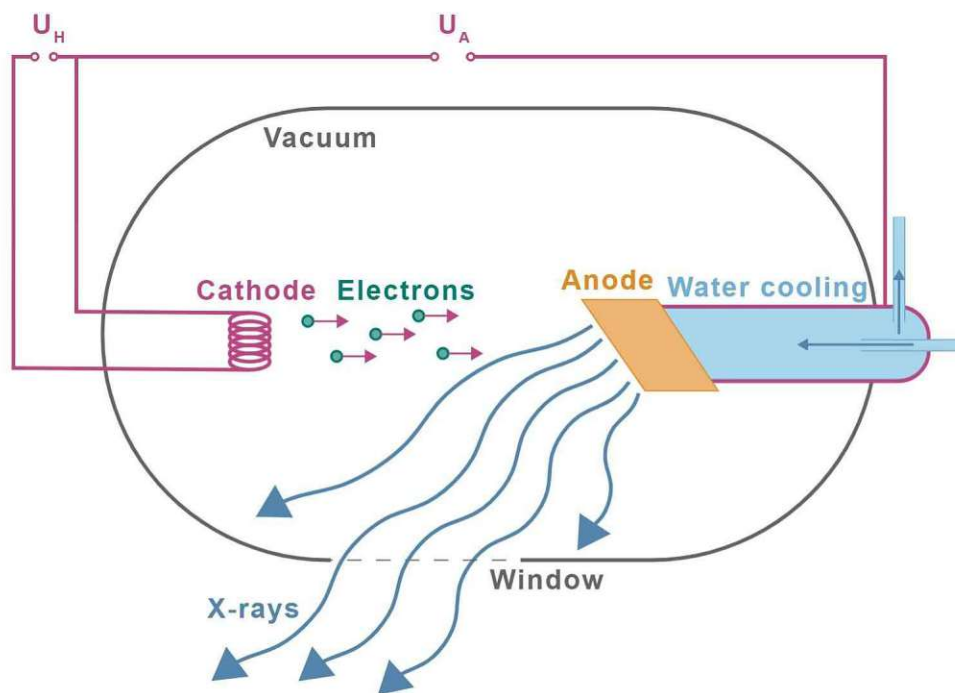


Figure 2: Schematic drawing of an X-ray tube. Electrons, emitted by a cathode, are accelerated towards a water-cooled anode inside an evacuated cylinder, producing X-rays upon impact.

The spectral distribution of the emitted radiation therefore consists of a continuous *bremstrahlung* part and *characteristic peaks*, as shown in figure 3.

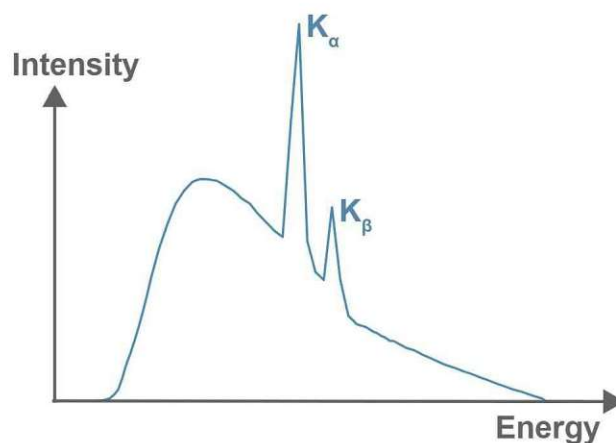


Figure 3: Shape of a typical energy dispersive X-ray tube spectrum, consisting of a continuous part and characteristic lines of the anode material.

While technical advances have been made to create X-ray tubes with higher brightness, such as liquid metal jet sources [14] or lower power, classical X-ray tubes are still in heavy use in X-ray labs around the world, due to their relatively low cost and versatile applicability in various setups.

2.1.2 Synchrotron sources

Synchrotrons utilize *bremsstrahlung* to produce X-rays. Magnetic and Electric fields are applied to accelerate charged particles (typically electrons), towards relativistic energies on a circular path (storage ring), emitting X-rays tangential to the direction of motion. Such typical *bending magnet* sources are supplemented with more advanced insertion devices such as *undulators*, *wigglers* and *free electron lasers (FEL)*, at most modern synchrotron facilities. Insertion devices use alternating magnetic fields to force the charged particles on a "slalom" trajectory (see figure 4), thus changing the spectral and spatial distribution of the emitted radiation.

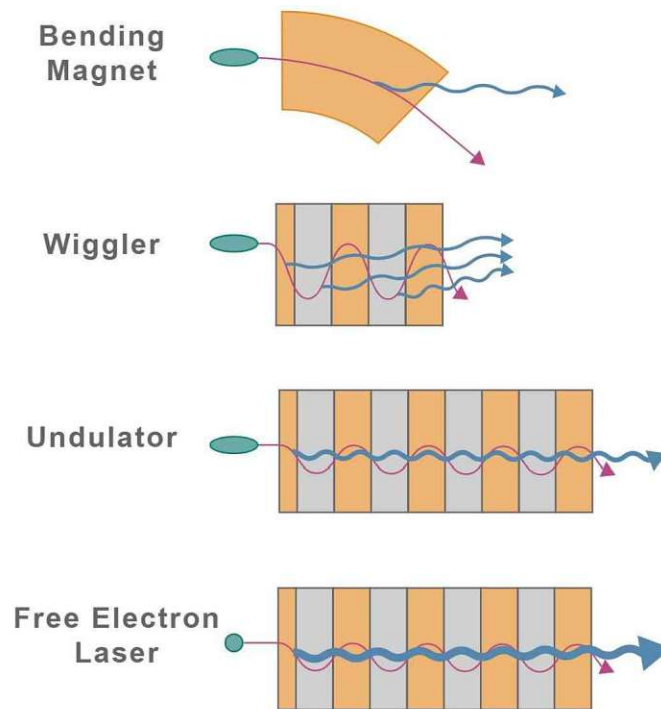


Figure 4: Schematic drawing of different synchrotron radiation insertion devices.

Synchrotron sources are in high demand due to the high brilliance of the produced beam (i.e. large photon flux, small divergence), the wide energy range of the radiation, as well as the high level of polarisation. Figure 5 shows a comparison of the brilliance of different types

of X-ray sources. One quickly sees that synchrotron sources, especially ones with modern insertion devices such as wigglers, undulators or free-electron lasers supersede classical X-ray tubes by several orders of magnitude. Thus synchrotron sources are especially important for the measurement of small samples, samples with low element concentration or other measurement problems requiring a highly brilliant beam.

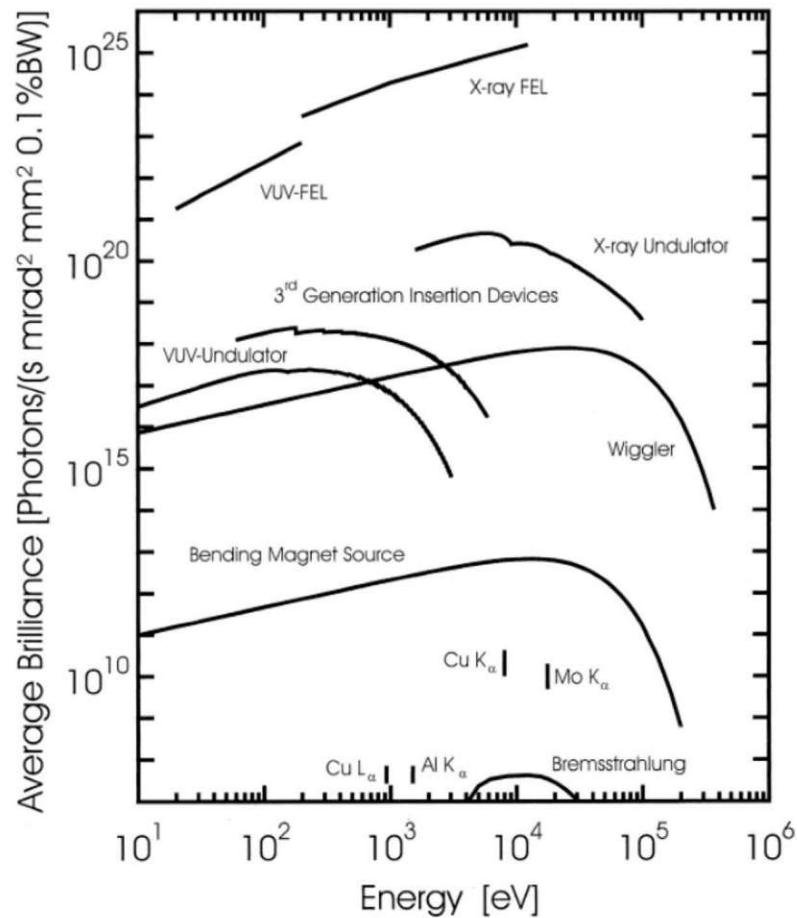


Figure 5: Comparison of the brilliance of different X-ray sources taken from [15].

2.2 X-ray optics

The properties of the beam (focal spot size, parallel beam, monochromatic) created with X-ray tubes and synchrotron sources can further be manipulated to suit the needs of the specific experiment using X-ray optics.

2.2.1 Monochromators

Monochromatic radiation makes the quantification process of XRF measurements much easier, due to a clearly defined excitation energy. The most common optics for monochromatisation rely on *Bragg's law* for constructive interference for the monochromatisation of X-rays. *Bragg's law* can be written as

$$n \cdot \lambda = 2 \cdot d \cdot \sin(\theta) \quad (4)$$

with n being a positive integer called the order of reflection, λ the wavelength of the radiation, d the distance between different planes of reflection and θ the angle of incidence of the beam. In crystal monochromators incoming radiation is reflected by the different atomic layers of the crystal structure (see figure 6). Radiation fulfilling *Bragg's law* is enhanced through constructive interference, while the rest of the radiation is "filtered" through destructive interference. Thus a specific energy of a polychromatic spectrum can be chosen, with crystals with different d and different angles of reflection θ .

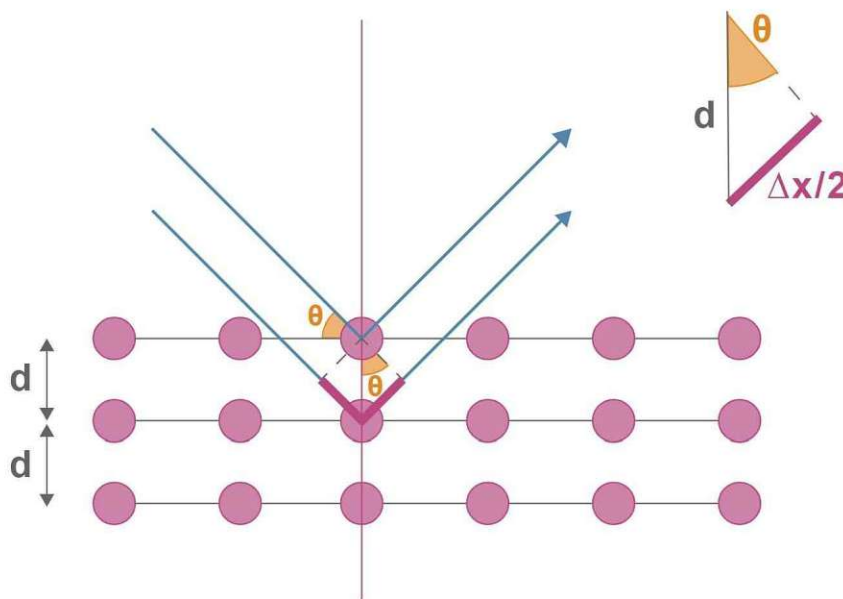


Figure 6: Schematic drawing of a crystal monochromator, with a distance d between different planes of reflection.

Multilayer monochromators use a periodic arrangement of heavy element (high atomic number Z) layers and light element (low atomic number Z) layers, with a fixed layer depth d (see figure 7). Incoming X-rays are reflected at the interface of light-element to heavy-element layer. Again rays fulfilling *Bragg's law* interfere constructively, and thus are enhanced.

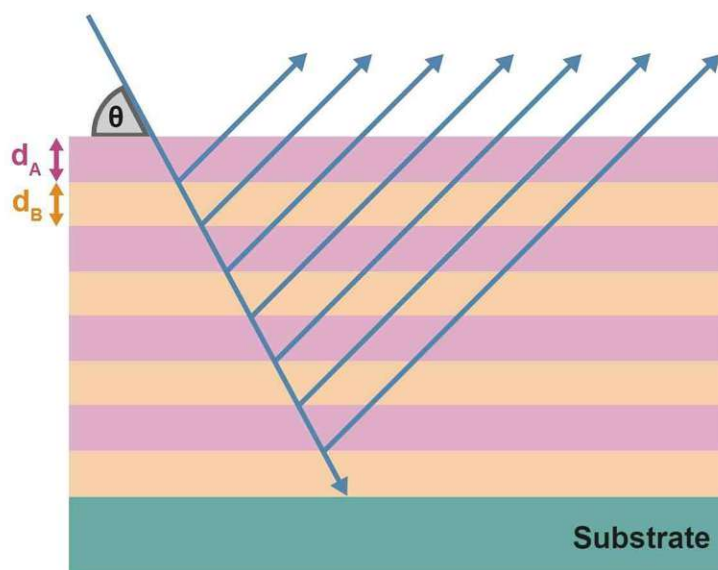


Figure 7: Schematic drawing of a multilayer monochromator with layer depths d_A of low- Z layers and d_B of high- Z layers.

Typically one has to choose between high energy resolution (small energy bandwidth) achieved with crystal monochromators and high photon flux achieved with multilayer monochromators[16].

Parallel monochromatic beams can be realized using parabolically shaped multilayers, positioning the spot of the X-ray source in the focal point of the parabola (see figure 8).

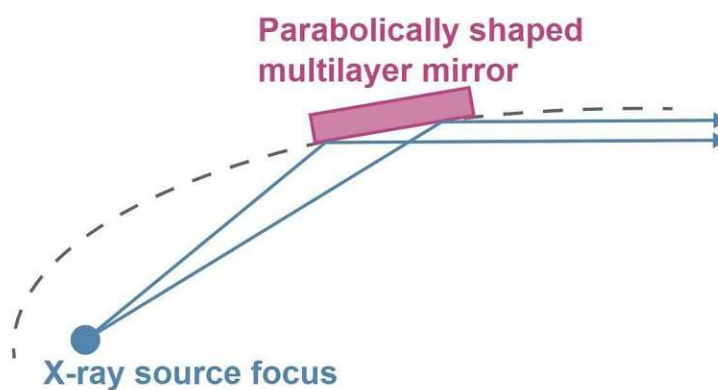


Figure 8: Schematic drawing of a parabolically shaped multilayer mirror (parallel beam monochromator), with the focal spot of the X-ray source in the focal point of the parabola.

2.2.2 Capillary optics

Glass capillaries with a very smooth inner surface can be used to focus divergent beams. Figure 9 shows the ray path of X-rays in a monicapillary. For applications in a given distance from the X-ray source the intensity in the focal spot of the capillary optic is typically much larger than for a spot of the same size produced with a collimator instead of the capillary optic.

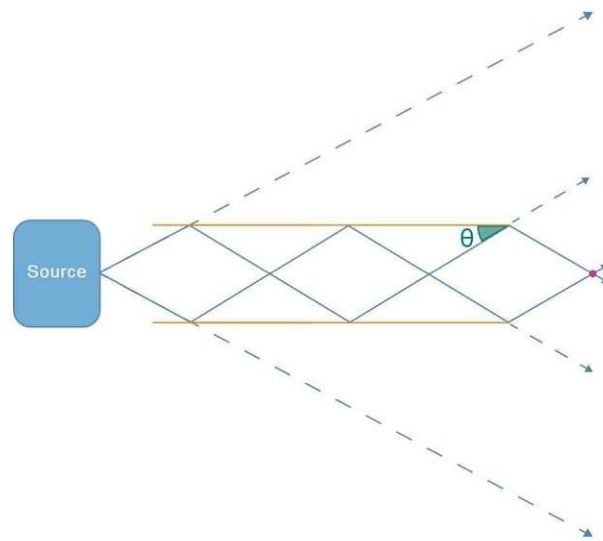


Figure 9: Schematic drawing of a monicapillary optic.

The functionality of capillary optics relies on the principle of total external reflection of X-rays. The complex refractive index n of X-rays with matter can be written as[17]

$$n = 1 - \delta - i\beta \quad (5)$$

with

$$\beta = \frac{\lambda}{4\pi} \left(\frac{\mu}{\rho} \right) \rho \quad (6)$$

being a measure of the attenuation, where λ is the wavelength of the radiation, $\left(\frac{\mu}{\rho} \right)$ the mass attenuation coefficient and ρ the density [17]. The real part δ of n can be written as

$$\delta = \frac{N_A}{2\pi} r_{el} \frac{1}{A} [f_0 + f(\lambda)] \rho \lambda^2 \quad (7)$$

with N_A being Avogadro's Number, r_{el} the classical electron radius, A the atomic mass, f_0 a quantity equal to the atomic number Z for X-rays, $f(\lambda)$ a correction term for the

absorption edges, λ the wavelength of the radiation and ρ the density of the material[17]. Total external reflection is possible for small angles θ as any medium is optically less dense than vacuum and any solid optically less dense than air for X-rays[17]. The critical angle θ_C for total reflection can be written as

$$\theta_C \approx \sqrt{2\delta} \approx \frac{1.651}{E} \sqrt{\frac{Z}{A}\rho} \quad (8)$$

with E being the energy of the radiation in keV, Z the atomic number, A the atomic mass and ρ the density of the material in $\frac{g}{cm^3}$ to result in a θ_C in $^\circ$ [17].

The intensity in the focal spot can be further improved with the use of many (hundreds of thousands) very small capillaries focused to the same point. Such polycapillary optics were first developed by Kumakhov in the 1990s [2, 3]. Polycapillary full lenses can be used to focus a divergent beam to a small spot in the micrometer regime (see figure 10).

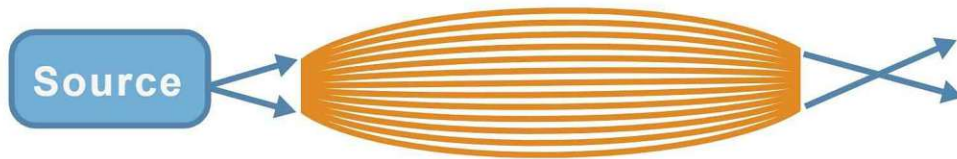


Figure 10: Schematic drawing of a polycapillary full-lens

Polycapillary half-lenses focus a parallel beam to a small spot, or alternatively parallelize a divergent beam(see figure 11).

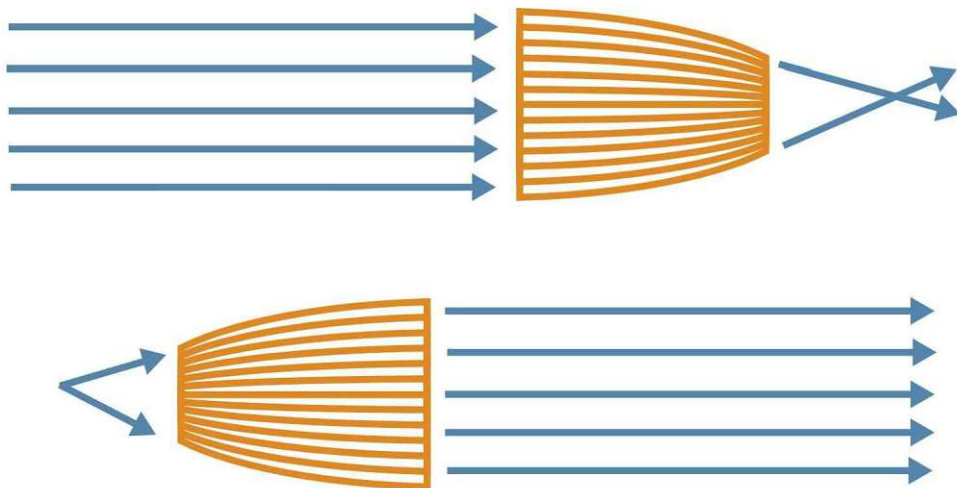


Figure 11: Schematic drawing of a polycapillary half-lens

Further properties of polycapillary optics are discussed in section 5.2.

2.3 Interactions of photons with matter

As interactions of radiation with nuclei, such as pair production, are only relevant for high energies, usually outside the range of typical XRF experiments, the following section only, gives an overview of interactions of photons with atomic shells. A more exhaustive overview over the possible interactions of photons with matter can be found in [18]. The fundamental parameters discussed in this section (cross sections, yields, differential cross sections) are available in *xraylib: a library for interactions of X-rays with matter* with APIs to many common programming languages[19, 20].

The attenuation of X-rays by matter can be described by *Beer's law*

$$I_x = I_0 \cdot e^{-\mu \cdot \Delta x} \quad (9)$$

with I_x being the intensity of the attenuated beam, I_0 the intensity of the primary beam, μ the *linear attenuation coefficient* of the material and Δx the path of the X-rays inside the material.

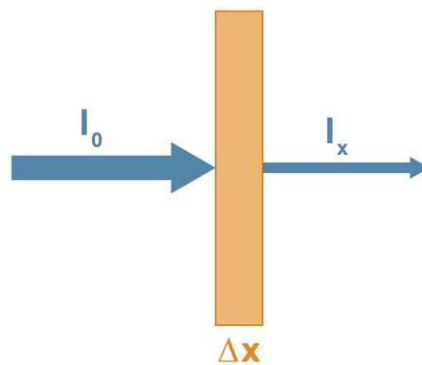


Figure 12: Depiction of Beer's law. X-rays with an intensity I_0 are attenuated by a massive sample with thickness Δx .

The *linear attenuation coefficient* μ can be written as [18]

$$\mu \left[\frac{1}{cm} \right] = \sigma_{tot} \left[\frac{cm^2}{atom} \right] \cdot \rho \left[\frac{g}{cm^3} \right] \cdot \frac{N_A}{A} \left[\frac{atoms}{g} \right] \quad (10)$$

where σ_{tot} is the *total attenuation cross section*, ρ the density, N_A Avogadro's Number and

A the atomic mass.

The total attenuation cross section σ_{tot} can further be written as the sum of cross sections from three effects

$$\sigma_{tot} = \tau + \sigma_{Rayleigh} + \sigma_{Compton} \quad (11)$$

with τ being the photoionization cross section, $\sigma_{Rayleigh}$ the cross section for Rayleigh scattering and $\sigma_{Compton}$ the cross section for Compton scattering. Figure 13 shows that while for low energies scattering is dominantly elastic (Rayleigh scattering), inelastic scattering (Compton scattering) becomes more relevant for higher energies. In the typical XRF energy regime (1 - 40 keV) photoionization is the dominant effect, by several orders of magnitude (note the logarithmic scale of figure 13).

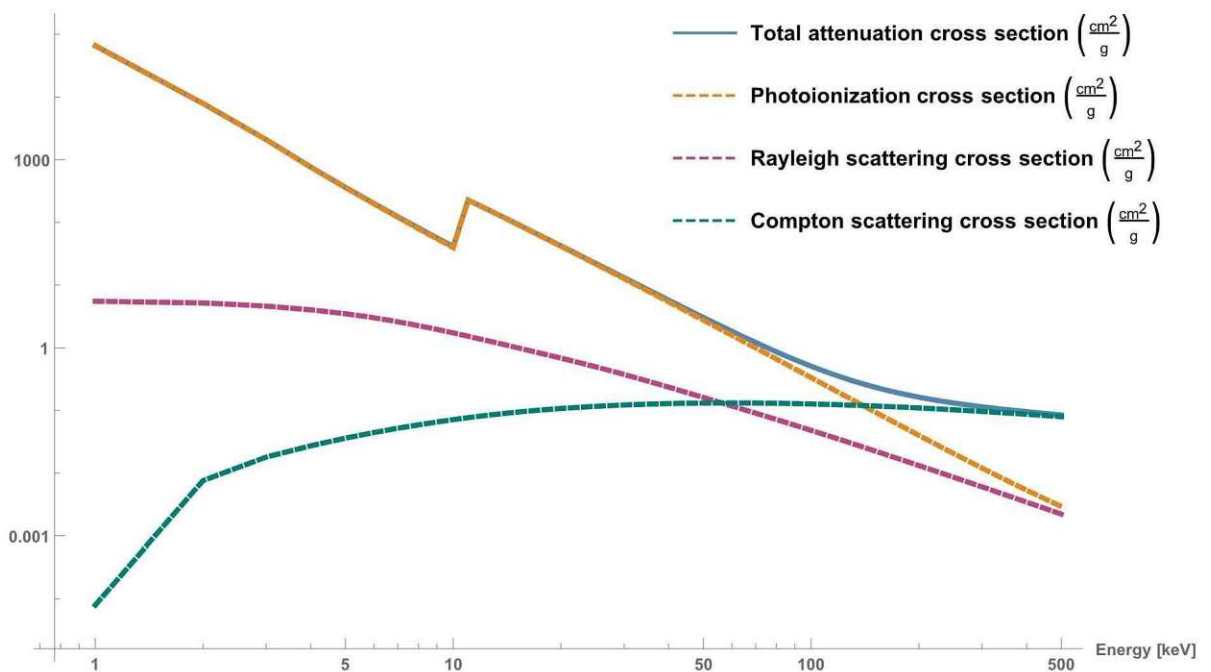


Figure 13: Cross sections of the different possible interactions for Zn. Created with data from *xraylib*[19, 20].

2.3.1 Photoelectric effect

The absorption of an incoming X-ray photon and subsequent ejection of a shell electron is called photoelectric effect. The probability for such an interactions is given by the photoion-

ization cross section $\tau(E, Z)$, which is dependent of the atomic number Z and the energy of the X-ray photon E .

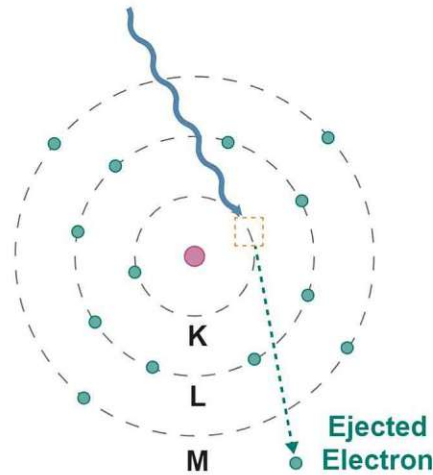


Figure 14: Schematic drawing of the photoelectric effect. A bound electron of an atom is ejected, absorbing an incoming photon.

Atoms excited this way can relax in to a lower energy state via either the emission of characteristic radiation or the ejection of an Auger-Meitner electron (see figure 15).

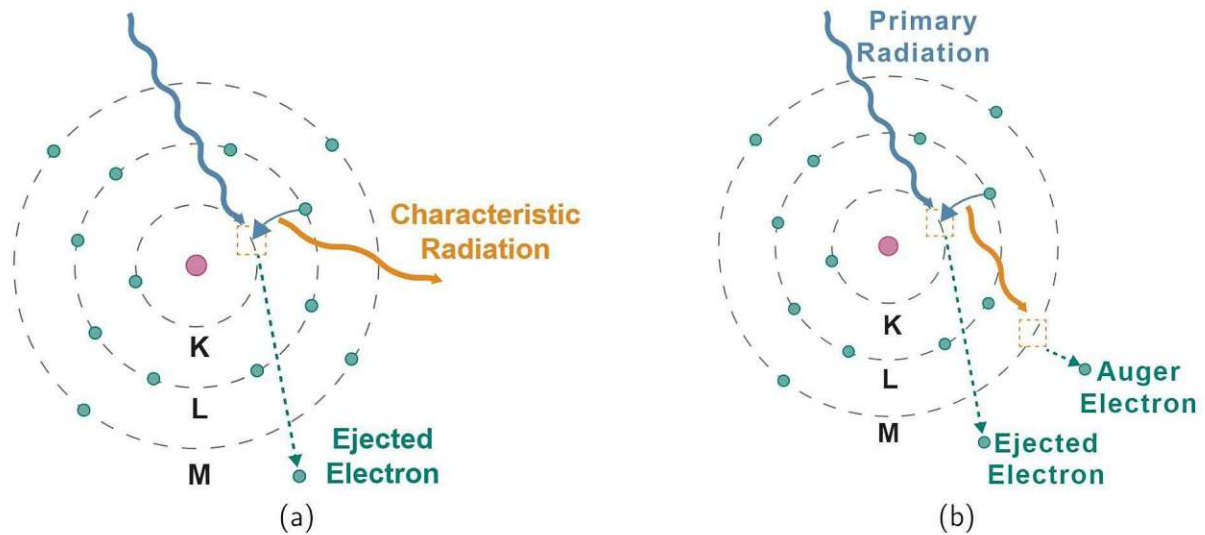


Figure 15: Relaxation of ionized atoms via (a) characteristic radiation or (b) emission of an Auger-Meitner electron.

The probability of a relaxation via emission of a fluorescence photon is given by the fluorescence yield ω_i , with i being the primary excited shell. The probability of the Auger-Meitner

process given by the Auger-Meitner yield a_i , with i being the primary excited shell and $\omega_i + a_i = 1$ decreases with the atomic number Z (see figure 16)

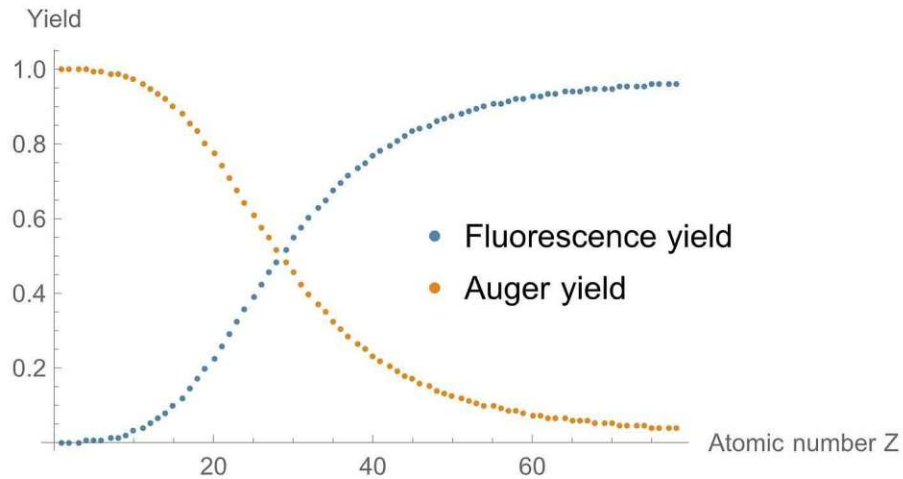


Figure 16: Fluorescence and Auger-Meitner yield for K vacancies of elements with different atomic numbers Z . Created with data from *xraylib* [19, 20].

2.3.2 Rayleigh scattering

Rayleigh scattering is the elastic or coherent scattering process of a photon at a (firmly bound inner) electron, without ionization or excitation of the atom or energy loss of the photon (see figure 17). The process of Rayleigh scattering occurs mostly at low energies and in materials with a high atomic number Z . [18, 17]

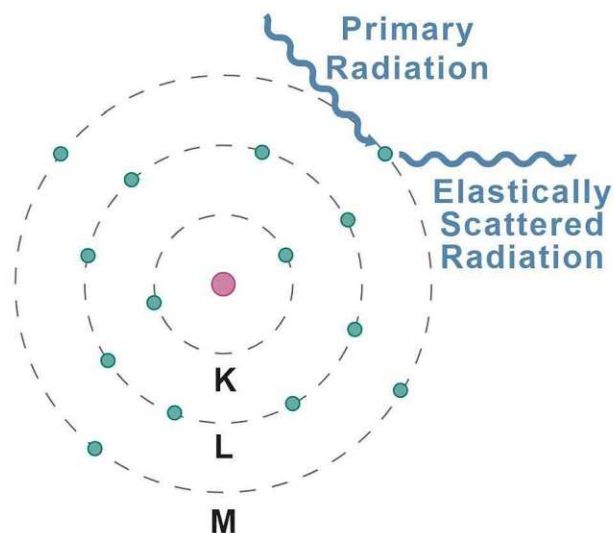


Figure 17: Schematic drawing of an elastic scattering process (Rayleigh scattering).

The differential scattering cross section, being the ratio of the number of photons scattered in a particular direction to the number of incident photons, for Rayleigh scattering of unpolarized radiation can be written as [18]

$$\frac{d\sigma_R}{d\Omega} = \frac{1}{2}r_e^2(1 + \cos^2(\theta)) \cdot |F(x, Z)|^2 \quad (12)$$

where r_e is the classical electron radius, θ the angle between the photons direction of travel before and after the scattering interaction and $F(x, Z)$ the atomic form factors. The differential Rayleigh scattering cross-sections for polarized and unpolarized radiation $\frac{d\sigma_R}{d\Omega}(Z, E, \theta)$ are available via *xraylib* [19, 20] using the atomic form factors taken from [21].

2.3.3 Compton scattering

Compton scattering is the inelastic scattering process of a photon with a (loosely bound or even free) electron with a change of direction and loss of energy of the photon. For a given scattering direction and primary energy the energy of the given photon can be calculated using the conservation of energy and momentum [18, 17].

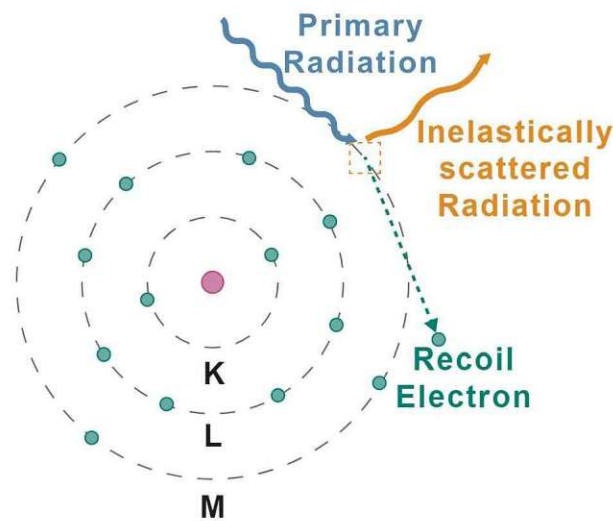


Figure 18: Schematic drawing of an inelastic scattering process (Compton scattering).

The differential scattering cross section for Compton scattering of unpolarized radiation can be written as [20]

$$\frac{d\sigma_C}{d\Omega} = \frac{d\sigma_{KN}}{d\Omega} \cdot S(x, Z) = \frac{r_e^2}{2} \cdot \left(\frac{K}{K_0}\right)^2 \cdot \left(\frac{K}{K_0} + \frac{K_0}{K} - 2\sin^2(\theta)\right) \cdot S(x, Z) \quad (13)$$

where r_e is the classical electron radius, θ the angle between the photons direction of travel before and after the scattering interaction, $S(x, Z)$ the incoherent scattering function and

$$\frac{K}{K_0} = 1 + \frac{E_i}{m_e c^2} (1 - \cos(\theta)) \quad (14)$$

where E_i is the energy of the incoming photon and m_e the electron mass. The differential Compton scattering cross-sections for polarized and unpolarized radiation $\frac{d\sigma_C}{d\Omega}(Z, E, \theta)$ are available via *xraylib* [19, 20] using the incoherent scattering functions taken from [22]).

2.4 X-ray detectors

Modern energy dispersive X-ray fluorescence setups use Silicon Drift detectors (SDD) for the collection of the fluorescence signal. SDDs absorb X-rays creating a charge carrier packages, with a charge proportional to the energy of the absorbed photon. These charge carriers are accelerated by an electrical drift field, generated by a series of electrodes with different potential (see figure 19). [23]

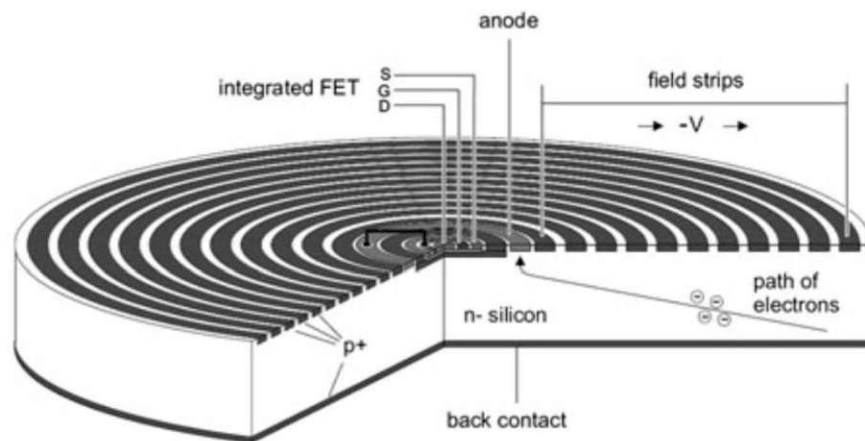


Figure 19: Sketch of a silicon drift detector (SDD) taken from [23].

Advantages of SDD detectors compared to previously commonly used Si(Li) detectors are their higher count rates due to a reduced dead time and their ability to be operated at higher temperatures (no liquid nitrogen cooling is needed). [23].

2.5 Confocal micro X-ray fluorescence analysis (CMXRF)

Typical X-Ray fluorescence setups consist of an X-ray source and a detector in a fixed geometry and a sample mounted on a movable sample holder to investigate different parts of the sample. In such a setup the investigated area of the sample, depends on the size of the beam generated by the X-ray source. The beam size can be limited to investigate smaller areas of the sample using apertures. Alternatively polycapillary optics can be used to focus the beam to microscopic size (some μm), to increase the primary beam intensity compared to a setup using apertures. Such a setup is well-suited for the two-dimensional investigation of samples. Nevertheless the sketch shown in figure 20 shows that, in such a setup it is impossible to distinguish from which depth of the sample the detected fluorescence radiation is coming.

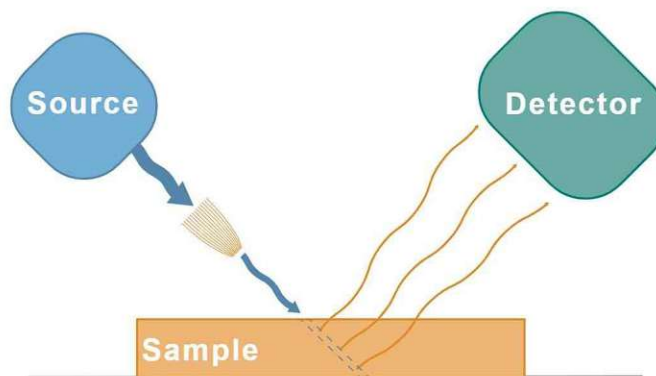


Figure 20: Sketch of a typical micro-XRF setup.

To address this problem, confocal Micro X-ray fluorescence analysis (CMXRF) setups [24, 25] use a second polycapillary optic to limit the area visible to the detector (see figure 21). To achieve a minimal investigated volume, the polycapillary optics are setup in a way that their foci coincide in the same spot (thus the term *confocal*).

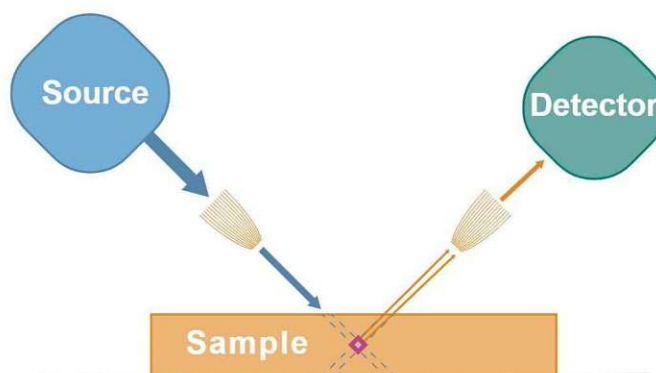


Figure 21: Sketch of a typical confocal Micro-XRF setup.

Such a setup can be used to investigate the three-dimensional elemental distribution of a sample, by moving it relative to the investigated confocal volume. The investigated volume is determined by the parameters and position of the used polycapillary optics as well as the energy of the excitation and fluorescence radiation.

2.6 Quantitative X-ray fluorescence analysis

Quantitative interpretations of XRF measurements can be achieved using well classified standard reference materials and a calibrated setup. The intensity of the measured signal can be calculated using the *fundamental parameter method* mathematically described in the equation, first described by *Sherman* in 1955 [26]. The Sherman equation can be written as [23]

$$I_i = G \int_E \frac{w_i \cdot \tau_i(E) \cdot \frac{S-1}{S} \cdot p_i \cdot \omega_i}{\frac{\mu(E)}{\sin(\theta_{incident})} + \frac{\mu_i}{\sin(\theta_{take-off})}} \cdot I_0(E) \cdot dE \quad (15)$$

where I_i is the intensity of the measured line of an element i , G is a factor considering the geometry of the setup, τ the linear absorption coefficient, $\frac{S-1}{S}$ the jump ratio, p the transition probability, ω the fluorescence yield, w the weight fraction, μ the linear mass absorption coefficient, E the energy, θ the angle of incidence or take of and $I_0(E)$ the intensity of the primary radiation.[23]

This relation can be adapted to include the energy dependent transmission of the capillary optic $T(E)$ and an elemental correction factor C_i

$$I_i = G \int_E \frac{w_i \cdot \tau_i(E) \cdot \frac{S-1}{S} \cdot p_i \cdot \omega_i}{\frac{\mu(E)}{\sin(\theta_{incident})} + \frac{\mu_i}{\sin(\theta_{take-off})}} \cdot I_0(E) \cdot T(E) \cdot C_i \cdot dE \quad (16)$$

Still this adapted version of the Sherman equation neglects effects of secondary excitation making adjustments with correction terms for second order interactions necessary. These can be written as

$$S_{ij} = \frac{G}{2} \cdot \int \frac{w_i \cdot \tau_i \cdot \frac{S_i-1}{S_i} \cdot p_i \cdot \omega_i \cdot w_j \cdot \tau_j \cdot \frac{S_j-1}{S_j} \cdot p_j \cdot \omega_j \cdot I_0(E)}{\frac{\mu(E)_S}{\sin(\theta_{incident})} + \frac{\mu(i)_S}{\sin(\theta_{take-off})}} \times \left[\frac{\sin(\theta_{incident})}{\mu(E)_S} \cdot \ln \left(1 + \frac{\mu(E)_S}{(\mu_j)_S \cdot \sin(\theta_{incident})} \right) + \frac{\sin(\theta_{take-off})}{(\mu_j)_S} \cdot \ln \left(1 + \frac{(\mu_j)_S}{(\mu_j)_S \cdot \sin(\theta_{take-off})} \right) \right] \cdot dE \quad (17)$$

While the routines for the simulation of X-ray fluorescence intensities discussed in this thesis rely on the concepts represented in the Sherman equation in a closed form, they pursue an iterative and discretized Monte-Carlo approach to consider the relevant interactions, made possible by the vast computational power of modern graphics processing units.

The advantages and disadvantages of common quantification routines based on the Sherman equation are discussed in section 3.

3 State of the art

Confocal Micro-X-ray fluorescence analysis (CMXRF) is a widely used technique for the non-destructive investigation of the three-dimensional elemental distribution of samples from various fields of study. Due to the non-destructive nature of the technique it is often the method of choice for the investigation of various samples, such as historical paintings [27, 28], cultural heritage objects [29] or biological samples [30, 31, 32].

Recent publications include investigations of the arsenic distribution in historic plaster, as well as color layers of bohemian panel paintings at the Czech Technical University in Prague [33, 34, 35]. Biological samples such as aquatic plants and a human tooth were investigated with CMXRF by *Perez et. al.* [30]. A further impressive recent showcase of CMXRF applied to biological samples is the investigation of hepatic iron deposition in drug-induced liver fibrosis in rats by *Xu et. al.* [31]. An extensive array of applications for CMXRF such as the depth elemental imaging of forensic samples (automotive paint samples) [36], the investigation of a microSD card [37], the visualization of a black cat drawing hidden inside a replicated Van Gogh painting [38], the investigation of Japanese lacquerware ‘Tamamushi-nuri’ [29] and investigation of the elemental deposition at a Solid/Liquid Interface [39] was shown by *Nakano and Tsuji et.al.*

Since the realization of the first confocal setups in the early 2000s using laboratory excitation sources [40, 28, 41] and synchrotron sources [24, 42, 25, 43], the need for quantitative interpretation of CMXRF measurements quickly arose. Currently two approaches to this problem are commonly used.

In [44, 45] *Mantouvalou et al.* present a modified fundamental parameter approach for homogeneous and stratified materials focusing on the correct calibration of CMXRF setups via the determination of the probing volume $\sigma_{x,i}(E_{exc}, E_{fluo})$ [46] and the integral sensitivity $\eta_{x,i}(E_{exc}, E_{fluo})$. These parameters can be written as [44]

$$\sigma_{x,i}(E_{exc}, E_{fluo}) = \sqrt{\sigma_{exc}^2(E_{exc}) \cdot \cos^2(\Psi) + \sigma_{fluo}^2(E_{fluo}) \cdot \sin^2(\Psi)} \quad (18)$$

$$\eta_{x,i}(E_{exc}, E_{fluo}) = \frac{T_{exc}(E_{exc})T_{fluo}(E_{fluo})\Omega\epsilon}{\sqrt{8\pi}} \frac{\sigma_{fluo}^2(E_{fluo})}{\sqrt{\sigma_{exc}^2(E_{exc}) + \sigma_{fluo}^2(E_{fluo})}} \quad (19)$$

with σ_i being the spotsize of the X-ray lens in excitation and detection channel, T_i the respective values for the energy dependent transmission function of the X-ray lenses, ϵ the detector efficiency, Ω the solid angle of detection and Ψ the angle between excitation channel and sample normal in a 90° geometry [44]. The modified fundamental parameter equation for the detected fluorescence signal Φ_i of a specific fluorescence peak i of a homogeneous layer as a function of depth position x can then be written as [44]

$$\begin{aligned} \Phi_i(x) = & \Phi_0 \eta_i \sigma_{F,i} \rho_i \times e^{\left(\frac{(\mu_{lin,i}^* \sigma_{x,i})^2}{2}\right)} \times e^{-\mu_{lin,i}^* x} \\ & \times \frac{1}{2} \left[\operatorname{erf} \left(\frac{d_2 + \mu_{lin,i} \sigma_{x,i}^2 - x}{\sqrt{2} \sigma_{x,i}} \right) - \operatorname{erf} \left(\frac{d_1 + \mu_{lin,i} \sigma_{x,i}^2 - x}{\sqrt{2} \sigma_{x,i}} \right) \right] \end{aligned} \quad (20)$$

with Φ_0 being the excitation intensity of the monochromatic radiation, $\sigma_{F,i}$ the fluorescence production cross section of the fluorescence peak i , ρ_i the local elemental density of the fluorescence element, $\mu_{lin,i}^*$ the effective linear mass absorption coefficient of the peak i , d_1 and d_2 the layer boundaries and the two calibration parameters $\sigma_{x,i}$ the size of the probing volume in the direction of the sample normal and the integral sensitivity η_i [44]. As both calibration parameters are functions of the excitation energy E_{exc} and the fluorescence energy E_{flu} the approach assumes monochromatic excitation, as a polychromatic excitation spectrum would require a long calibration procedure for different energies. In [47] Förste *et. al.* expand on this approach with a more generalized calibration procedure to consider polychromatic excitation spectra.

Czyzycki *et al.* [48, 49, 50] and Golioso *et al.* [51, 52] apply a Monte-Carlo ray-tracing method to simulate CMXRF and XRF spectra. The concepts of such a Monte Carlo simulation of X-rays in a massive sample and useful variance reduction techniques were discussed in [53, 54, 55, 56, 57, 58]. The possible interactions of X-rays with matter (photoionization, elastic and inelastic scattering) are modeled inside a sample of given composition. Typical variance reduction techniques include recording the probability of a photon reaching the detector after each interaction to reduce simulation times for the calculations performed on CPUs.

This thesis aims to implement the previously mentioned approach of a full forward Monte Carlo ray-tracing of the rays inside the sample "without the constraint of forcing the photons to the detector" [44], i.e. a full "brute force" [53] model of the ray path, to consider all higher order effects inside the sample combined with the possibility to model voxel-based samples

more complex than layer structures or homogeneous materials, similar to the mosaic model discussed in [10]. This time-demanding simulation task is made feasible by the use of the vast parallelization capabilities of modern graphics processing units. This approach while computationally expensive tackles multiple challenges present in the above discussed models.

- **Energy dependency of the confocal volume:** The energy dependent confocal volume does not have to be determined via calibration. As the shape and size of the volume is also highly sensitive to the correct alignment of the capillary optics (see section 4.3) this calibration process is usually necessary for each adjustment of the setup using fundamental parameter approaches.
- **Peak deconvolution:** The simulation process does not depend on the peak deconvolution of the measured spectra with AXIL [59] or PyMca [60]. This process can often be difficult or even faulty, due to overlapping lines and varying results of fit routines when deviating from fixed line ratios, e.g. between $K\alpha$ and $K\beta$, which cannot be applied due to possibly different absorption inside the sample.
- **Consideration of scattering and higher order effects:** All higher order processes, from multiple scattering to secondary excitation, as discussed in [10] are automatically considered in this approach.
- **Modelling of a complex voxel based sample with an energy independent voxel size:** A complex 3D sample can be simulated with voxels containing multiple elements. The voxel size of the model can be chosen independent of the confocal volume. This allows the modelling of a voxel size smaller than the confocal volume improving the possible scan resolution.
- **Change of setup to non-confocal:** The developed software can be used for the modelling of X-ray paths in confocal and non confocal setups.

4 voxTrace

Parts of the following section were previously published in [61]. voxTrace is a voxel-based Monte-Carlo ray-tracing code for the simulation of X-ray fluorescence spectra. It utilizes the computational power of graphics processing units (General Purpose Computation on Graphics Processing Units *GPGPU*) for the highly parallel task of tracing the path of single X-rays through a massive sample. The freely available and commonly used software packages *shadow3* [62] for the simulation of X-ray sources, mirrors and other standard optical components available at the synchrotron and *polycap* [1] for the simulation of the path of X-rays in polycapillary optics can be easily used with C++ interfaces written for this purpose. The heartpiece of voxTrace simulates the interaction of the X-rays with matter in a voxel-based sample. Due to the modularity of the design, the software can be easily adapted to also simulate non-confocal Micro-XRF measurements. Figure 22 schematically depicts the simulation performed by voxTrace and the different software packages.

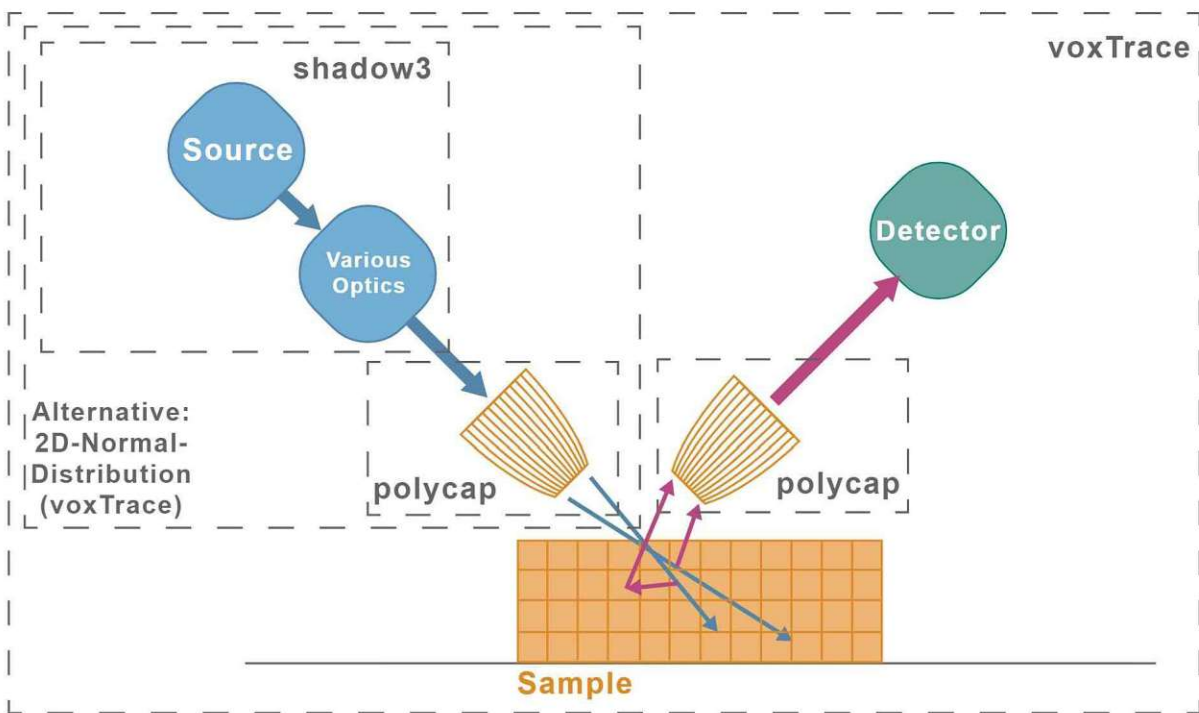


Figure 22: Schematic drawing of a modelled experimental setup, showing the different software packages (*shadow3* [62], *polycap* [1] and *voxtrace* [61]) used for modelling the different components of the setup. Primary X-rays (blue) interact with material in the sample (absorption and scattering), producing secondary X-rays (red), which can again interact with the sample. Previously published in [61].

4.1 Algorithm

Monte-Carlo X-ray tracing through samples has been expertly described by Vincze et. al. and Schoonjans et.al in a series of papers [53, 54, 55, 56, 57, 58]. A short overview over the involved calculations is given in the following.

Initial starting point of voxTrace's simulation process is a ray exiting the primary polycapillary optic. This ray can either be taken from a list of previously generated rays. This can be used to model complex optical systems at synchrotron sources. The software package *shadow3* [62] allows the simulation of synchrotron sources and selected other parts of optical systems (mirrors, crystals, etc.). For an exact modelling of the path of these rays in polycapillary optics the software *polycap* [1] can be used to model the primary polycapillary optic. To easily use both software packages in combination with voxTrace a C++ interface to implementing clean namespaces for all packages was written.

Alternatively voxTrace features the possibility to generate primary X-rays as a two-dimensional normal distribution. This feature was implemented, as the reading of large files was shown to slow down the simulation process drastically. The validity of both approaches was shown in [63], with the investigation of different polycapillary half-lenses and comparison of measured results with analytical models and results simulated with *polycap* (see also section 5.2).

The primary ray is intersected with the sample and the initially interacting Voxel is established. The intersection length of voxel and the ray is then calculated as the distance between entry and exit point established via intersection with the bordering planes of the voxel. A sketch of this process in two dimensions is shown in figure 23.

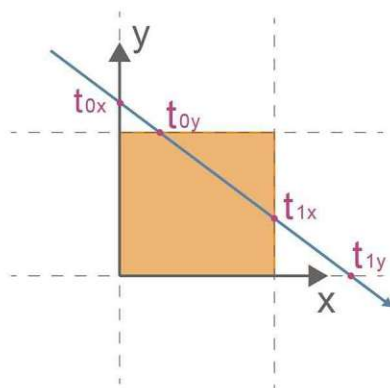


Figure 23: Two-dimensional representation of a ray intersecting a voxel.

Now the probability for an interaction of the ray in this voxel can be calculated using Beer's law (see equation 9). Generating a random Number R between 0 and 1 the probability for an interaction can be established by

$$e^{-\mu \cdot \Delta x} < R = \begin{cases} \text{if true} \rightarrow \text{interaction} \\ \text{if false} \rightarrow \text{go to next voxel} \end{cases} \quad (21)$$

Each voxel holds information about its elemental composition, in the form of an array with the weight percentage of each chemical element in the voxel. Which element interacts with the voxel can be established by comparison of a new random number R between 0 and 1 with the weighted percentage of the attenuation coefficient of the specific element with the overall attenuation coefficient of the material. This can be written as

$$\sum_i^k \mu_{i-lin-\%} \leq R \leq \sum_i^{k+1} \mu_{i-lin-\%} \quad (22)$$

where $\mu_{i-lin-\%} = \frac{w_i \cdot \mu_{Lin-i}}{\mu_{Lin-Total}}$, μ_{Lin-i} is the linear absorption coefficient of the element i with the weight fraction w_i , $\mu_{Lin-Total}$ being the total linear absorption coefficient and k being a number smaller than the number of elements in the material of the voxel.

Which interaction takes place is established using the cross-sections for photo-absorption $\tau(E)$, Rayleigh scattering $\sigma_R(E)$ or Compton scattering $\sigma_C(E)$, the total attenuation cross-section $\mu(E) = \tau(E) + \sigma_R(E) + \sigma_C(E)$ (see section 2.3) and again a new random number R between 0 and 1.

$$0 \leq R \leq \frac{\tau(E)}{\mu(E)} \rightarrow \text{Photo absorption} \quad (23)$$

$$\frac{\tau(E)}{\mu(E)} \leq R \leq \frac{\tau(E) + \sigma_R(E)}{\mu(E)} \rightarrow \text{Rayleigh scattering} \quad (24)$$

$$\frac{\tau(E) + \sigma_R(E)}{\mu(E)} \leq R \leq \frac{\tau(E) + \sigma_R(E) + \sigma_C(E)}{\mu(E)} = 1 \rightarrow \text{Compton scattering} \quad (25)$$

For the case of photo-absorption, the excited shell can be found with the photo-absorption cross-section $\tau_i(E)$ of a single shell i of the element and the total photo-absorption cross section of the element $\sum_j \tau_j(E)$. This can be written as

$$\sum_i^k \frac{\tau_i(E)}{\sum_j \tau_j(E)} \leq R \leq \sum_i^{k+1} \frac{\tau_i(E)}{\sum_j \tau_j(E)} \quad (26)$$

Atoms excited in a photo-ionization process can relax via the emission of a Fluorescence photon or an Auger-Meitner electron (see section 2.3). Which reaction is performed can be established with the comparison of the fluorescence yield ω_i of the excited shell i with a new random number R between 0 and 1. This can be written as

$$\omega_i > R = \begin{cases} \text{if true} \rightarrow \text{Fluorescence photon} \\ \text{if false} \rightarrow \text{Auger-Meitner electron} \end{cases} \quad (27)$$

Auger-Meitner electrons are not traced further, as this would require a more complicated model of the sample. In this case a new ray from the source is generated and traced. X-ray fluorescence photons can spring from a number of transitions. Which one, is established with the use of the radiative rates r_i of a transition i , and a new random number R between 0 and 1.

$$\sum_i^k r_i \leq R \leq \sum_i^{k+1} r_i \quad (28)$$

Secondary rays have a different direction than primary rays. The according coordinate transformation using the rotational angles θ and ϕ is shown in figure 24.

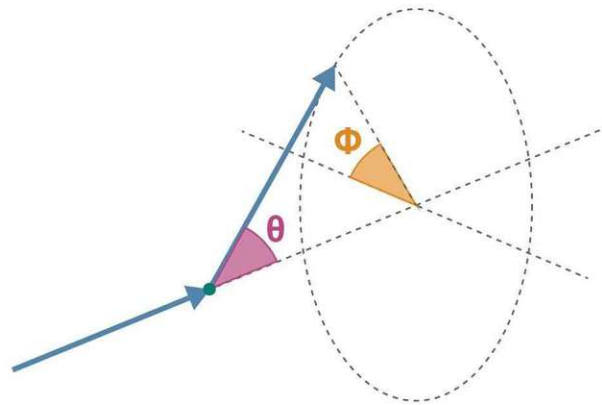


Figure 24: Coordinate transformation of a ray during an interaction process (scattering or fluorescence). The angles ϕ and θ are established using the differential scattering cross-sections for Rayleigh scattering and Compton scattering and random numbers. Previously published in [61]

For all processes (fluorescence and scattering) ϕ can be written as

$$\phi = 2\pi R \quad (29)$$

with R again being new random numbers between 0 and 1. For fluorescence photons θ can be written as

$$\theta = a \cos(2R - 1) \quad (30)$$

with R again being new random numbers between 0 and 1. For scattering processes θ can be established with the differential scattering cross-sections for Rayleigh scattering or Compton scattering.

$$\frac{2\pi}{\sigma(E, Z)} \sum_0^i \frac{d\sigma}{d\Omega}(E, Z, \theta) \cdot \Delta\theta \leq R \leq \frac{2\pi}{\sigma(E, Z)} \sum_0^{i+1} \frac{d\sigma}{d\Omega}(E, Z, \theta) \cdot \Delta\theta \quad (31)$$

with $\frac{d\sigma}{d\Omega}(E, Z, \theta)$ being the differential scattering cross-section ($\frac{d\sigma_R}{d\Omega}$ for elastic scattering and $\frac{d\sigma_C}{d\Omega}$ for inelastic scattering) and R again being a new random number between 0 and 1. If an interaction has taken place, the resulting ray is traced further in the same manner as described above with the current voxel serving as the first voxel potentially interacting with the new ray. This recursion is an important feature of the software, as higher order effects such as secondary excitation or absorption and further fluorescence of a scattered primary photon is considered. Future development of the software will include the possibility to set flags for different interactions, making a more exact peak deconvolution of the resulting spectrum possible, to further investigate the proportions of primary excitation, secondary excitation and scattered radiation reaching the detector. Figure 25 shows a flowchart of the simulation process.

Another important aspect to be noted is the result of the simulation being a complete spectrum, comparable to a measured XRF spectrum. This direct comparison makes it possible to skip the usual step of peak deconvolution of measured spectra, which itself can be a difficult process.

Further future developments will include the implementation of global optimization algorithms taking the weight-percentage of each element in each voxel as a free parameter to fit the simulated spectra to measured ones. This should make a fine-tuned quantification of unknown samples without similar standard reference materials possible.

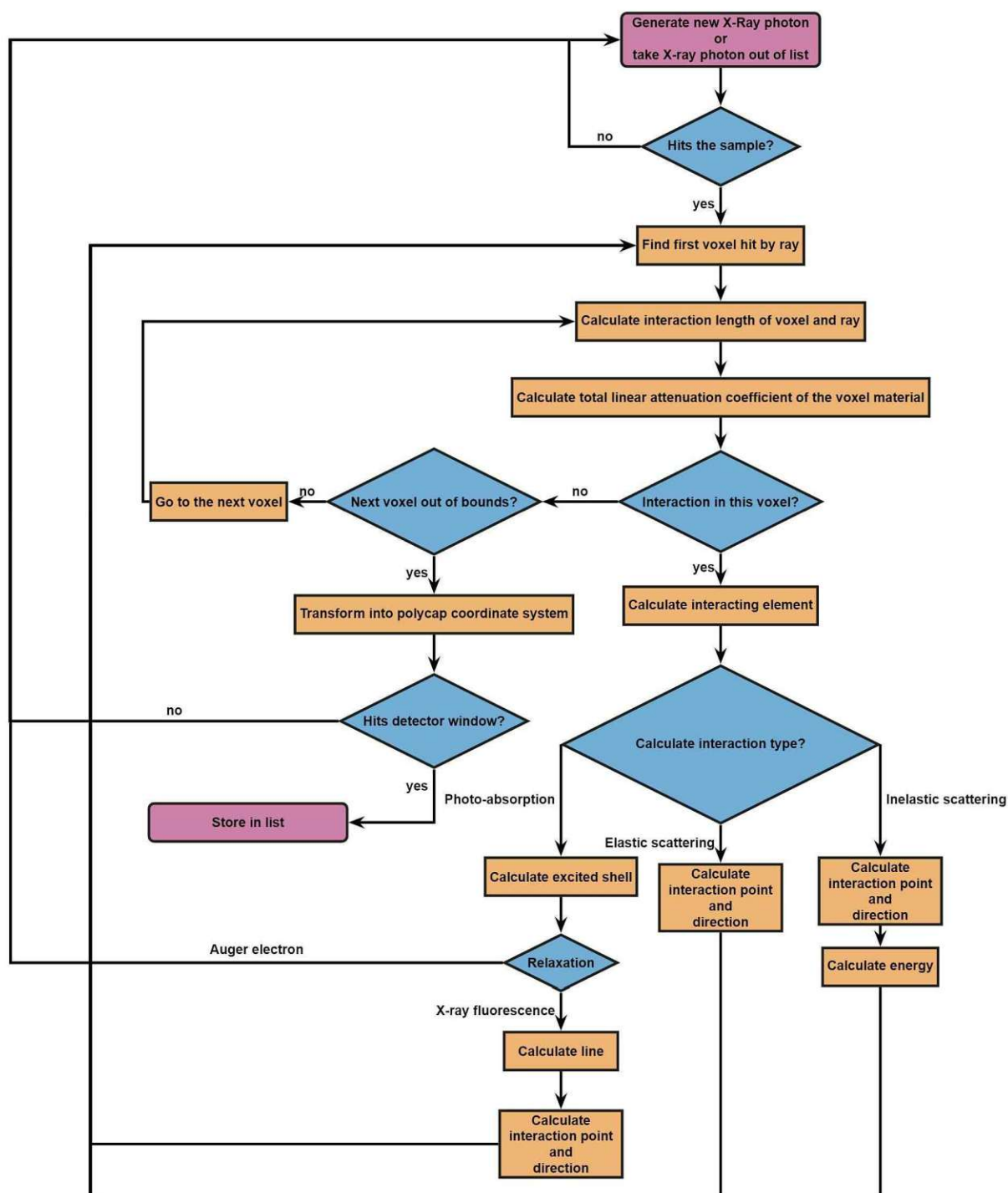


Figure 25: Workflow of the simulation software voxTrace. X-rays are traced through a sample of given elemental distribution. New primary X-rays are generated or taken from a list of rays until enough scattered and fluorescence photons reach the entrance window of the secondary polycapillary optic. Previously published in [61]

4.2 Implementation

First implementation attempts in C++ with OpenMP acceleration proved insufficient, concerning speed. Single points of simulation exceeded a feasible timeframe for the simulation of a statistically relevant signal. Therefore the software was reimplemented in *CUDA C++*, utilizing the power of graphics processing units (GPU) using *armadillo* [64] library for linear algebra to handle data sets larger than 3D vectors.

CUDA is a toolkit provided by NVIDIA for the acceleration of parallel tasks on NVIDIA GPUs, commonly used in home computers and high performance clusters. It offers a C++/C like interface. While Object oriented *CUDA* is not a common choice in the world of high performance computing (HPCs) an object-oriented approach was chosen for this project to clearly separate calculations belonging to different physical entities and obtain a flexible, expandable, comprehensible and easily maintainable code. The implemented objects are: *ChemElementGPU*, *MaterialGPU*, *VoxelGPU*, *SampleGPU*, *RayGPU* and *TracerGPU*. Figure 26 shows a simplified class diagramm of the implemented objects.

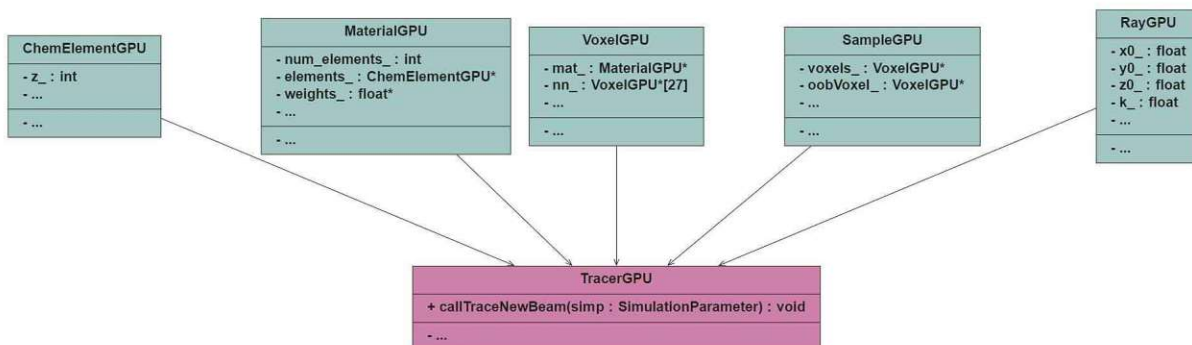


Figure 26: Class Diagramm. Previously published in [61]

ChemElementGPU discretizes all necessary fundamental parameters (attenuation coefficients, cross-sections, fluorescence yields, etc.) from *xraylib* [19, 20]. As this information can quickly become expensive in terms of memory, when used redundantly for each voxel, only one *ChemElementGPU* is created for each chemical element present in the sample.

MaterialGPU is the "lowest" entity of the sample model. It holds an array with the weight concentrations of the different chemical elements in the material as well as pointers to the specific *ChemElementGPUs*.

VoxelGPU contains the geometric information (position and size) about the voxels in the sample. Each *VoxelGPU* holds a pointer to a single *MaterialGPU*. This clear separation of geometry and elemental composition was chosen on purpose for easier adaption of the voxel geometry in future development, for possible advantage of speed.

SampleGPU combines the information of the other objects holding data of the overall sample dimensions as well as pointers to the list of all *VoxelGPUs* in the sample as well as a single "out-of-bounds"-*VoxelGPU* representing the outside of the sample.

RayGPU holds information about the specific X-rays traced through the sample. The information consists of the coordinates of the origin and the direction of the ray, as well as its energy. Parameters for polarisation, as present in other software packages like *shadow3* [62] and flags for different types of interaction (see above) can be easily added.

TracerGPU is so to say the *main* function of the code instantiating the previously mentioned objects. It should be noted here that while the software has only been tested for the simulation of monochromatic excitation radiation, the generation of rays with a polychromatic excitation spectrum is also possible.

The software design considers memory efficiency, speed and ease of adaptability for different simulation setups. The choice of the implementation using *CUDA* limits the scope of applicability of the software to computers with *NVIDIA* hardware. Nevertheless the vast speed-up of using GPUs for ray-tracing, a task for which they are build for, justifies the choice. Furthermore *CUDA*'s C/C++-like interface makes the code easily readable and adaptable to developers proficient in those languages. Benchmarks for the simulation of a depth scan of a homogeneous NIST certified standard reference material were performed (see results in section 4.3).

A statistically relevant signal of the main elements Cu and Zn could be simulated on a reasonably priced (~ 2500 € in 2019) regular workstation PC with an AMD Ryzen 7 5800X, 8C/16T, 3.80-4.70 GHz CPU and a ZOTAC Gaming GeForce RTX 3060 Ti Twin Edge OC LHR, 8GB GPU in approximately 5 h for 20 measurement points.

The same results could be achieved in approximately 5 minutes on a single node of the

Vienna Scientific Cluster with 2 NVIDIA A40 GPUs and a dual socket with 8 cores AMD EPYC 7252.

4.3 How to use voxTrace

voxTrace 1.0 as published in [61] loads the necessary simulation parameters from 4 txt-files (*Sample.txt*, *Capillaries.txt*, *Materials.txt*, *Simulation.txt*). The basic geometry of the sample model (see table 1, defining a sample with $60 \times 60 \times 60$ quadratic voxels with a side length of $5\mu m$) is defined in *Sample.txt*

Coordinate origin		Sample dimensions		Voxel dimensions	
Parameter	Example Value	Parameter	Example Value	Parameter	Example Value
X	$0.0 \mu m$	X	$300.0 \mu m$	X	$5.0 \mu m$
Y	$0.0 \mu m$	Y	$300.0 \mu m$	Y	$5.0 \mu m$
Z	$0.0 \mu m$	Z	$300.0 \mu m$	Z	$5.0 \mu m$

Table 1: Basic geometry of the sample defined in *Sample.txt*

The positions and geometry of the polycapillary optics in the setup, as well as the monochromatic energy (see table 2 and figure 27) is read from *Capillaries.txt*.

Primary polycapillary		Secondary polycapillary	
Parameter	Example Value	Parameter	Example Value
X (focal point)	$150.0 \mu m$	X (focal point)	$150.0 \mu m$
Y (focal point)	$150.0 \mu m$	Y (focal point)	$157.0 \mu m$
Z (focal point)	$0.0 \mu m$	Z (focal point)	$7.0 \mu m$
Working distance	$5100.0 \mu m$	Working distance	$4900.0 \mu m$
α	45.0°	β	45.1°
Exit radius	$1075.0 \mu m$	Entrance-Radius	$950.0 \mu m$
Focal spot size	$16.5 \mu m$		
Primary beam energy	$17.4 keV$		

Table 2: Positioning and geometry of the capillary optics.

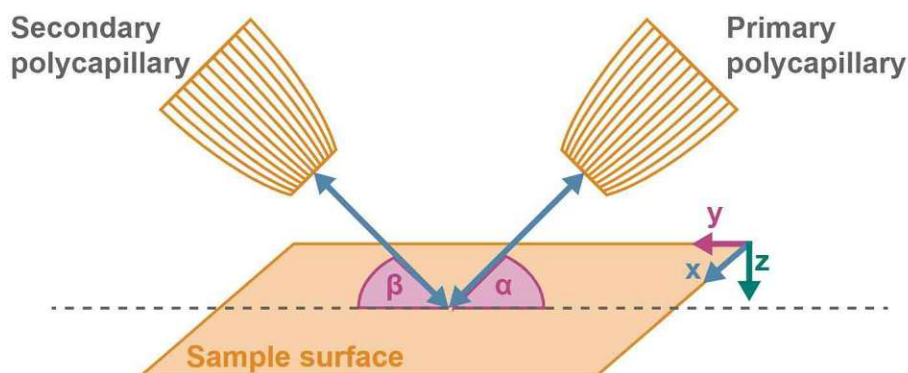


Figure 27: Positioning and geometry of the polycapillary optics in the setup.

The elemental composition of the sample is read from *Materials.txt*. Here a small python routine can help to generate a simple homogeneous or layered sample model. For more complex samples a similarly simple routine to use measured line intensity ratios as a starting elemental composition for optimization routines can be realised this way. Table 3 shows an example for the definition of a homogeneous NIST certified standard reference material 1107 brass sample, defining for each voxel with the integer coordinates x,y,z (in our case of a sample with 60 voxels with all possible combinations between 0 and 59) the number of elements in the voxel, the atomic number of the elements and their weight-percentage in the material of the voxel.

```
# Point 1
0, 0, 0 # x,y,z
6 # Number of Elements
26, 28, 29, 30, 50, 82 # Elements Z
0.0004, 0.001, 0.6119, 0.3741, 0.0107, 0.0019 # Element Mass Fractions

# Point 2
0, 0, 1 # x,y,z
6 # Number of Elements
26, 28, 29, 30, 50, 82 # Elements Z
0.0004, 0.001, 0.6119, 0.3741, 0.0107, 0.0019 # Element Mass Fractions

# Point 3
0, 0, 2 # x,y,z
...
```

Table 3: Material composition of the sample model.

Finally the scan path and the number of rays to hit the secondary polycapillary entrance window to be simulated are read from *Simulation.txt*. Detector effects are currently not modeled in the code.

Number of Rays		30000		
Measurement points	x	y	z	
1	0.0	0.0	-50.0	
2	0.0	0.0	-40.0	
3	0.0	0.0	-30.0	
4	0.0	0.0	-20.0	
5	0.0	0.0	-10.0	
6	0.0	0.0	0.0	
7	0.0	0.0	10.0	
8	0.0	0.0	20.0	
9	0.0	0.0	30.0	
10	0.0	0.0	40.0	
11	0.0	0.0	50.0	

Table 4: Scan path and number of rays to be traced

Simulations with the parameters as defined above (see table 1-4) were performed on a regular PC and a high-performance cluster (see Benchmark times in section 4.2). The list of rays reaching the detector can be depicted as an energy dispersive spectrum and compared to measurement results (see figure 28).

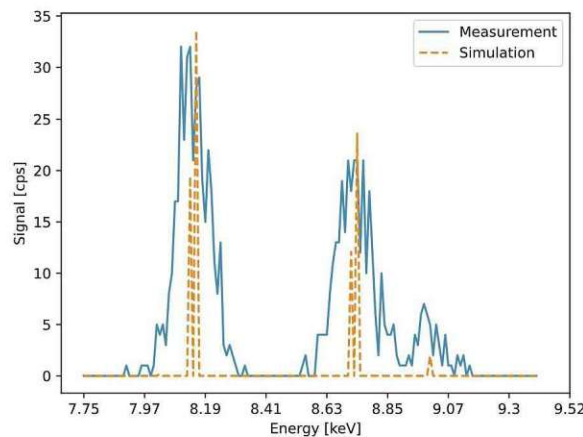
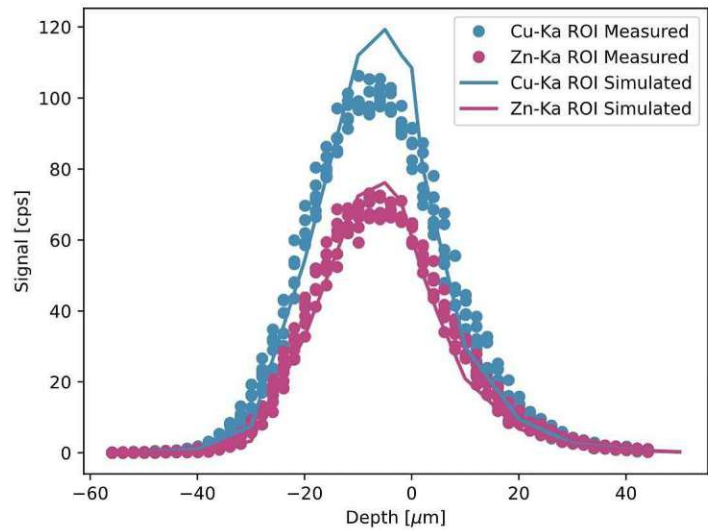
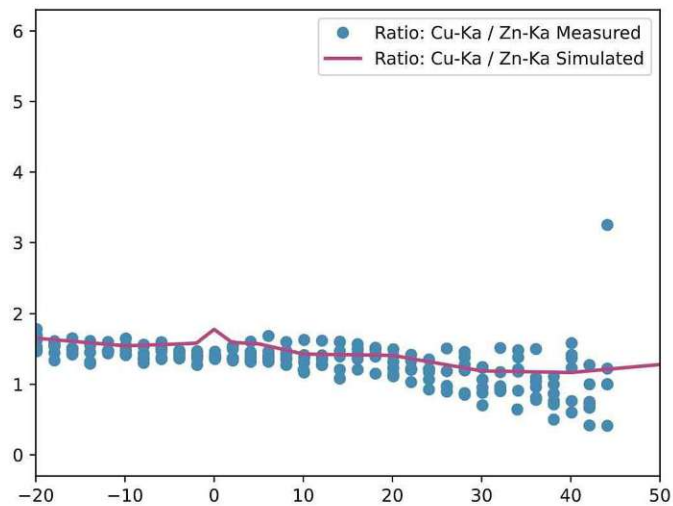


Figure 28: Measured spectrum for the measurement point in depth 20 μm below sample surface compared to the scaled simulated spectrum in the same measurement point. Previously published in [61]

The results for the intensities of the main lines $\text{Cu-K}\alpha$ and $\text{Zn-K}\alpha$ for different depth, as well as the ratio between the intensities in those depths are shown in figure 29.



(a)



(b)

Figure 29: Comparison of empirical results with simulated data for the certified standard reference material sample NIST 1107. (a): Plot of the $\text{K}\alpha$ -lines of the main elements Cu and Zn as a function of depth. (b): Signal ratio of the $\text{K}\alpha$ -lines of the main elements Cu and Zn as a function of depth. Previously published in [61]

It should be mentioned that a small misalignment of the setup can have an effect on the shape and orientation of the confocal volume. This further has an effect on the shape of the depth curve shown in figure 29. Note that the angle between capillaries is slightly tilted, 0.1° with respect to a 90° angle (see table 2 with $\beta = 45.1^\circ$) and a small misplacement of the focal point of the secondary polycapillary optic, $10 \mu\text{m}$ along its own optical axis from the focal point of the primary polycapillary optic (see table 2 with $Y = 157.0$ and $Z = 7.0$) is modelled in the simulation. Such a misalignment can be considered small and hard to eliminate during an adjustment procedure. The shape of the curve without such a misalignment ($\beta = 45.0^\circ$, $Y = 150.0$ and $Z = 0.0$) is shown in figure 30.

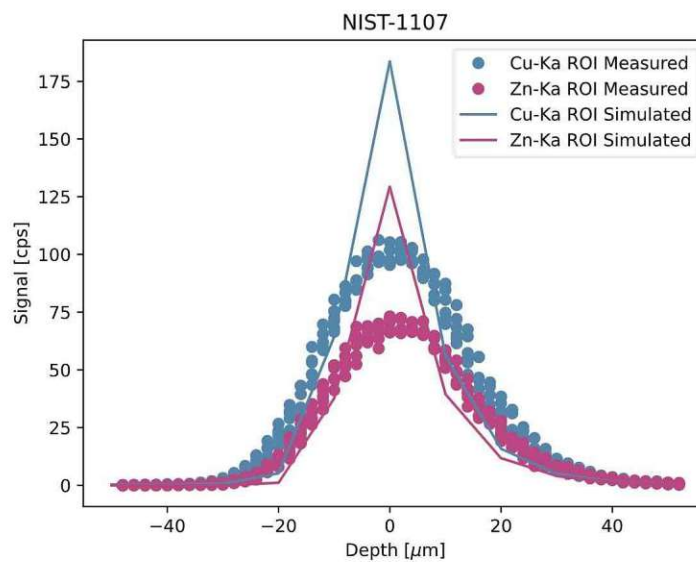


Figure 30: Comparison of empirical results with simulated data for the certified standard reference material sample NIST 1107, with an ideally aligned setup. Plot of the $K\alpha$ -lines of the main elements Cu and Zn as a function of depth.

This shows that a small misalignment of the setup is likely as simulated curves in figure 29 show a better fit to measurement results than figure 30. This is an illustrative example of voxTrace's capabilities for the investigation and modelling of not only samples but also CMXRF setups.

5 Experimental work

Experimental work was done with a CMXRF setup for the lab and synchrotrons using monochromatic excitation radiation. The resolution and imaging qualities of the setup were tested in a number of experiments in the X-ray laboratory at the Atominstitut of the TU Wien. Furthermore the properties of polycapillary half-lenses were investigated in experiments at Atominstitut and at the BAMline beamline at the BESSY II Synchrotron of the Helmholtz-Zentrum-Berlin. Additionally standard reference materials with a three-dimensional structure, developed by partners from the Institute of Inorganic and Analytical Chemistry at Clausthal University of Technology, were investigated at Atominstitut as well as at the XRF beamline at the Elettra Sincrotrone Trieste and B16 Test Beamline at the Diamond Light Source. Measurement results were compared with simulations performed with *voxTrace*, as a validation of the simulation procedure. Parts of the following sections were previously published in [65, 63, 61].

5.1 A monochromatic confocal micro-x-ray fluorescence spectrometer

Parts of the following section were previously published in [65]. Typical CMXRF lab setups use polychromatic excitation for imaging purposes (see section 2.5), to exploit the full intensity of the X-ray beam generated by the X-ray tube. Nevertheless quantitative interpretation of such setups is difficult due to the need for the exact knowledge of the transmission properties of the used capillary lenses as well as high scattering background. Thus a monochromatic CMXRF setup was realized to address these challenges.

The setup (see figure 31) consists of a standard water-cooled x-ray diffraction (XRD) glass tube, mounted in line focus direction. The tube with the anode material molybdenum, can be operated at 2kW and produces a beam with the dimensions $0.04 \times 8\text{mm}^2$.

An AXO Dresden one dimensional parabolic multilayer monochromator, for Mo- $K\alpha$ with a length of 10 *cm* is used to monochromatize the beam. The output is a nearly parallel beam (divergence 0.027°) with a size of $1 \times 8\text{mm}^2$. Monochromator and X-ray tube are mounted on a plate, that can be moved in vertical direction with a motorized stage. Furthermore the monochromator is mounted on a motorized stage. In this way the position of monochromator in respect to the tube exit window, as well as the overall position of this "X-ray source" for

a monochromatic parallel beam in respect to the rest of the setup can be adjusted.

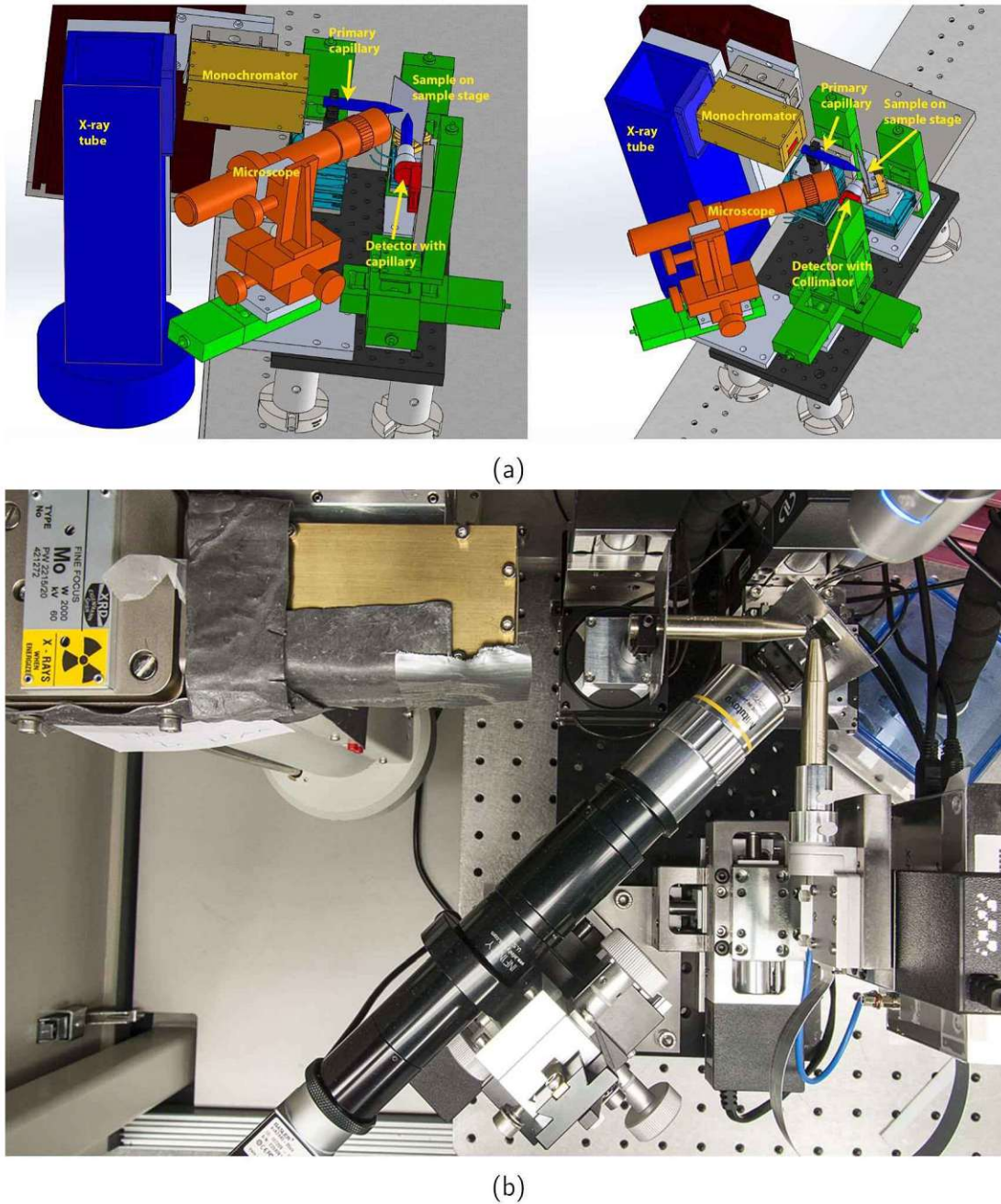


Figure 31: Monochromatic confocal Micro X-ray fluorescence setup consisting of an X-ray tube, a parallel beam monochromator a primary polycapillary half-lens to focus the beam, a moveable sample stage and microscope to position the sample stage and a detector (a) Sketch of the setup at the Atominstitut consisting of an (b) Photo of ATI-Setup from top [65].

The parallel monochromatic beam is focused by a polycapillary half-lens (see section 2.2) produced by Fischer (former IFG - Institute for Scientific Instruments GmbH). The polycapillary is encapsulated in a helium-filled housing with thin beryllium entrance and exit windows, mounted on a motorized sample stage for the movement in 5 directions. Four piezo-based attocube nanopositioners enable the positioning in the directions x , y , yaw and pitch. A Newport MFA-CC motorized linear stage is used to control the movement of the capillary in z -direction. For 17.4 keV ($\text{Mo-K}\alpha$) a focus size of $16.5 \mu\text{m}$ is achieved (see PC-246 in section 5.2). To reduce scattering radiation a Pb shield is mounted around the polycapillary encapsulation.

Samples can be mounted on a motorized sample stage with three degrees of freedom. X - and y - movement are controlled by two ECS nanopositioners from attocube, with a bidirectional repeatability of 50 nm . Z -movement is controlled by a Newport MFA-CC linear stage, with a bidirectional repeatability of less than $1 \mu\text{m}$.

A microscope setup consisting of a Mitutoyo Plan Apo infinity corrected long working distance objective with $10\times$ magnification, an Infinity InfiniTube standard, and a Basler Ace acA2440-35uc USB3 camera is used for positioning and optically investigating the surface of samples. The small depth of focus ($3.5 \mu\text{m}$) is helpful for a fast sample positioning. The positioning of the microscope can be adjusted with a manual XYZ stage.

An Amptek Silicon Drift Detector (SDD) with an active area of 50 mm^2 , a thickness of $500 \mu\text{m}$ and a $12.5 \mu\text{m}$ beryllium window is used. Its position can be adjusted by three MFA-CC linear stages from Newport.

The secondary polycapillary optic is again from Fischer with dimensions and properties very similar to the primary polycapillary optic (see PC-236 in section 5.2). For two-dimensional investigations the secondary polycapillary can be replaced by a collimator to enlarge the photon flux (see figure 31 (a), right).

The modularity of the setup, enables flexible usability for various problems. The complete setup except X-ray tube and monochromator is mounted on a single optical plate, making it easy to dismount, transport to a synchrotron source and set up there. For investigations in the lab, X-ray tube and monochromator optic can be easily replaced for tubes with a

different anode material, i.e. excitation energy, and the according monochromator optic. The possibility to replace the secondary polycapillary optic with a collimator to enhance the photon flux for two-dimensional investigations, is especially important for lab measurements as measurement times for confocal measurements can be very long, due to the lower brilliance of X-ray tubes compared to synchrotron sources.

The proper adjustment of the capillary optics can be achieved and tested with scans of a cross structure, made out of two Cu-wires with a diameter of approximately $10\mu\text{m}$ mounted on a Gd-Screen. Figure 32 shows the 3D representation of the Cu (red) and Gd (grey) using the intensities of the Cu- $K\alpha$ and Gd- $L\alpha$ lines. The measurements were performed with a step size of $3\mu\text{m}$ (in the x, y, and z direction) and a counting time of 10 s/point. For Cu- $K\alpha$, the confocal volume is $15 \times 20 \times 20\mu\text{m}^3$.

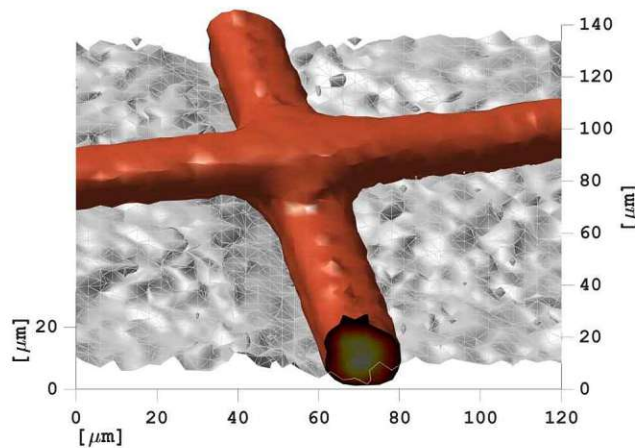
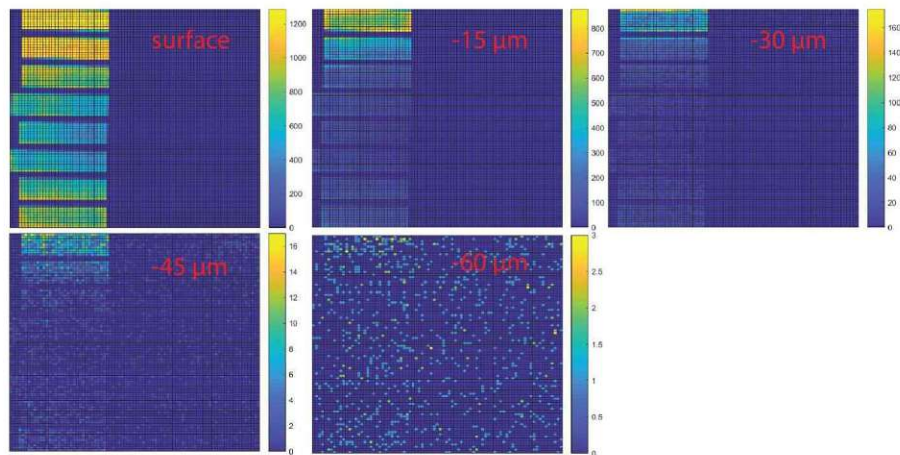


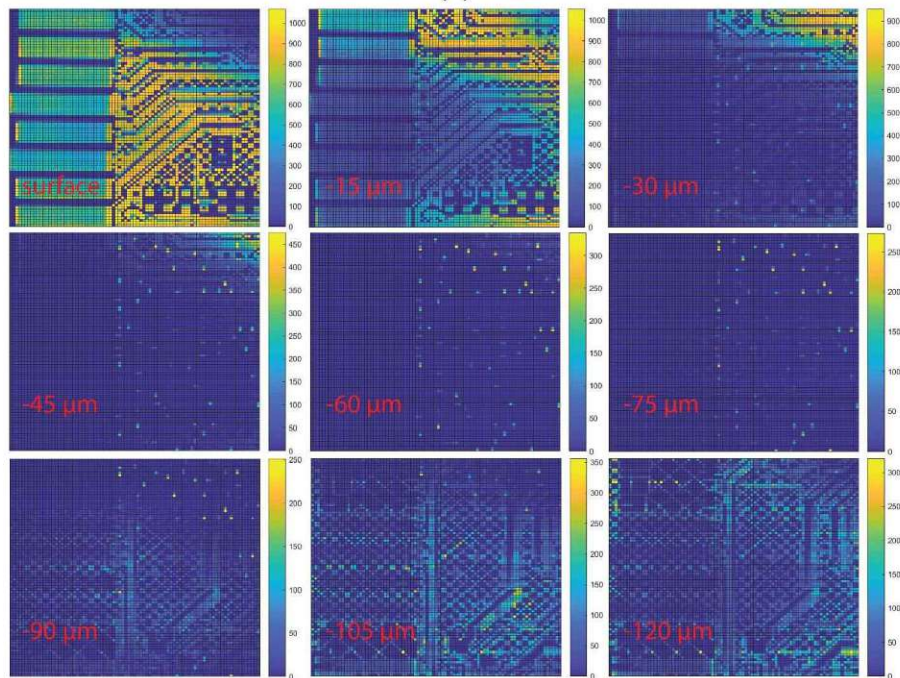
Figure 32: 3D scan of a $10\mu\text{m}$ thick copper wire on a Gd screen. The red color shows the surface with the Cu- $K\alpha$ intensity, whereas gray represents Gd- $L\alpha$ from the screen. The measurements were performed with a step size of $3\mu\text{m}$ (in the x, y, and z direction) and a counting time of 10 s/point, with the tube being operated at 50 kV and 38 mA [65].

As discussed in section 2.5, confocal setups are widely used for imaging purposes. These capabilities can be demonstrated for the given setup with a scan of an area as large as $8.5 \times 8.2\text{mm}^2$ of an SD-card. The scan covers the sample from a distance of $15\mu\text{m}$ to the surface down to a depth of $120\mu\text{m}$ in 9 steps with a stepsize of $15\mu\text{m}$ and a step size in the surface plane of $100\mu\text{m}$. This amounts to a total of 64 242 measurement points. With a measuring time per point of 15 s (in the lab setup), the total scan time resulted to be more

than 11 days. The Ni and Cu distribution maps for different depths are shown in figure 33. The results of this scan are in good agreement with results for an SD-card scan, reported by Nakazawa and Tsuji [37]. The scans, conducted by Julia Swies, were previously published in [65].



(a)



(b)

Figure 33: 3D scan of a SD-card, displayed as 2D element distribution (Ni for (a) and Cu for (b)) for different depths. The measurements were performed with a step size of $100 \mu m$ (in the x and y direction) and $15 \mu m$ (in the z direction), respectively, and a counting time of 15 s/point [65].

The resolution was further tested via the comparison of a measurement of a 3D gold structure previously measured with a different confocal setup by Tsuji and Nakano [66]. Figure 34 shows a schematic drawing of the structure including distance and dimensions of the structure.

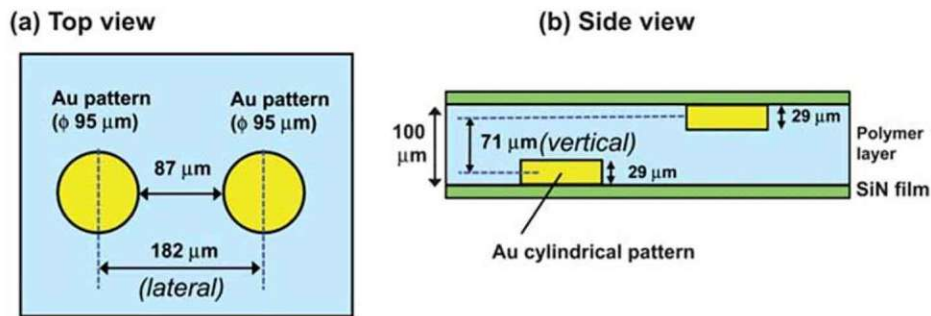


Figure 34: Schematic diagram of the top view (a) and the side view (b) of the 3D-structured Au material taken from [66].

The measurement results, measured with the Au-L lines (see figure 35), are in good agreement with the results previously published by Tsuji and Nakano [66]. The scan was conducted with vertical stepsize of $18.75 \times 18.75 \mu\text{m}$ and a horizontal stepsize of $7.5 \mu\text{m}$ and a live time of 20s per measurement point.

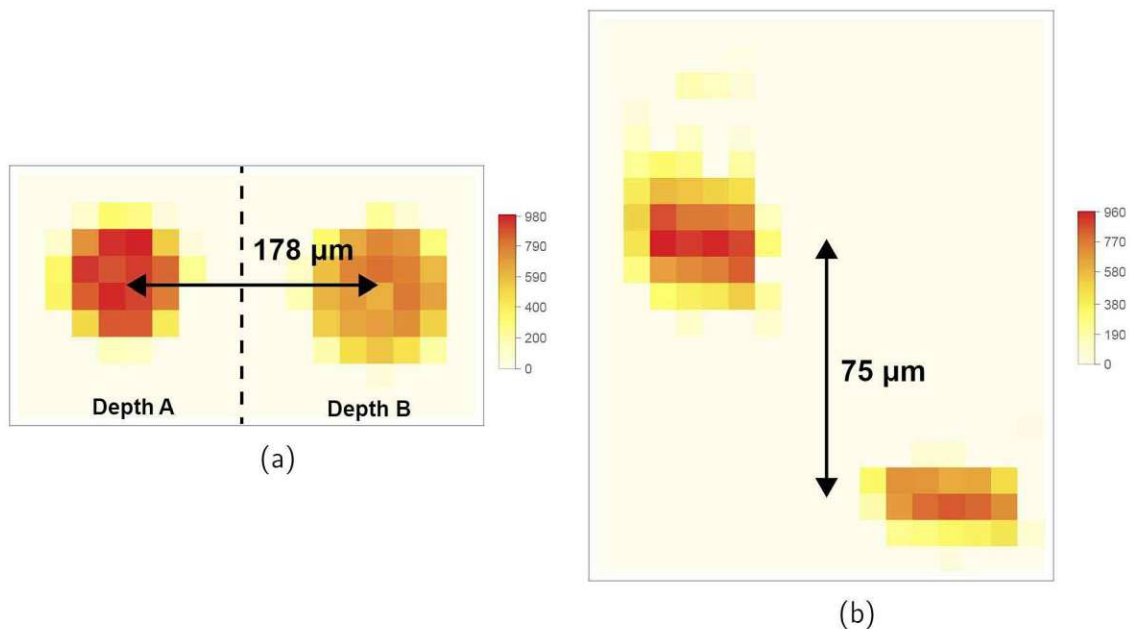


Figure 35: Heat map of the measured intensity of the Au-L lines of the top view, in the different depths were they perform (a) and the side view (b) of the 3D-structured Au material previously investigated by Tsuji and Nakano [66].

5.2 Investigation of polycapillary half-lenses

A vital issue for the quantitative interpretation of CMXRF measurements is the exact description of the transmission properties of polycapillary optics. Those properties were investigated for three different polycapillary optics in experiments at Atominstut and BESSY Synchrotron. Parts of the following section were previously published in [63].

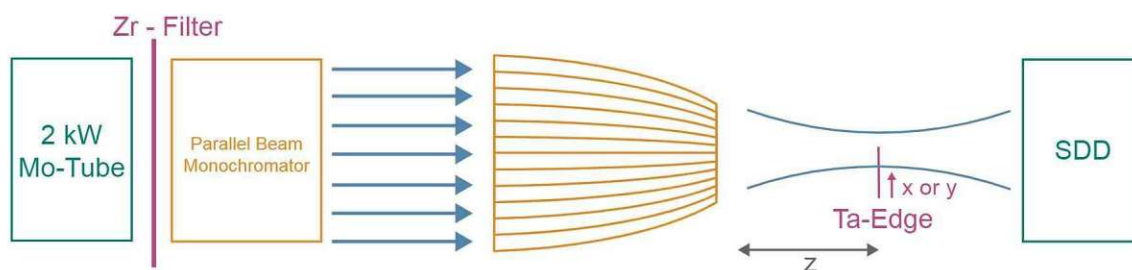
Data given by manufacturer (see table 5) is often insufficient for an exact modelling of the capillary optics.

	PC-236	PC-246	PC-50
Manufacturer	Fischer	Fischer	XOS
Serial number	246mls26	236mls13	5632
f (mm)	5.1	4.9	5.0
L (mm)	39.4	40.3	<50
D_{in} (mm)	7.4	6.35	7.4
D_{out} (mm)	2.15	1.9	
Spotsize 7.5-10 keV (μm)	25	25	
Spotsize 10-15 keV (μm)	17	20	
Spotsize 15-20 keV (μm)	14	15	
Spotsize 20-25 keV (μm)	14	15	

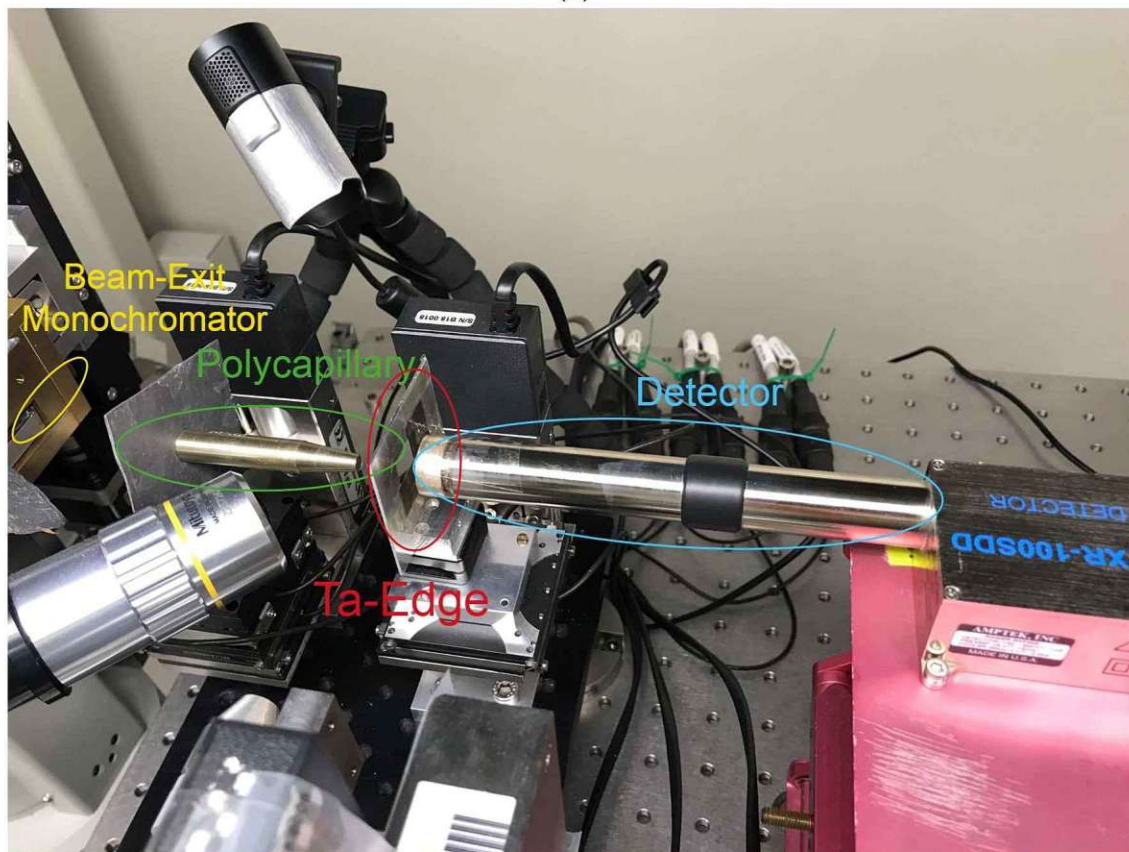
Table 5: Data given by the manufacturer for the investigated polycapillary optics.

5.2.1 Knife-edge scans

The polycapillary optics used in the setup described in 5.1 (PC-246 (primary polycapillary) and PC-236 (secondary polycapillary)) were investigated for their energy dependent transmission properties. Knife-edge scans were conducted to establish the beam size after the primary polycapillary. Figure 36 shows the adapted setup with a detector in the direction of the primary beam and a Ta cross structure to conduct knife-edge scans in vertical and horizontal direction. The tube was operated at lower power (50 kV and 5mA) to avoid count rates superseding the capabilities of the detector.



(a)



(b)

Figure 36: Sketch (a) and Foto (b) of the knife-edge scan setup at the Atominstytut of TU Wien. Previously published in [63]

The spectrum of the primary beam was measured with and without a thin Zr-filter, between tube and monochromator, to reduce continuous background. Figure 37 shows the measured spectra. While both spectra are not 100% monochromatic, the Zr-filter drastically reduces the continuous background (note the logarithmic scale) without taking to much of the overall intensity. The resulting spectrum can be considered nearly monochromatic, with 87% of the collected photons being in a very thin band between 16.84 keV and 17.72 keV.

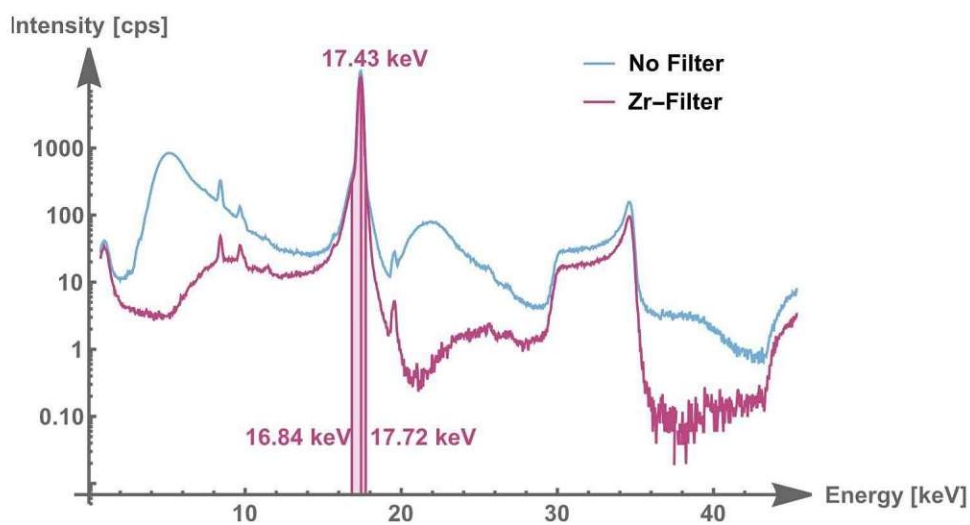


Figure 37: Beam spectrum in logarithmic scale with and without a Zr filter. The marked ROI holds approximately 87% of the total beam intensity. The X-ray tube was operated at 50 kV and 5 mA. Previously published in [63].

Beam size and shape can be established via the fit of different functions to the measured curves of the knife-edge scan. Similar investigations of different beam shape functions for wire scans are discussed in [67]. For the movement of the Ta knife-edge in x and y direction for a given distance z (see figure 36 (a)) the measured intensity curve can be considered a cumulative density function (CDF) for a given probability density function (PDF) representing the beam-shape. The probability density functions of the investigated distributions are:

- *Gaussian normal distribution:*

$$f(x) = \frac{1}{\sqrt{2\pi}} e^{-\frac{1}{2}\left(\frac{x-\mu}{\sigma}\right)^2} \quad (32)$$

with μ being the mean and σ the standard deviation of the distribution.

- *PERT distribution:*

$$f(x) = \begin{cases} \frac{(b-a)^{-1-\lambda} (b-(x-\mu))^{\frac{(-c+b)\lambda}{b-a}} (-a+(x-\mu))^{\frac{(c-a)\lambda}{b-a}}}{Beta\left[1+\frac{(c-a)\lambda}{b-a}, 1+\frac{(-c+b)\lambda}{b-a}\right]} & a < x < b \\ 0 & x < a \quad || \quad x > b \end{cases} \quad (33)$$

with a and b denominating the boundaries of the distribution, μ being the mean, Beta being the *Euler beta function* and the parameters c and λ determining the shape of the distribution. The parameters were chosen $c = 0$ and $\lambda = 4$ in the following.

- *Wigner semicircle distribution:*

$$f(x) = \begin{cases} \frac{2\sqrt{1-\frac{(x-\mu)^2}{r^2}}}{\pi r} & \mu - r < x < \mu + r \\ 0 & x < \mu - r \quad || \quad x > \mu + r \end{cases} \quad (34)$$

with r denominating the "width" of the distribution, and μ its center.

- *Truncated normal distribution:*

$$f(x) = \begin{cases} \frac{1}{\sqrt{2\pi}} e^{-\frac{1}{2}\left(\frac{x-\mu}{\sigma}\right)^2} & \mu - n \cdot \sigma < x < \mu + n \cdot \sigma \\ 0 & x < \mu - n \cdot \sigma \quad || \quad x > \mu + n \cdot \sigma \end{cases} \quad (35)$$

with n being 1,2 or 3, μ the mean and σ the standard deviation of the distribution.

- *Flat-top normal distribution:*

$$f(x) = \begin{cases} \frac{1}{\sqrt{2\pi}} e^{-\frac{1}{2}\left(\frac{x-\mu}{\sigma}\right)^2} & x < \mu - n \cdot \sigma \quad || \quad x > \mu + n \cdot \sigma \\ \frac{1}{\sqrt{2\pi}} & \mu - n \cdot \sigma < x < \mu + n \cdot \sigma \end{cases} \quad (36)$$

with n being 1,2 or 3, μ the mean and σ the standard deviation of the distribution.

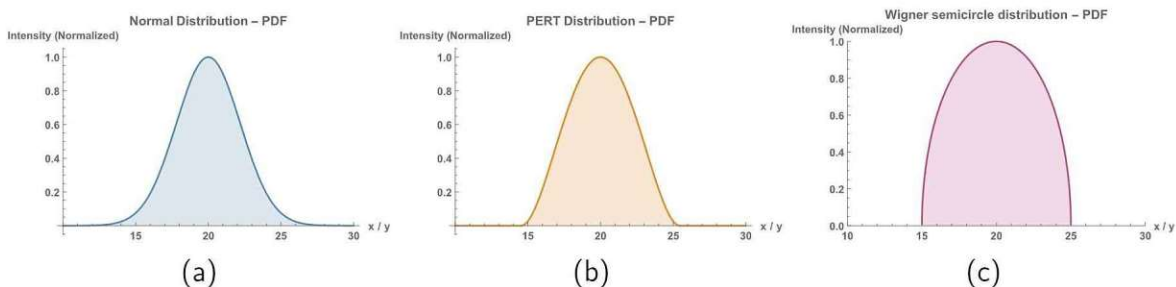


Figure 38: Probability density function representing the beam shape of a gaussian normal distribution (a), a PERT distribution (b) and a Wigner-semicircle distribution (c).

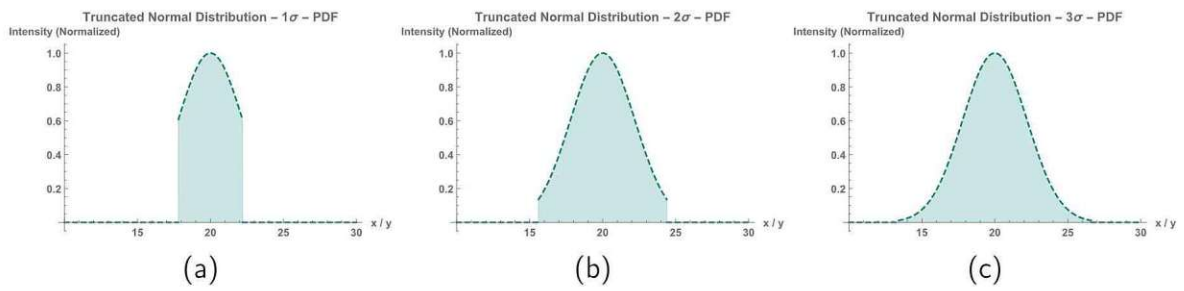


Figure 39: Probability density function representing the beam shape of a truncated normal distribution with a half-width of 1σ (a), 2σ (b), 3σ (c).

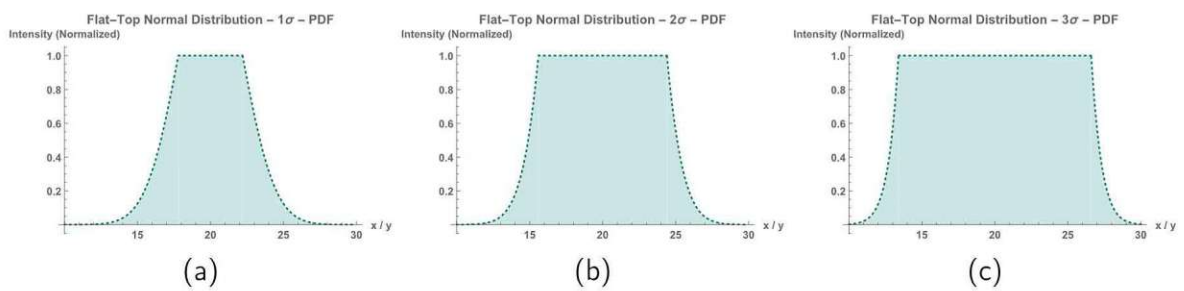


Figure 40: Probability density function representing the beam shape of a flat-top normal distribution with a half-width of 1σ (a), 2σ (b), 3σ (c).

Figures 41-43 show the according *cumulative density functions* (CDF) for the given distributions.

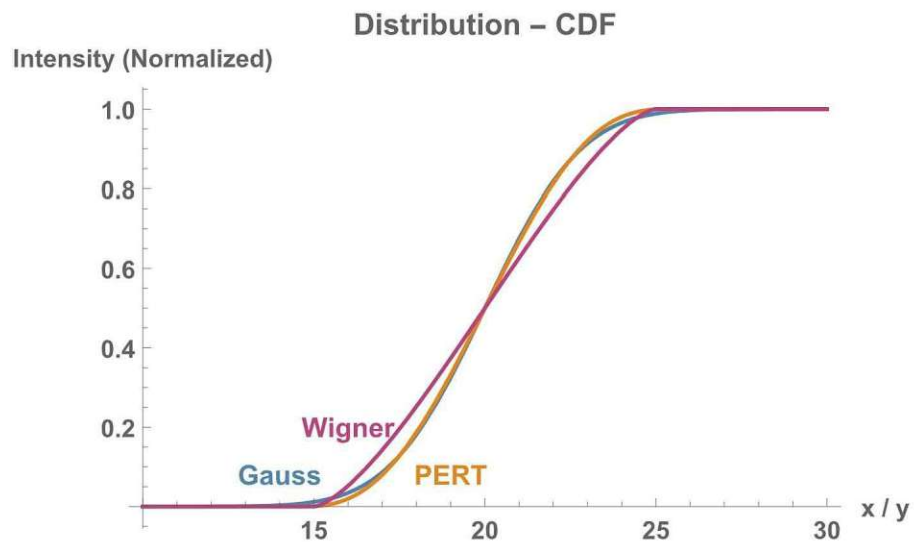


Figure 41: Cumulative density function representing the intensity profile of a knife-edge scan of a gaussian normal distribution (blue), a PERT distribution (orange) and a Wigner-semicircle distribution (red).

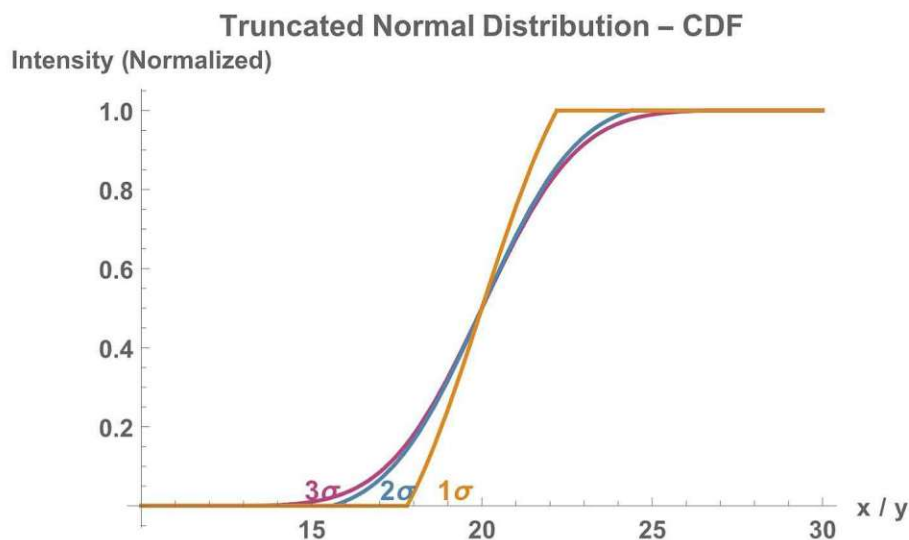


Figure 42: Cumulative density function representing the intensity profile of a knife-edge scan of a truncated normal distribution with a half-width of 1σ (orange), 2σ (blue) and 3σ (red).

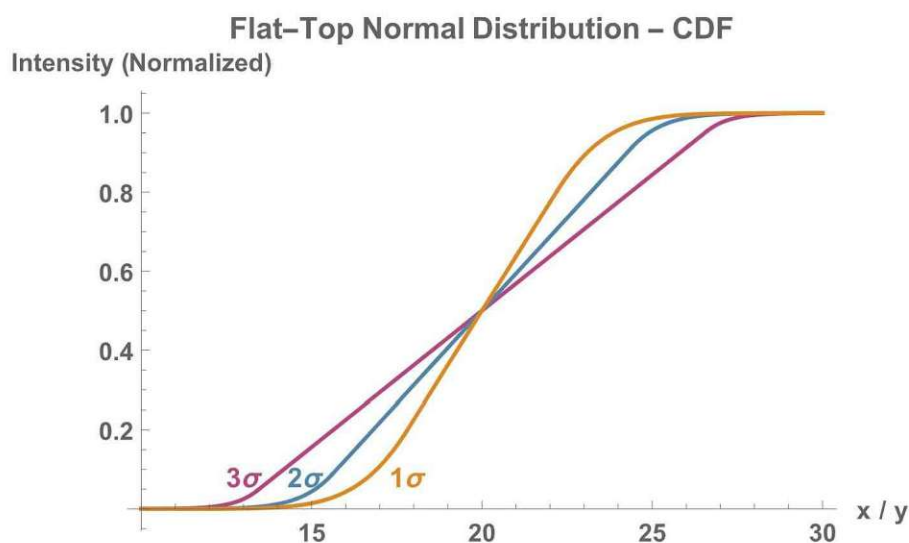


Figure 43: Cumulative density function representing the intensity profile of a knife-edge scan of a flat-top normal distribution with a half-width of 1σ (orange), 2σ (blue) and 3σ (red).

These CDFs were fitted to the intensity profiles of the knife-edge scans, using *Mathematica* [68]. The best fit results (see figure 44) were achieved with the gaussian normal distribution and the PERT distribution.

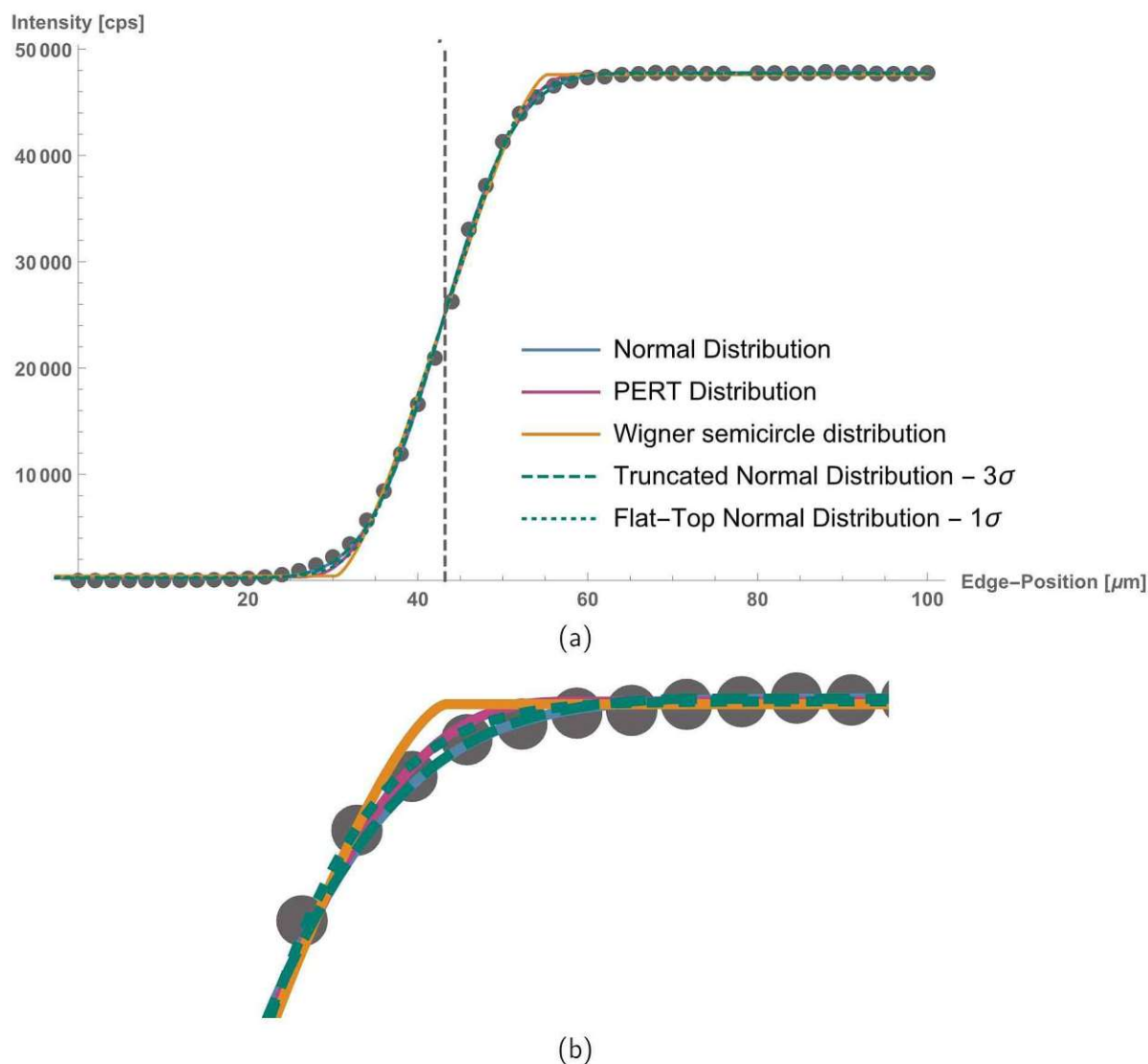


Figure 44: Fit of the cumulative density functions of a gaussian normal distribution (blue), a PERT distribution (red), Wigner semicircle distribution (orange), a truncated normal distribution with a half-width of 3σ (green, dashed) and a flat-top normal distribution with a half-width of 1σ (green, dotted) to the intensity profile measured in the knife-edge scan in vertical direction (a) and enlarged area of varying fit-quality (b).

The results for the spotsize of the beam are shown in table 6. The spotsize for the normal and PERT distribution is given as the full width half maximum (FWHM). Spotsizes for truncated and flat-top normal distribution are given as $2.355 \times \sigma$, which should be a fitting equivalent to the FWHM of the normal distribution. The width of the wigner semicircle distribution is given as the established free fit parameter r .

	Vertical [μm]	Horizontal [μm]
Normal distribution	16.36	16.17
PERT distribution	16.36	16.18
Wigner semicircle distribution	12.47	12.36
Truncated normal distribution - 3σ	16.43	16.24
Flat-Top normal distribution - 1σ	14.19	14.02

Table 6: Spotsizes established by the fit results for knife edge scans in horizontal and vertical direction, in focal distance. The spotsize is given as full width half maximum (FWHM) for the normal and PERT distribution, as $2.355 \times \sigma$ for truncated and flat-top normal distribution and as the established free fit parameter r for the Wigner semicircle distribution.

Due to very similar fit results, it is hard to discern in this setup any differences, between PERT distribution, normal distribution, or truncated normal distribution. The results show that a typical gaussian normal distribution is a very good fit for the shape of the beam, and due to it's simplicity for calculations an ideal candidate for the approximation of the beam shape. A beam size of $\sim 16.5 \mu m$ for the "monochromatic" energy of 17.4 keV was established.

For a further investigation of the energy-dependence of the beam dimensions the spectral distribution of the primary beam can be used to perform fits using a gaussian normal distribution as described above for each individual energy channel of the detector (see figure 45).

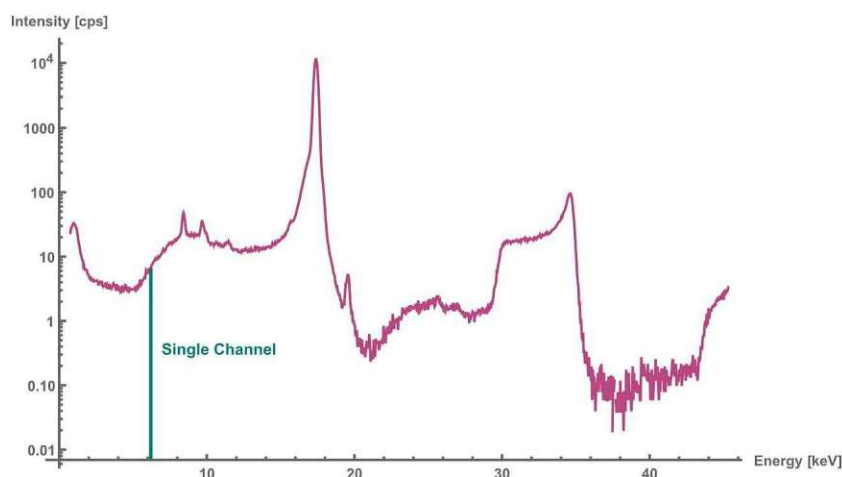


Figure 45: Energy dependent evaluation, via the investigation of single energy channels of the detector.

Figure 46 shows the results of the fits of selected channels, for a knife-edge scan in focal distance in horizontal direction.

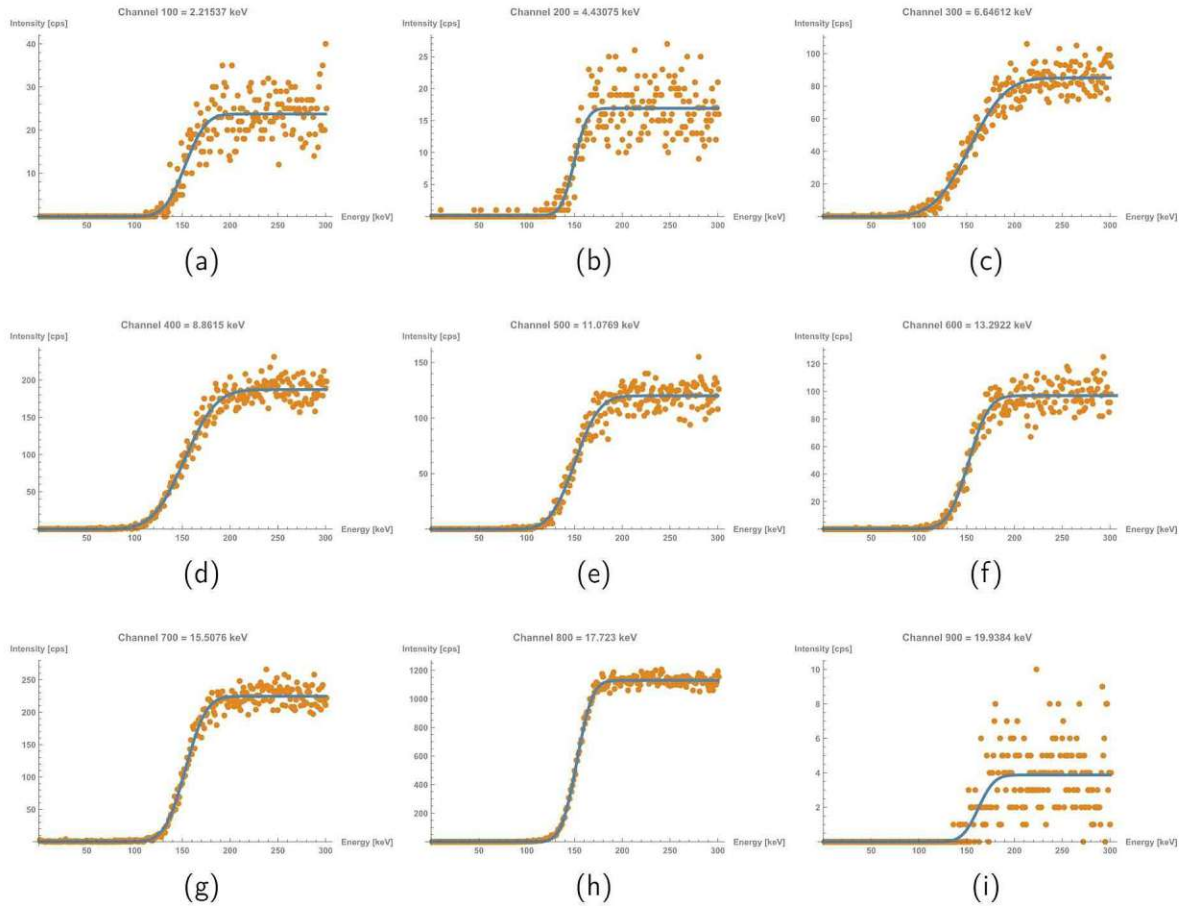


Figure 46: Fit of the cumulative density function of a gaussian normal distribution to the intensity curves measured in a knife-edge scan in focal distance in horizontal direction for single energy channels.

The results for very low (see figure 46 (a) and (b)) and very high energies (see figure 46 (i)) can be considered arbitrary due to low count rate in this spectral band. The low count rate results into a strong variation of the measured intensity for positions of the knife edge outside the detected beam. Therefore this evaluation is only applicable for a limited energy range, for which statistical relevance can be achieved. Figure 47 shows the evaluated FWHM in the focal distance in respect to energy, showing clearly the spectral band for which statistical relevance of the fits could be achieved (between 6.2 keV and 18.05 keV). Figure 47 also shows that the energy dependent evaluations for knife-edge scans in horizontal and vertical direction indicate good symmetry of the beam in the focal spotsizes.

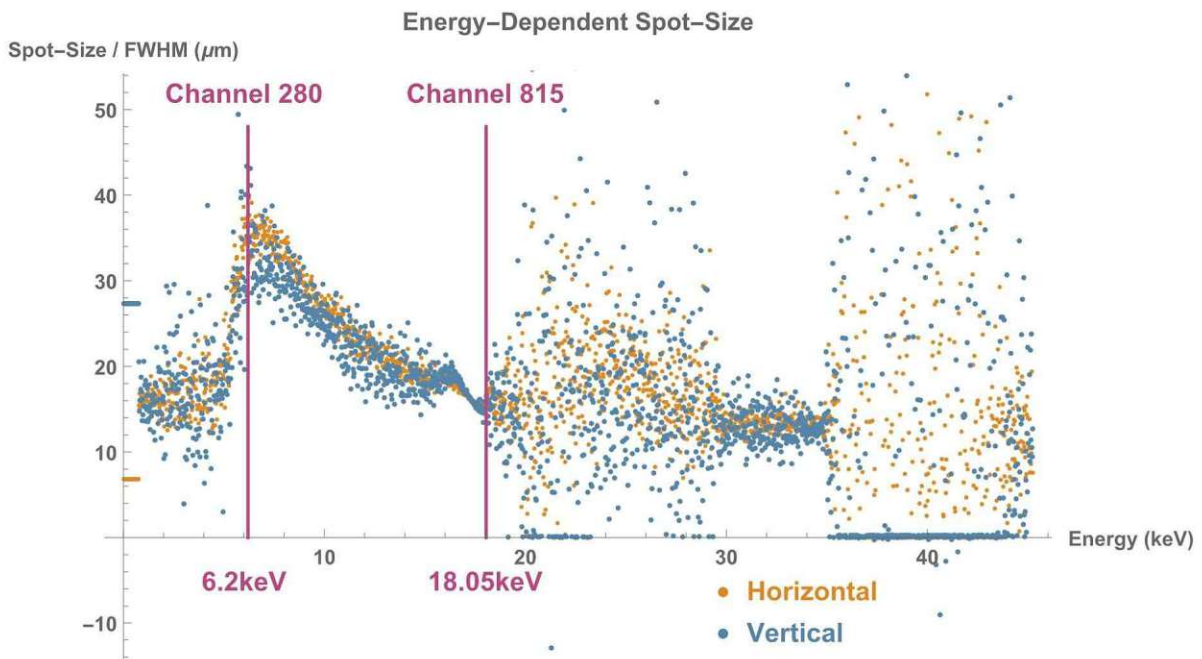


Figure 47: Fit results for the energy dependent spotsize in focal distance for horizontal (orange) and vertical (blue).

The energy range for a statistically relevant signal is in good accordance with the measured spectrum (see figure 48), with very small countrates outside this energy band.

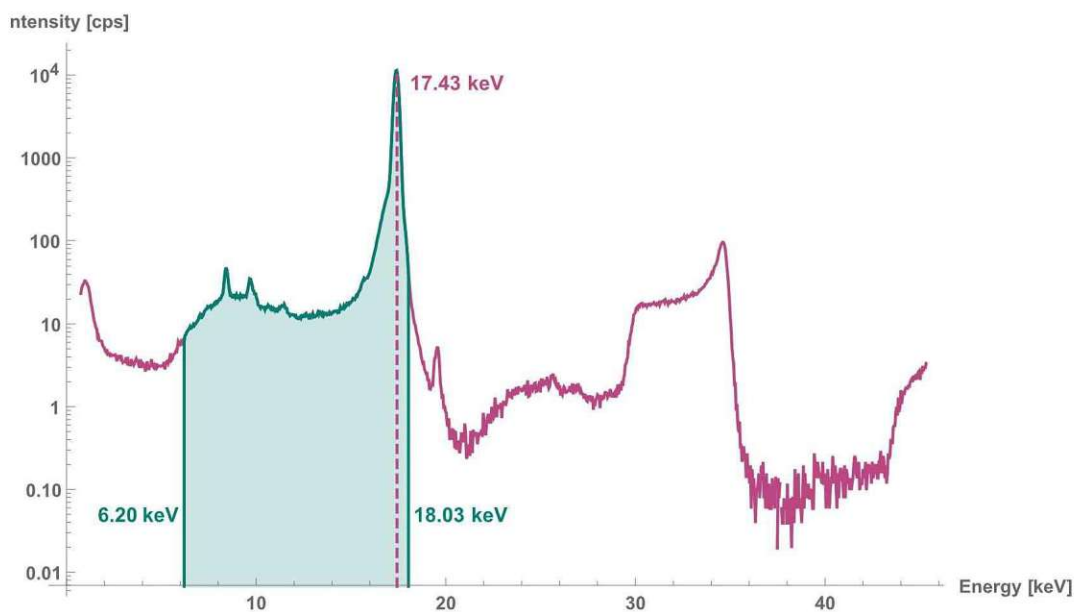


Figure 48: Primary spectrum with marked area for which single channel evaluation is statistically relevant.

The spot size in the focal distance can be estimated with the parameters of a single capillary. Such an estimate for the lower boundary of the spot size d_{LB} , neglecting misorientation of the capillaries, can be written as

$$d_{LB} = d_{SC} + 2\theta d_W \quad (37)$$

with d_{SC} being the diameter of a single capillary, θ the dominant angle of reflectance and d_W the distance between capillary and the spot, i.e. the focal distance of the polycapillary optic (see figure 49).

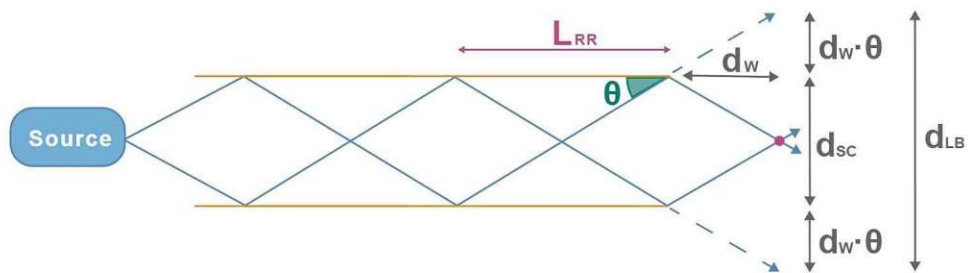


Figure 49: Multiple reflections and estimates of a lower boundary for the spot size close to the focal distance of a straight monocapillary optic. Previously published in [63].

The dominant angle of reflection θ is much smaller than the critical angle of total reflection θ_C (see equation 8). This can be explained by the large number of reflections inside the capillary (in the case of the polycapillary optics PC-236 and PC-246 40). The reflectivity for multiple reflections of X-rays with an energy of 17.4keV is shown in figure 50.

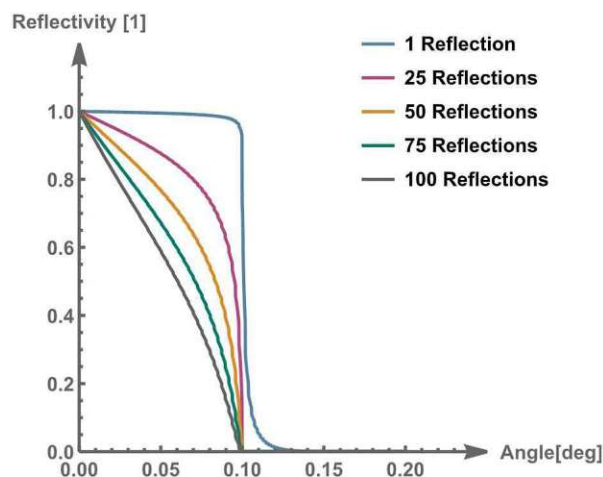


Figure 50: Calculated total reflectivity for a reflection on an SiO₂ surface for multiple reflections of X-rays with an energy of 17.4 keV. Previously published in [63].

A comparison of the measurement results in vertical and horizontal direction, with data given by the manufacturer as well as an estimate for the lower boundary of the spot size with a dominant angle of reflection $\theta = 0.65\theta_C$ is shown in figure 51.

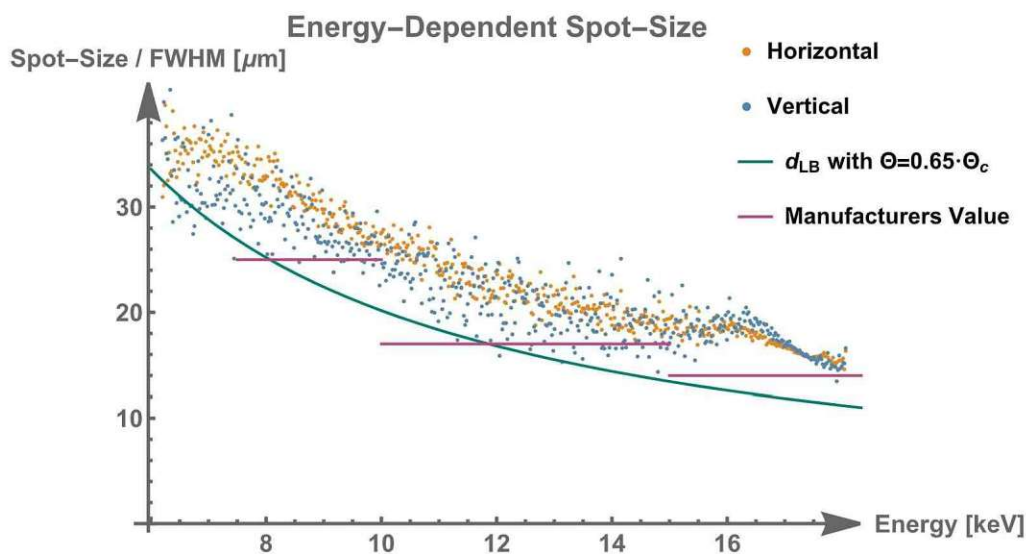


Figure 51: Energy-dependent spot size of PC-246 in the focal distance for horizontal and vertical knife-edge scans. Previously published in [63].

This shows that, while the results generally agree well with estimations and data given by the manufacturer, an exact investigation of the used optics is necessary to minimize errors in quantification. To investigate the local beam divergence knife edge scans were conducted for different distances (100 μm steps) between edge and capillary optic (see z in figure 36 (a)).

The spot size as a function of distance to the focal spot shows a hyperbolic shape (see figure 52).

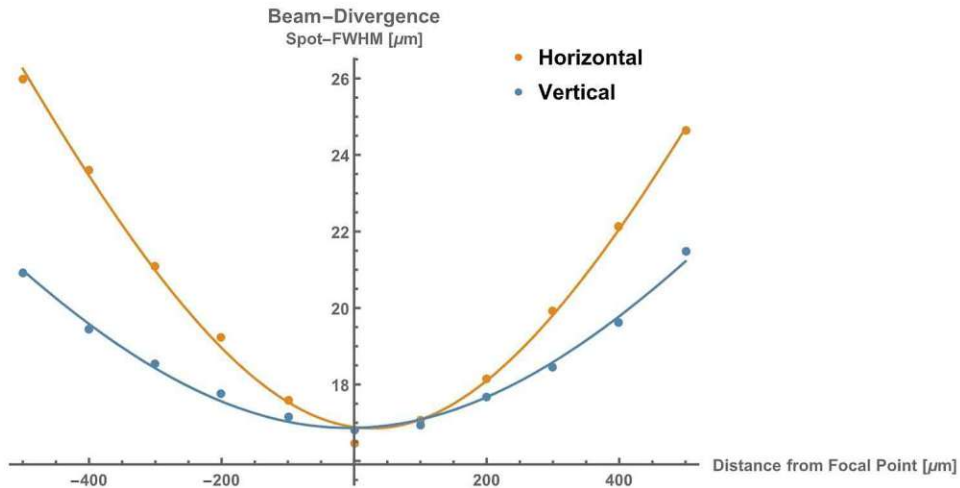


Figure 52: Beam divergence as a function of distance to the focal spot.

The local divergence (near focal distance) of the beam profile is dominated by the dimensions of a single capillary (see figure 49) in the bunch of capillaries. For the full investigation of the polycapillaries, capillary misalignment and manufacturing imperfections have to be considered. The large difference between the horizontal and vertical divergence can be explained by an asymmetrical shape of the single capillaries. This shows that even small misalignments can have an impact on the spotsize of a polycapillary optic, and thus on the size, shape and orientation of the investigated confocal volume (see also section 4.3). Furthermore the divergence of the beam is again an energy dependent quantity. Figure 53 shows the measured divergence of the beam for three different energies.

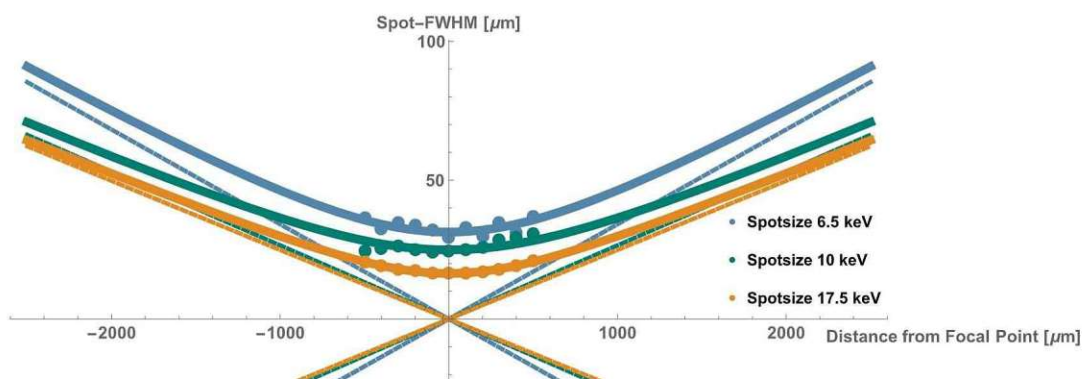


Figure 53: Vertical energy dependent beam divergence as a function of distance to the focal spot.

The parameters for the hyperbolic fit, describing the local divergence for different energies are shown in table 7.

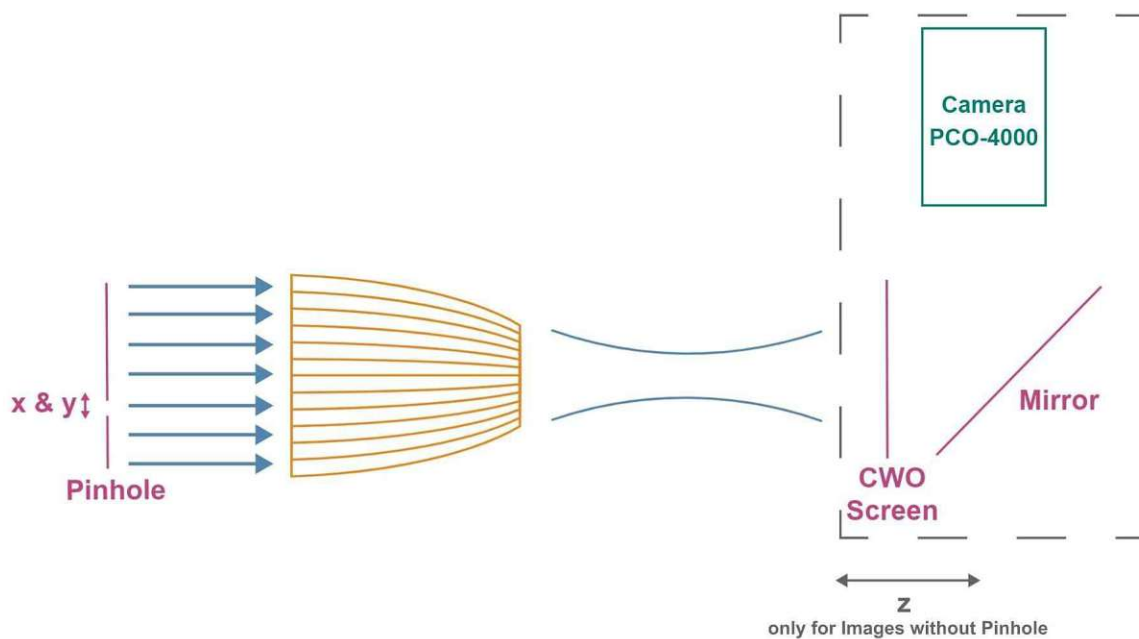
Energy [keV]	a_v [μm]	b_v [μm]	$k_v = a_v/b_v$ [μm]	a_h [μm]	b_h [μm]	$k_h = a_h/b_h$ [μm]
6.5	31.3	917.8	0.034	33.0	516.6	0.064
8	28.3	775.3	0.037	31.2	555.4	0.056
10	24.9	938.8	0.027	27.2	579.1	0.047
12	21.7	731.0	0.030	22.2	521.6	0.043
14	18.4	608.3	0.030	19.5	439.5	0.044
17.5	16.4	659.6	0.025	16.4	425.1	0.038

Table 7: Fit results for knife edge scans in focal distance in vertical (left) and horizontal (right) direction for different energies. The parameters a and b are established with a hyperbolic fit to the measurement data so that a gives the minimum of the hyperbola, i.e. the minimal spotsize and $\frac{a}{b}$ gives the ascent of the asymptote of the hyperbola.

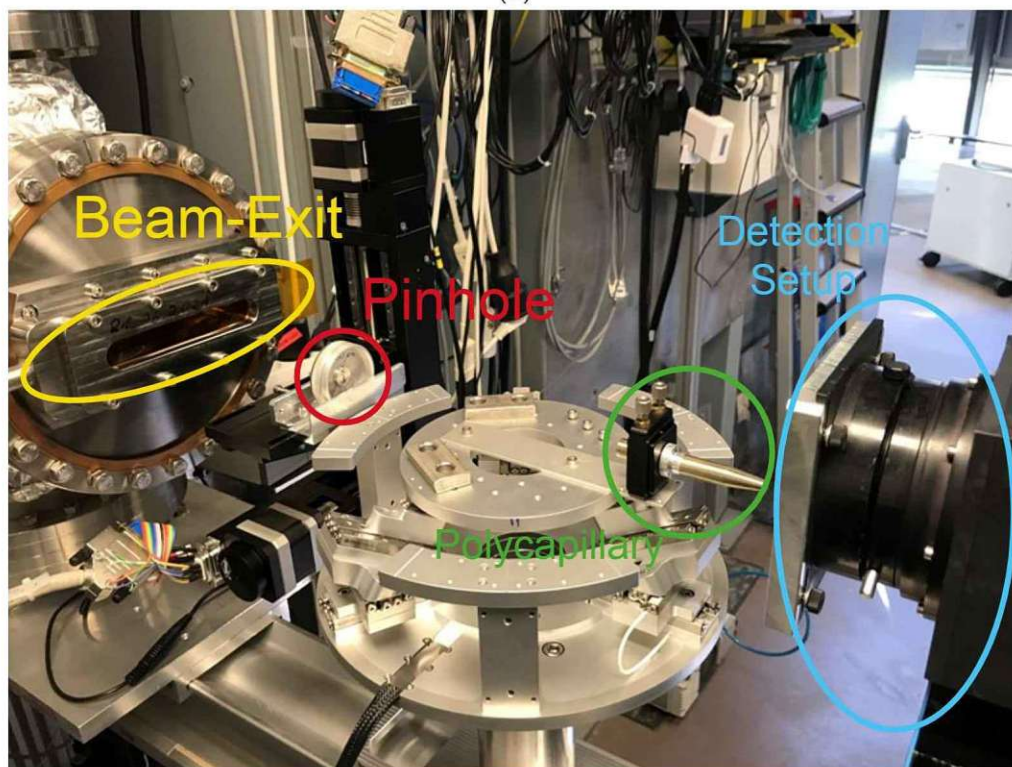
The values for $k = \frac{a}{b}$ describe the local divergence as the slopes of the asymptotes of the hyperbolas.

5.2.2 Images and Pinhole-Scans

Further experiments investigating beam shape and possible manufacturing imperfections were conducted at the Bamline beamline at the BAMline beamline at the BESSY II Synchrotron of the Helmholtz-Zentrum-Berlin. The monochromatic parallel beam was directed at the capillary optic, with the beam from the capillary directed at a cadmium tungstate (CWO) screen and a mirror reflecting the luminescent signal of the beam on the screen to a Camera (see figure 54). The setup was used to collect pictures of the beam for a fully irradiated polycapillary entry window, with different distances (in mm steps) between polycapillary exit window and CWO screen. Furthermore partial irradiations were realized with a pinhole (diameter $250 \mu\text{m}$) located between beam exit and capillary optic, to investigate small manufacturing errors and reduce smearing effects of the collected beam, resulting from misorientation of single capillaries or capillary bunches. Different pinhole positions for movement in the plane of the polycapillary entry window were taken, to combine pictures of single pinhole positions to an image of the full beam, showing possible manufacturing defects.



(a)



(b)

Figure 54: Sketch (a) and foto (b) of the experimental setup for the far from focal-distance investigation on the BAMline beamline at the BESSY II synchrotron, at the HZB. Previously published in [63]

The captured images for full irradiation of the capillary entry window show the hexagonal bunch structure of the polycapillary optics very well (see figure 55).

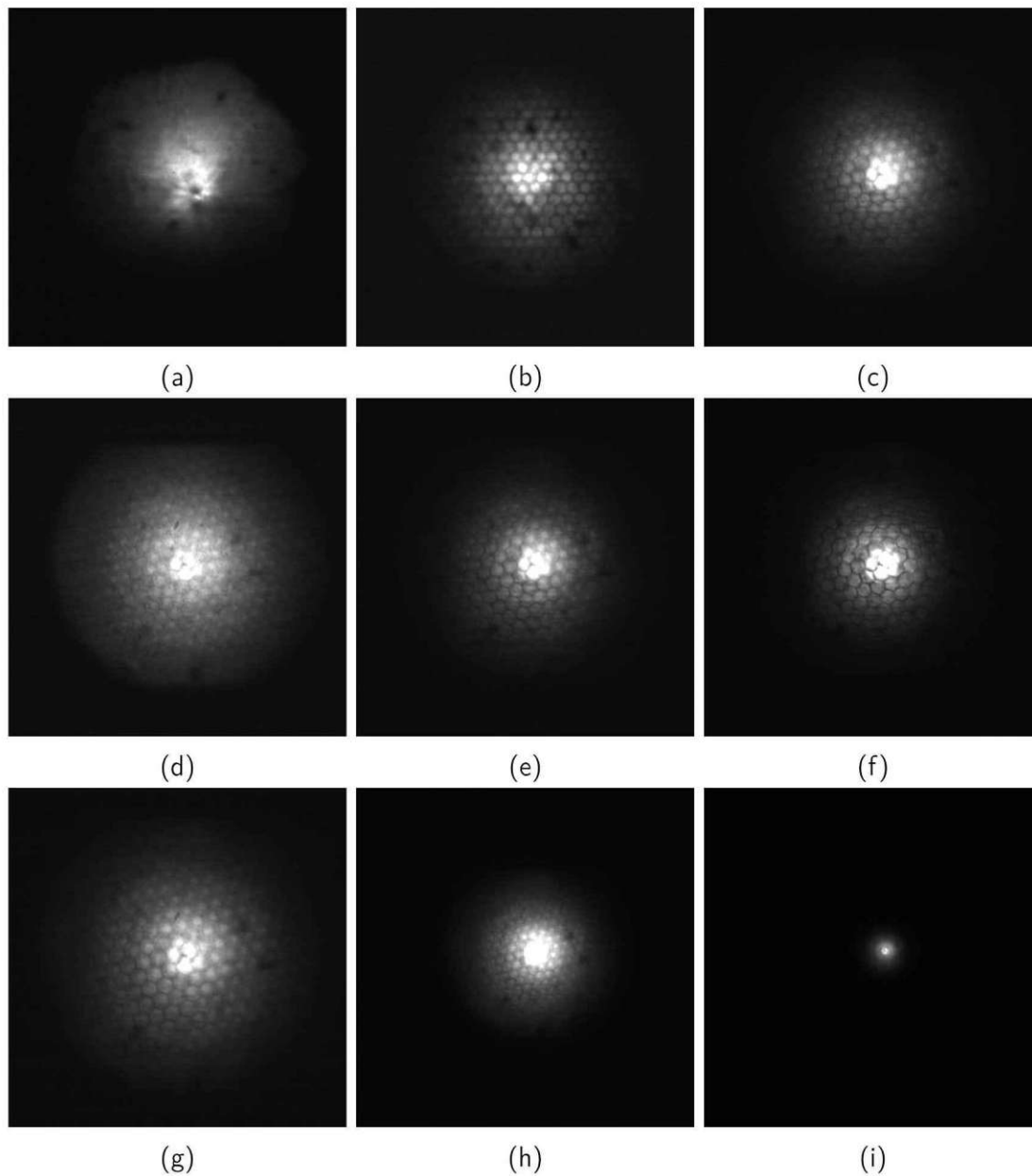
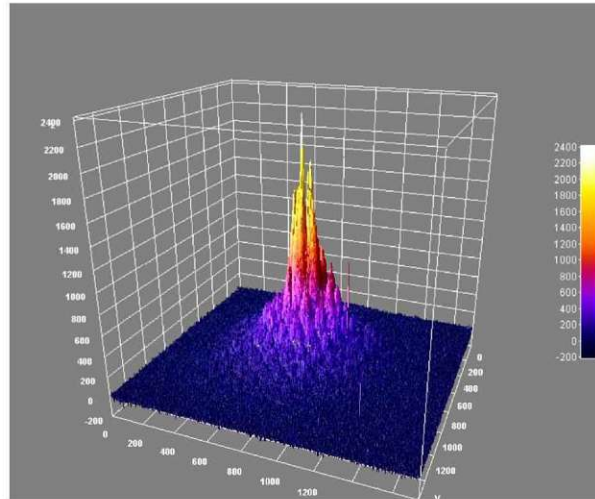
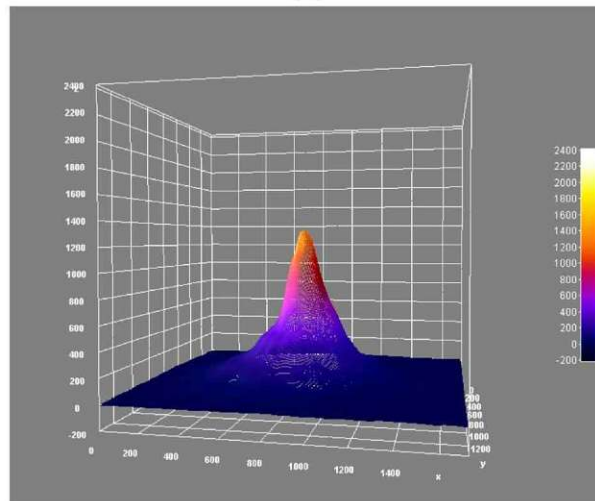


Figure 55: Beam intensity distribution for a primary beam energy of 12 keV for three different polycapillary optics PC-50 (a), PC-236 (b) and PC-246 (c). Beam intensity distribution for PC-246 for the primary beam energies 8 keV (d), 12 keV (e) and 17.5 keV (f). Beam intensity distribution for PC-246 for the primary beam energy 10 keV for different distances (see z in figure 54 (a)). With 6 mm distance between (g) and (h) and 6 mm distance between (h) and (i). Previously published in [63]

This setup allows a much more detailed investigation of the polycapillary half-lens and the shape of the beam transmitted by them. A three-dimensional illustration of the captured picture of the beam intensity distribution for PC-246 for 12 keV is shown in figure 56. The images were created with *ImageJ* [69].



(a)



(b)

Figure 56: 3D beam intensity distribution for PC-246 for the 12 keV primary beam unsmoothed (a) and smoothed (b). Previously published in [63]

The application of a smoothing algorithm, as shown in figure 56 (b), shows that a multivariate gaussian normal distribution is a good candidate to describe the shape of the beam. This is in good agreement with the evaluations from section 5.2.1. Center and standard deviation of the two dimensional normal distribution of the intensity, i.e. brightness of the captured pictures

were established with a python routine based on an algorithm calculating the moments of the data and optimizing the initial guesses for the parameters of the distribution [70]. The result of such a fit is shown in figure 57.

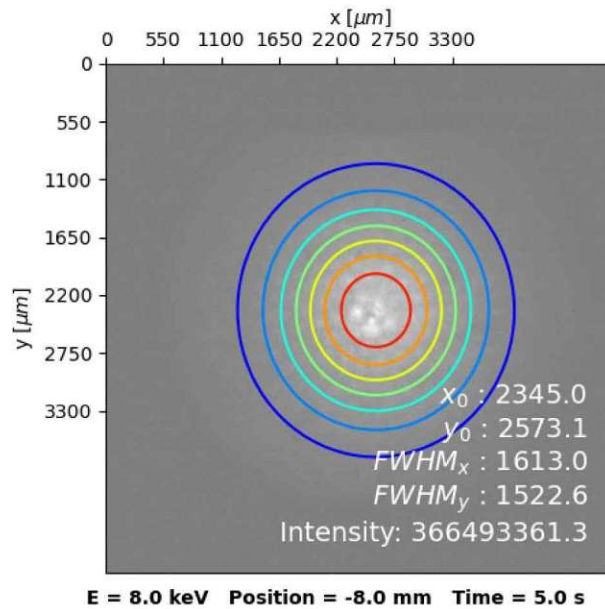


Figure 57: Fitted multivariate normal distribution parameters. Previously published in [63]

The established parameters of the 2D normal distribution can be used to determine the global divergence of the polycapillary optic. In addition to the energy dependence of the local divergence (see above), the global divergence is further dependent on the curvature of the optic [71] (see figure 58).

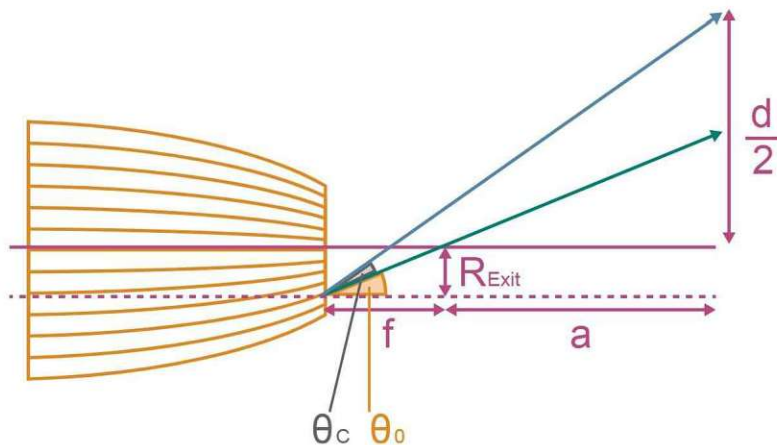


Figure 58: Sketch of the divergence far from focal distance. Previously published in [63]

The spot-size for a beam far outside the focal distance d can be written as

$$d(E) = \frac{2\{(f + a)\tan[\theta_0(E) + \theta_C(E)] - R_{Exit}(E)\}}{a} \quad (38)$$

with f being the focal distance, a the distance of the measured spot to the focal distance, $\theta_0(E)$ the angle between the tangent to the curvature radius at the polycapillary exit and the optical axis, $\theta_C(E)$ the critical angle for the given energy and $R_{Exit}(E)$ the distance between the optical axis and the 'outermost' capillary with a relevant transmission for a given energy E . Considering a large a and small $\theta_0(E)$ and $\theta_C(E)$ this can be simplified to

$$d(E) = 2 \left[\frac{R_{Exit}(E)}{f} + \theta_C(E) \right] \quad (39)$$

with

$$\theta_0(E) = \tan \left(\frac{R_{Exit}(E)}{f} \right) \approx \frac{R_{Exit}(E)}{f} \quad (40)$$

Considering the lower number of outer capillaries with a relevant transmission, R_{Exit} turns out to be proportional to the inverse energy E .

$$R_{Exit}(E) \propto \frac{R_{Out}}{E} \quad (41)$$

For a given energy and different distances of the capillary optic to the screen the global divergence can be established with a linear fit, shown in figure 59 for the polycapillary PC-246. The spot sizes are established using the FWHM of the fit results for the 2D normal distribution as shown in figure 57. The linear progression in figure 59 is in good accordance with the picture of a hyperbolic beam-shape with a close to linear asymptotic progression far outside the focal distance. Establishing the slope of the the linear fits the energy dependence of the divergence can be depicted as shown in figure 60 showing the expected progression from equation 41.

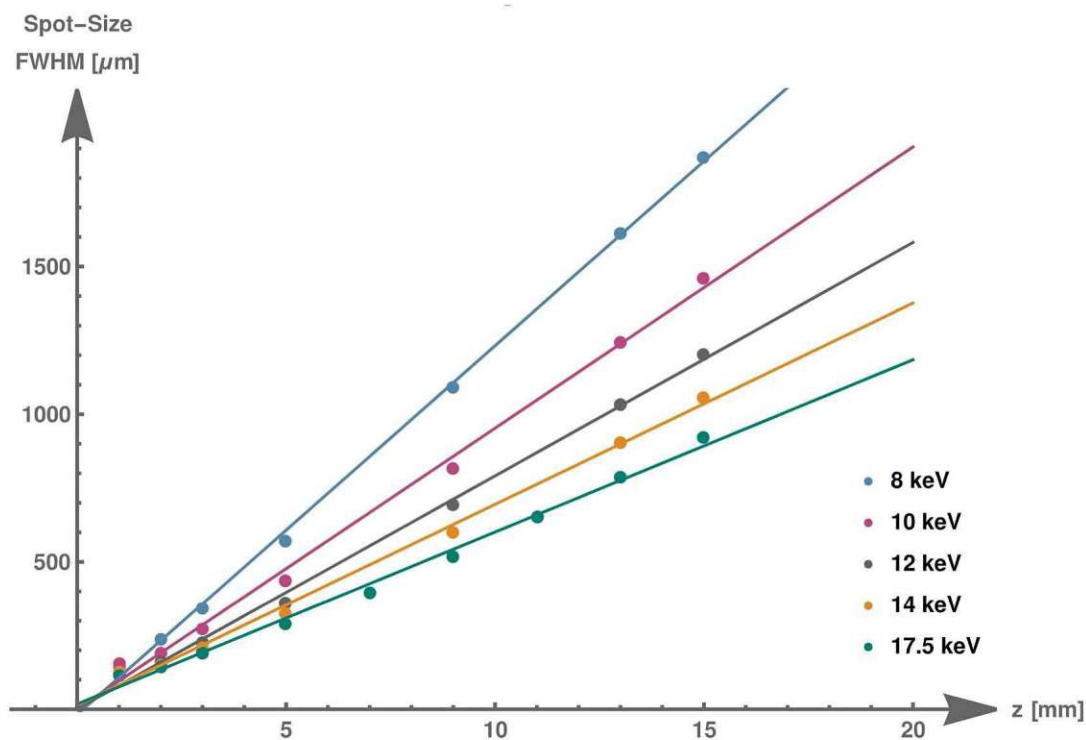


Figure 59: Divergence far from the focal distance of PC-246 for different energies. Previously published in [63]

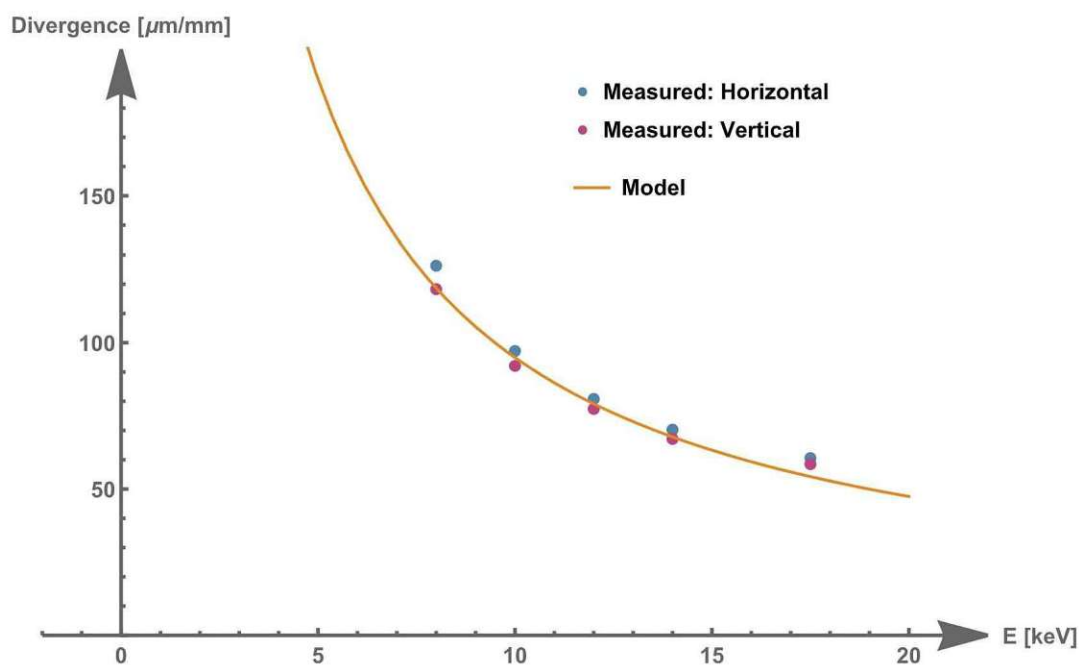


Figure 60: Energy dependence of the global divergence. Previously published in [63]

To investigate possible fabrication defects of the polycapillary optics, without smearing effects from different parts of the polycapillary optics, pinhole scans were conducted with a pinhole diameter of $250\ \mu\text{m}$ in front of the capillary optic (see figure 54). The resulting images (see figure 61 (a)) were combined to an image of the full beam adding the maximum value of each pixel of each image for a different pinhole position (see figure 61 (b)).

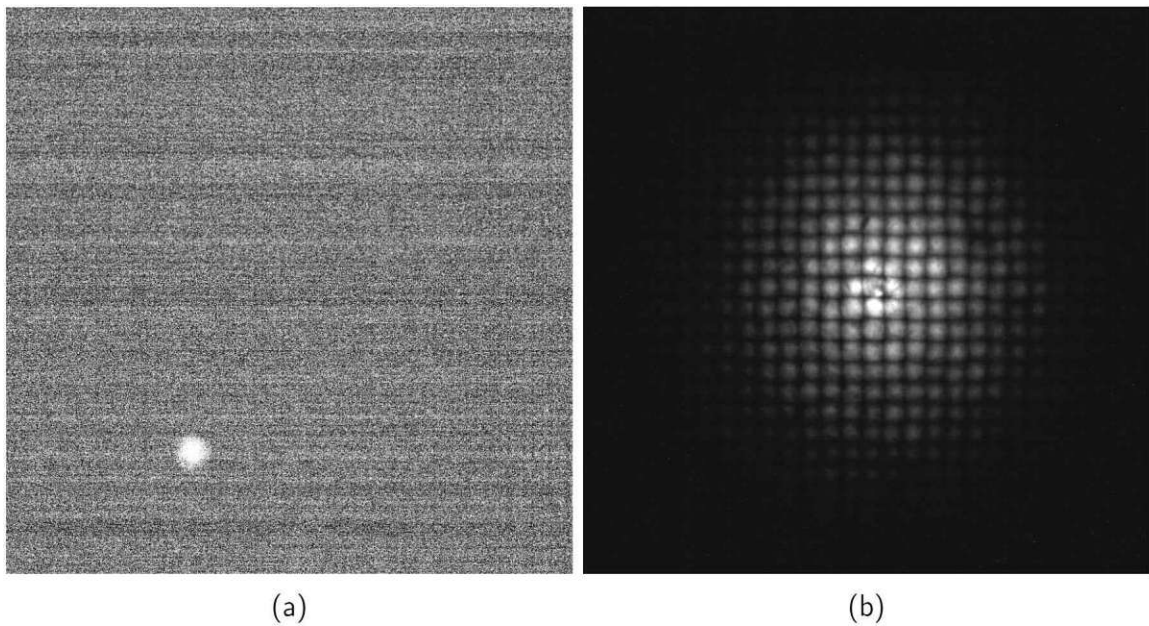


Figure 61: Pinhole scans for PC-246 at a beam energy of 8 keV. Image of a single pinhole position (a). Combined image of different pinhole positions (b). Previously published in [63]

The images of the total beam, combining images of different pinhole positions are in good agreement with the images taken of the full beam, showing a similar shape. To distinguish the artefacts from fabrication defects from artefacts of the primary beam intensity, only aberrations visible for different primary energies are considered fabrication defects. Two (PC-50 and PC-236) of the three investigated optics showed small fabrication defects (see figure 62 for PC-50). The slightly mangled form of the total beam can be explained by a small tilt of the optic in respect to the parallel primary beam. This effect is stronger represented for higher energies. Overall all investigated optics show a good quality of fabrication. The assumption of a multivariate normal intensity distribution of the beam is therefore justified.

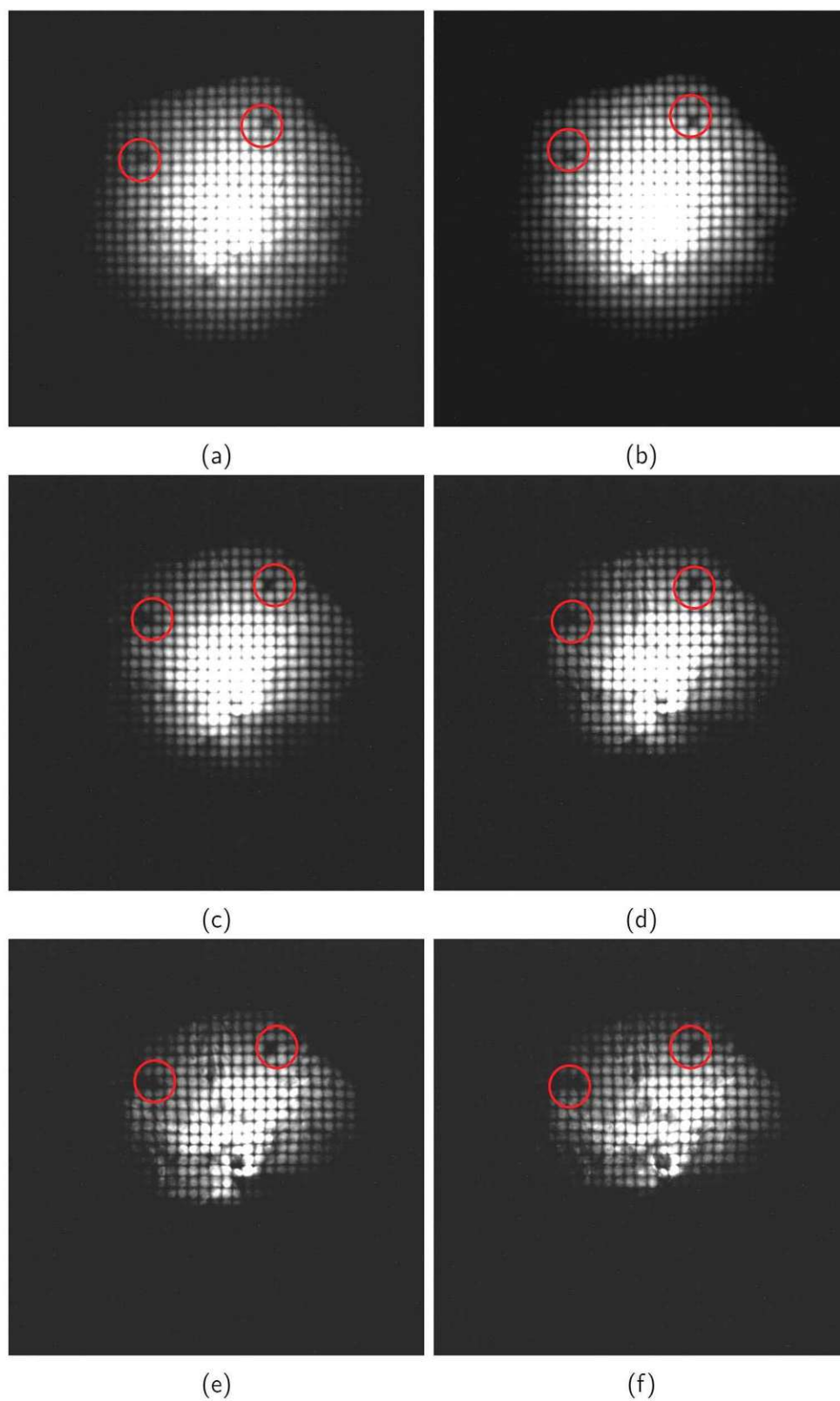


Figure 62: Small fabrication defects of PC-50 identified at beam energies (top-left to bottom-right) of 8 keV (a), 10 keV (b), 12 keV (c), 14 keV (d), 17.5 keV (e), 20 keV (f). Previously published in [63]

5.2.3 Transmission

The following analytical model for the transmission of a polycapillary half-lens was previously published in [63]. The dominant factors for the shape of the transmission function of a polycapillary half-lens are the average number of reflections of an X-ray inside the capillary, the number of X-rays hitting the surface in outer capillaries and the number of rays hitting the surface of the glass capillary in an angle larger than the critical angle on the first reflection. The number of reflections is especially important for photons with a low energy. The ratio of rays initially absorbed due to their angle being larger than the critical angle is the dominant effect for high energetic photons. Thus the overall transmission can be written as a product of functions considering the dominant effects of the low-energy and high-energy regime.

$$T(E) = F_{low-energy}(E) \cdot F_{high-energy}(E) \quad (42)$$

Taking a look at the high-energy function, i.e. the photons hitting the capillary under an angle larger than the critical angle, one has to consider the curvature of the capillaries inside the polycapillary optics. The curvature radius of a single capillary R_C (see figures 63 & 64) can be written as

$$R_C(x) = \frac{4[x(R_{In} - R_{Out})]^2 + (2L)^2}{8[x(R_{In} - R_{Out})]} \quad (43)$$

with R_{In} and R_{Out} being the upstream- and downstream-radius of the polycapillary optic and x the ratio of the distance of the single capillary with the curvature radius R_C to the optical axis.

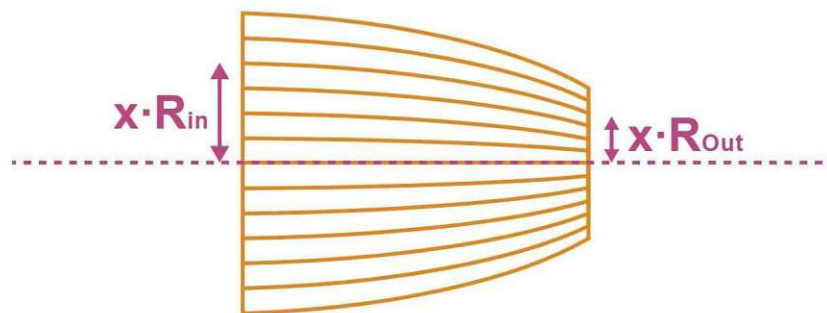


Figure 63: Parametrization of the polycapillary optic. Previously published in [63]

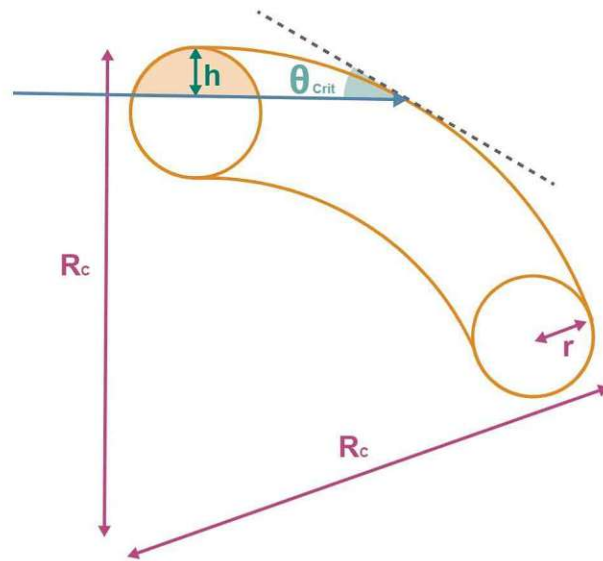


Figure 64: Sketch of the bending radius of a single capillary. Previously published in [63]

For a beam perfectly parallel to the optical axis the height $h(E, x)$ of the Area $A(r, h(E, x))$ illuminated with X-rays, with the energy E fulfilling the critical condition (see figure 63) can be written as

$$h(E, x) = (1 - \cos[\theta_{crit}(E)]) \cdot R_C(x) \quad (44)$$

where $\theta_{crit}(E)$ is the critical angle. The illuminated area $A(r, h(E, x))$ can be further written as

$$A(r, h(E, x)) = r^2 \cdot \cos^{-1} \left[1 - \frac{h(E, x)}{r} \right] - (r - h(E, x)) \cdot \sqrt{2 \cdot r \cdot h(E, x) - h(E, x)^2} \quad (45)$$

with r being the entrance radius of a single capillary. The overall Transmission Function for high-energy effects for the complete polycapillary can then be calculated by the sum of the fractions of the illuminated area fulfilling the critical condition $A[r, h(E, x)]$ and the overall illuminated area of a single capillary $r^2\pi$. Considering the fact that the number of single capillaries increases with the distance to the optical axis x , the sum can be written as the integral

$$F_{High-Energy} = \int_0^1 \frac{A[r, h(E, x)]}{r^2\pi} x dx \quad (46)$$

The low energy part of the transmission can be written as

$$F_{Low-Energy} = [R(E, \theta)]^{n_{Ref}(E, \theta)} \quad (47)$$

with $R(E, \theta)$ being the reflectivity of an X-ray with the energy E hitting a surface of the capillary under the angle θ . As shown in figure 50 the dominant angle of reflection is reduced to an angle smaller than the critical angle for multiple reflections. The number of reflections $n_{Ref}(E, \theta)$ of a ray with the angle of incidence θ and an energy E can be estimated by the number of reflections in a straight monicapillary (see figure 49).

$$n_{Ref}(E, \theta) = \frac{L_{Cap}}{L_{RR}} = \frac{L_{Cap}}{(d_{Cap}/\tan(\theta))} \simeq \frac{L_{Cap}}{d_{Cap}} \theta \quad (48)$$

The expected value for the dominant angle of reflection can be estimated using the reflectivity $R(E, \theta)$ as a weight function of the angle θ .

$$\int_{-\infty}^{\infty} w(\omega) \omega d\omega \simeq \int_0^{\theta_{Crit}} R(\theta, E) \theta d\theta \propto \frac{1}{E^2} \quad (49)$$

The calculated model is in very good agreement with measurement results and beam dimensions simulated with polycap (see figure 65).

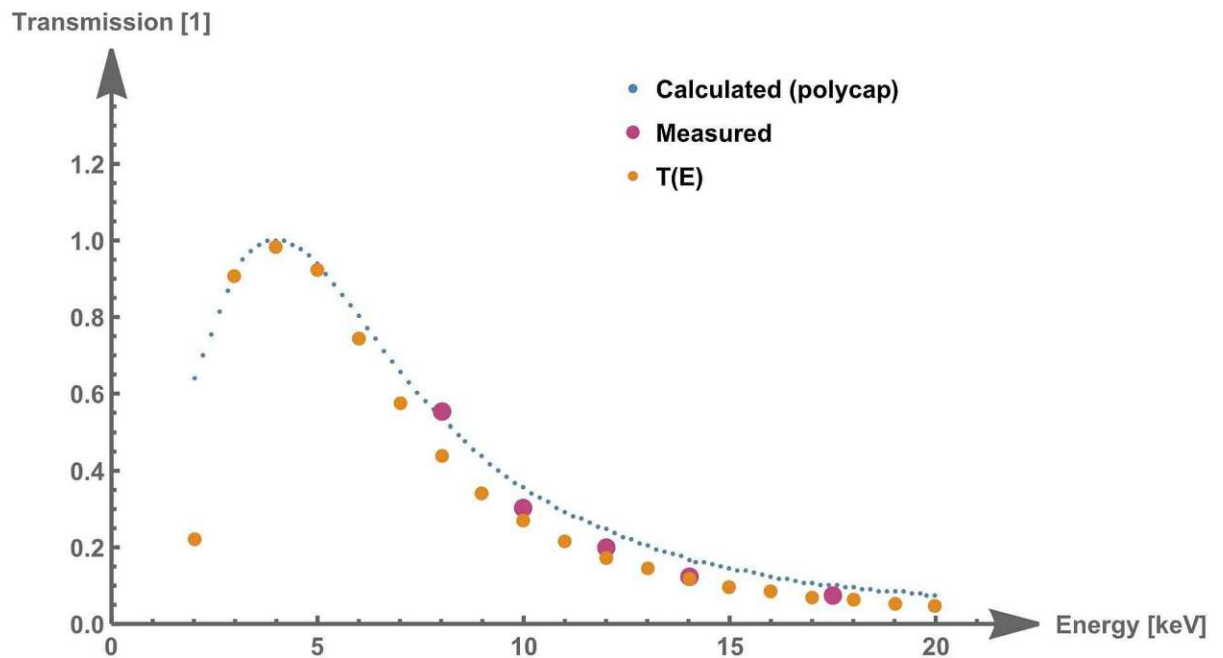


Figure 65: Model for the transmission function compared with single energy measurements made at the synchrotron and Monte Carlo simulations performed with polycap. The calculated and simulated values of the various energies are normalized to the maximum transmission at approximately 4 keV. The measured values are scaled accordingly to illustrate the trend of energy dependence. Previously published in [63]

This shows that *polycap* is well suited for the simulation of the used capillary optics as well as the developed analytical model, as both of them are in good agreement with measurement results for the polycapillary optics used in the experimental setup.

5.3 Investigation of standard reference materials with a three-dimensional structure

A current challenge for the full quantification of CMXRF measurements is the lack of generally applicable standard reference materials (SRM) of well known composition with a three-dimensional structure. First steps in the development of suitable SRMs with a three-dimensional structure were taken in collaboration with *S. Hampel and U. Fittschen* from TU Clausthal.

5.3.1 Filament based standard reference materials

The first samples were created with a filament-based 3D-printer at TU Clausthal. Figure 66 shows a printed sample cross structure made of filaments doped with steel (bottom) and brass (top) on a pure polymer support structure.



Figure 66: Printed sample cross structure made of filaments doped with steel (bottom) and brass (top) on a pure polymer support structure. The quadratic printed structure is approximately 1 *cm* wide with a layer thickness of 60 μm .

The cross-structures were printed with a filament-based 3D-printer. The weight percentages of the doping materials in the different filaments available from commercial filament distributors are shown in table 8.

Filament	Cu [w-%]	Sn [w-%]	Zn [w-%]	Fe [w-%]	Cr [w-%]	Polymer [w-%]
Bronze	72,8	7,2	/	/	/	20
Brass	48	/	32	/	/	20
Steel	/	/	/	68	12	20

Table 8: Composition of the filaments used in the printing process as given by the manufacturer, given as weight-percentages of the doping elements.

First depth scans in the lab seemed promising, showing an expected shape of the depth curve of the elements in the sample (see figure 67).

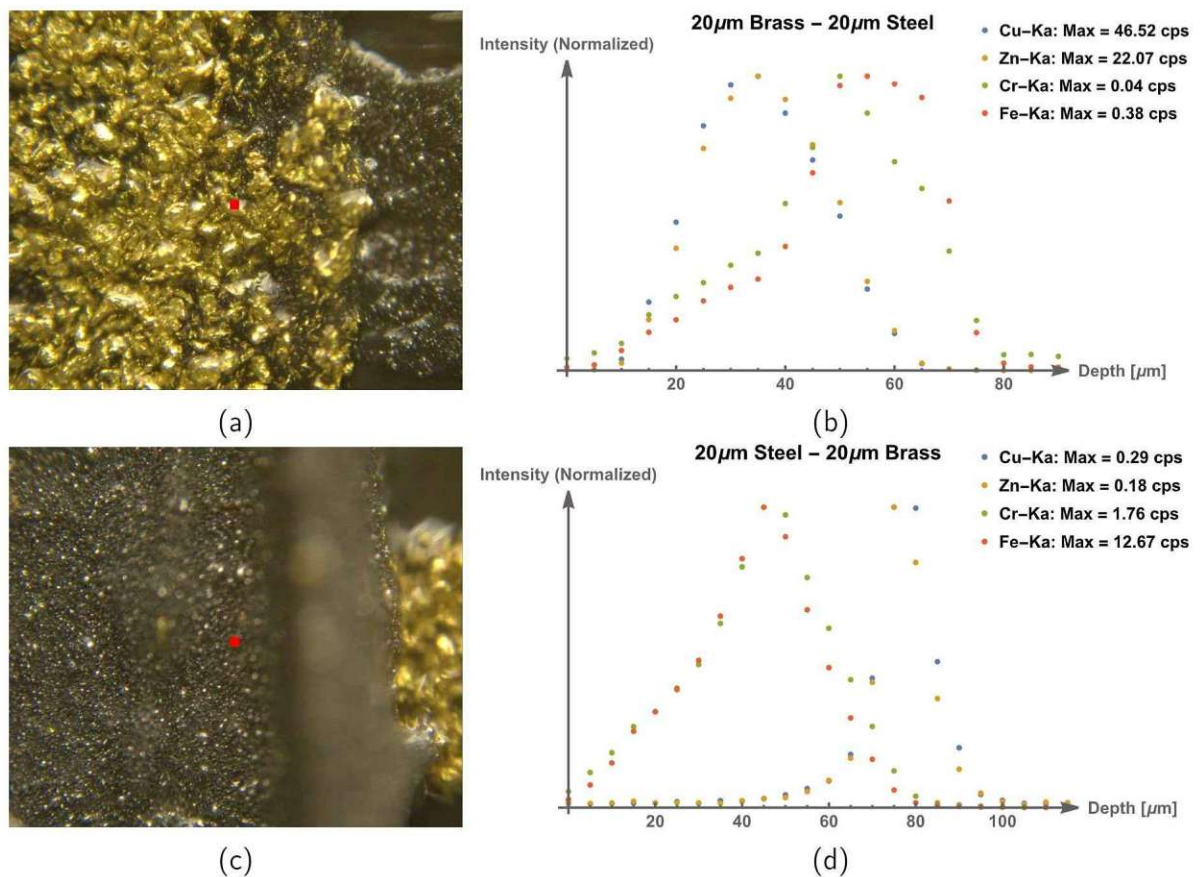


Figure 67: Images and depth curves of the K- α lines (normalized to the maximum value of each curve as given in the legend) of the elements Cu, Zn, Cr and Fe for cross structures made of brass and steel filaments with a composition as given in table 8. The images and curves are for (a) & (b) a 20 μm brass-filament-layer on top and a 20 μm steel-filament-layer on the bottom and for (c) & (d) a 20 μm steel-filament-layer on top and a 20 μm brass-filament-layer on the bottom.

The samples were further investigated in a beamtime at the XRF beamline at the Elettra Sincrotrone in Triest. The adapted setup presented in section 5.1 was installed at the XRF beamline (see figure 68) for the investigation of the 3D-printed samples.

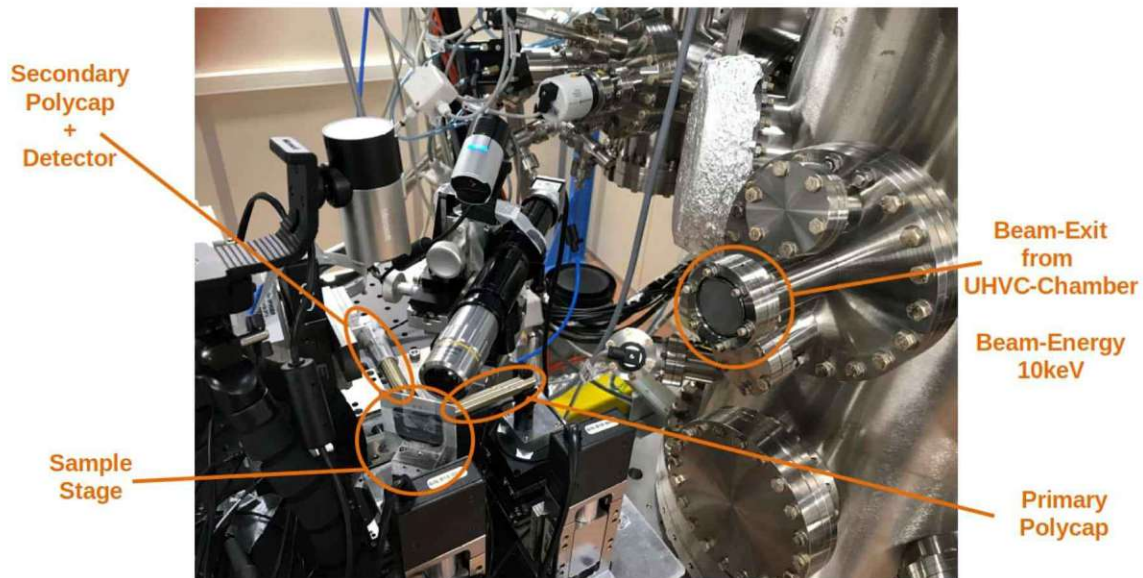


Figure 68: CMXRF setup at the XRF beamline at the Elettra Sincrotrone for the investigation of samples printed with a filament-based 3D-printer.

Figure 69 shows a photograph of the investigated sample (right, also shown in figure 66) and a microscope image of the investigated area (left) for which area scans were conducted in different depths.

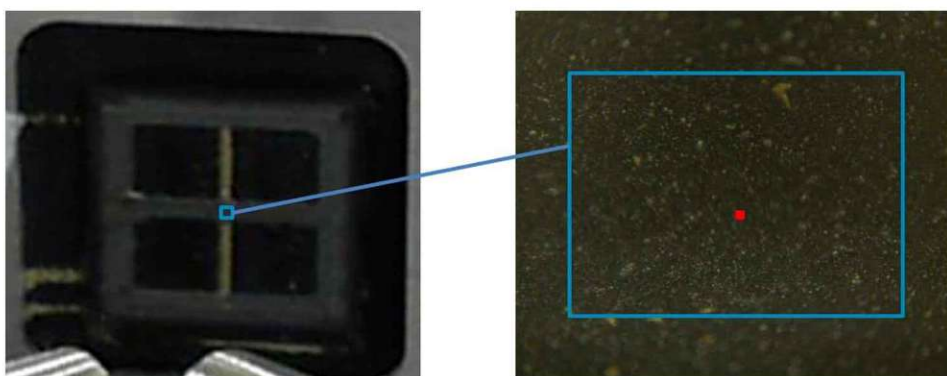


Figure 69: Investigated cross structure with 60 μm steel doped filament on top and 60 μm brass doped filament on the bottom in the setup at the synchrotron (left) and microscope image of the investigated area for which 3D scans were conducted (right).

For the use as SRM reproducibility of scan results is vital. The depth scans in the lab showed a high sensitivity in respect to the chosen surface point at which the depth scans were conducted on the shape of the depth curve. Therefore the investigation at the synchrotron focused on 3D-scans of a broader area of the printed samples. The resolution of the setup using a 10 keV primary energy was established with the scan of a Cu-Cross (see 32) to be $37 \mu\text{m}$ (horizontal) \times $27 \mu\text{m}$ (vertical) for Cu-K α . Due to the high-percentage of metal in the sample, different primary intensities were used for the area scans in different depths, to avoid count rates exceeding the detector capabilities (with high dead times) for upper layers and long measurement times necessary to receive a statistically relevant signal for layer deeper within the sample. The different primary intensities were achieved via reduction of the beam size in front of the primary polycapillary optic using slits. Figure 70 shows Fe maps of the area scans in different depths. It can be seen that the printed samples do not have a straight surface making them unsuitable for SRMs due to the variation in respect to the predefined structure.

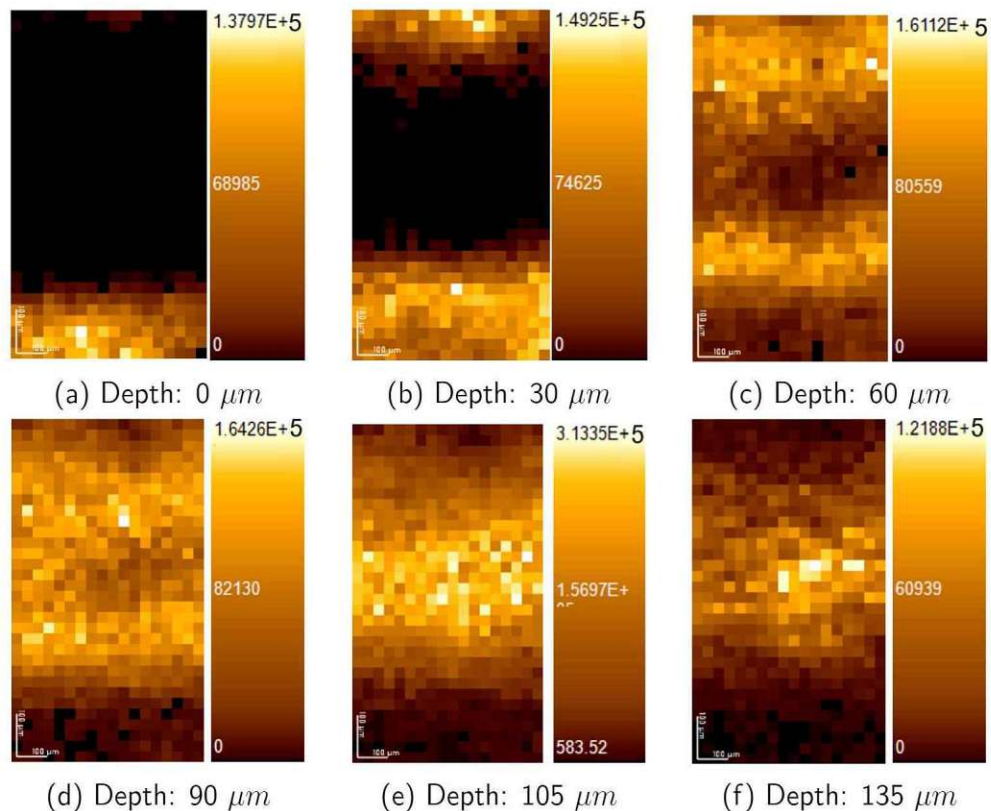


Figure 70: Heat maps of the investigated area in different depths for Fe-K α with a scale of total counts in with a stepsize of $25 \mu\text{m} \times 15 \mu\text{m}$

The scans show large variations of the Fe concentration in each layer, due to the roughness of the sample. To investigate the properties of the samples with a flat surface further measurements of the printed samples with a surface grinded with a very fine grain paper were conducted. These scans also showed large inhomogenities in the measured maps. This can be explained by a large particle size of the doping metal particles in the filament. Particle size was estimated to be up to roughly a third of the estimated confocal probing volume for Cu-Ka, making the filled part of the confocal volume random for different supposedly homogeneous parts of the sample. Figure 71 shows a foto of the grinded sample and microscope images of the investigated surface area. Figure 72 shows the inhomogenities in the Fe and Cu maps at the surface of a grinded sample.

The large inhomogenities in the printed samples visible in the maps taken at the synchrotron showed that the used 3D-printing technique is not applicable for the development of suitable SRMs, due to the grain size of the doping material and the surface roughness of the produced samples.

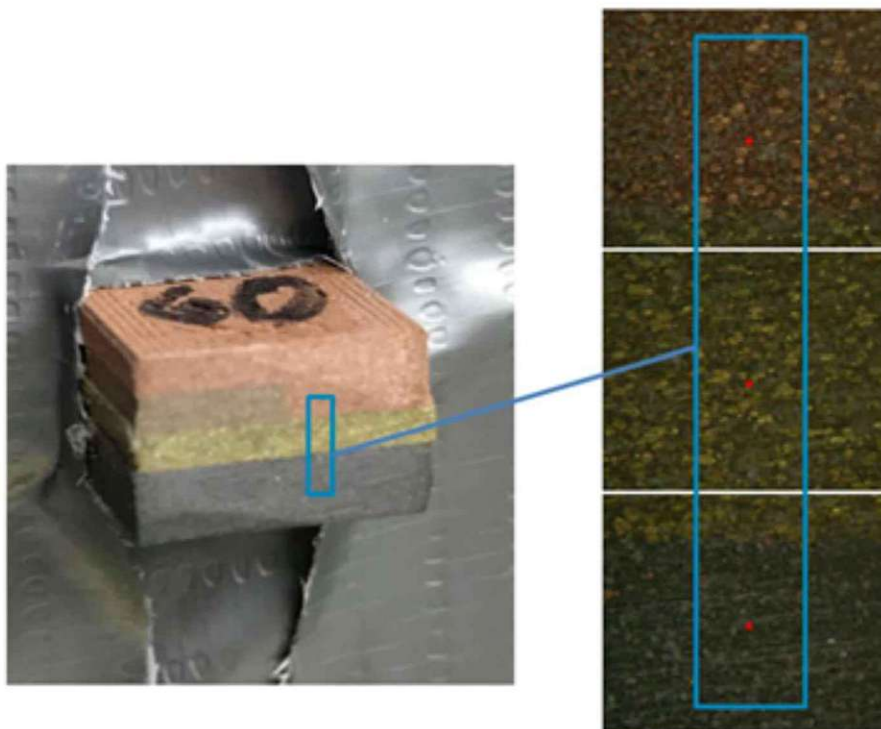


Figure 71: Foto of the investigated grinded sample (left) and microscope pictures of the surface of the investigated area (right).

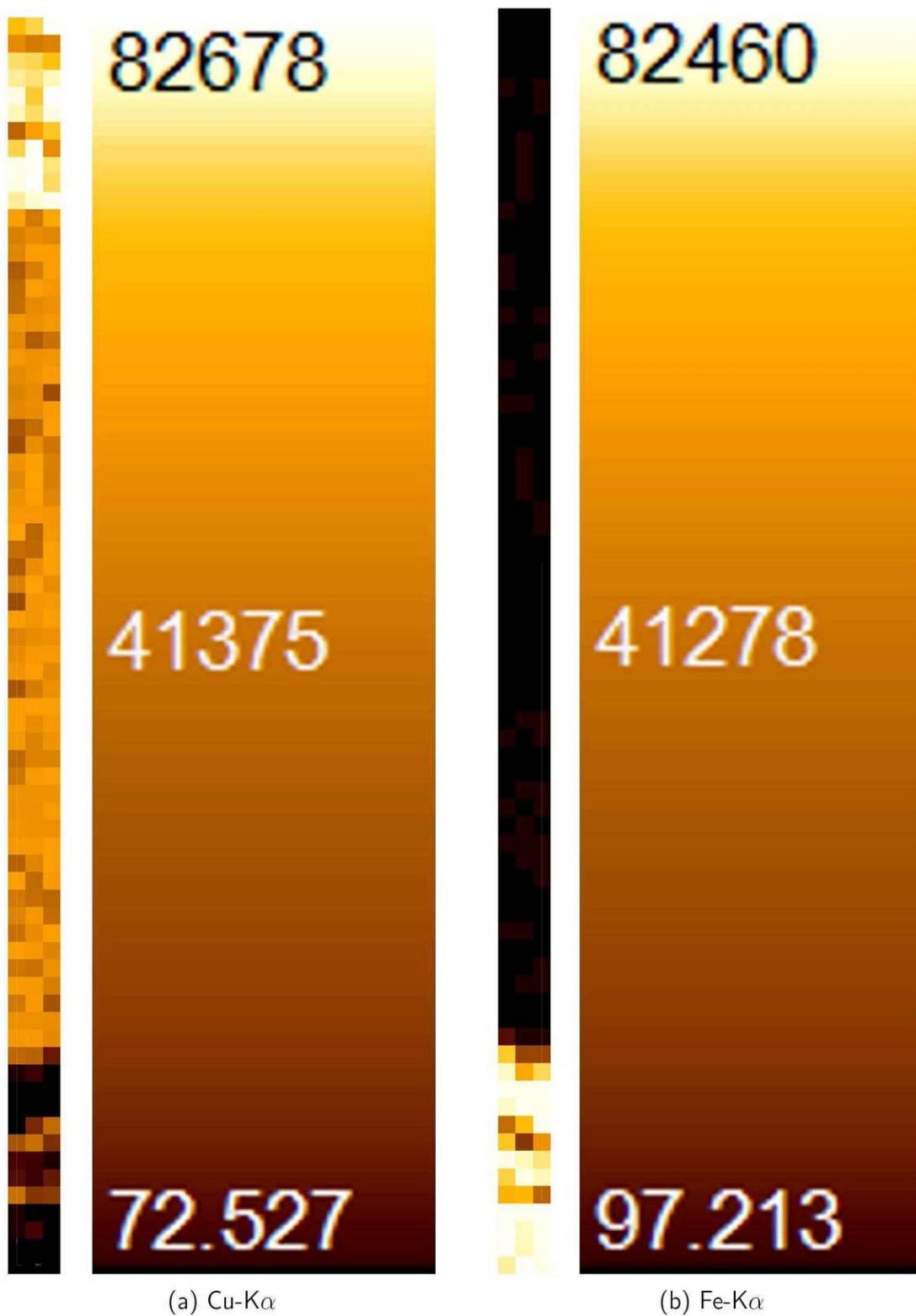


Figure 72: Heat maps for Cu-K α and Fe-K α at the surface of the grinded sample.

5.3.2 Resin based standard reference materials

An adapted printing process using a resin-based 3D-printer was used to create samples with a better defined structure. The samples printed at TU Clausthal, were investigated in a beamtime at the B16 Test Beamline at the Diamond Light Source. Figure 73 shows the setup, described in 5.1 at the beamline.

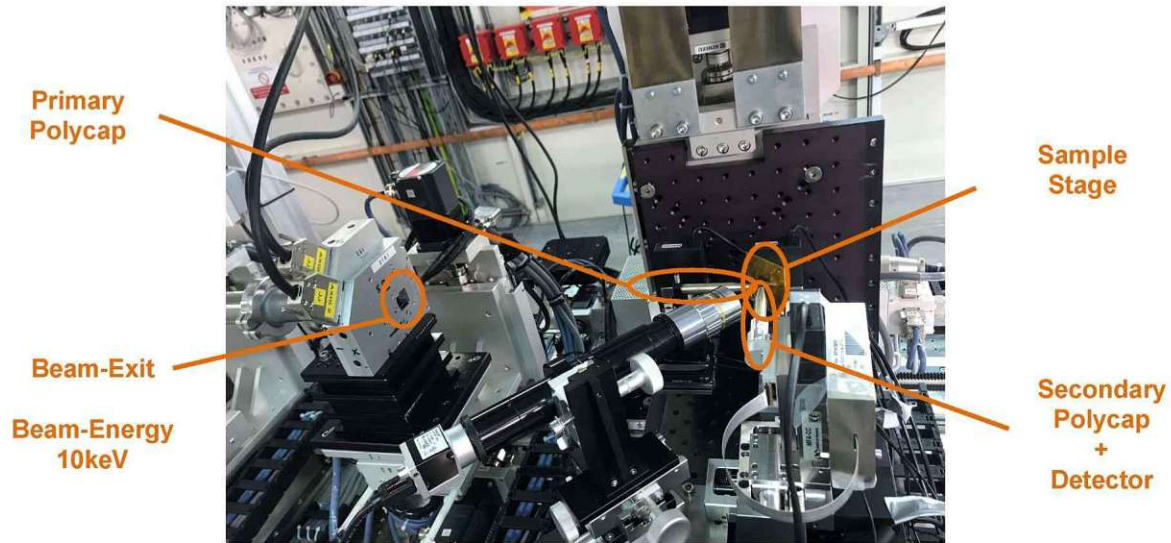


Figure 73: CMXRF setup at the B16 Test Beamline at the Diamond Light Source for the investigation of samples printed with a resin-based 3D-printer.

Due to the different printing process based on the hardening of resin, when exposed to UV-Light much lower doping element concentrations could be achieved (see table 9).

Sample	Fe [w-%]	Cr [w-%]	Co [w-%]	Zn [w-%]	Type
V6	0.039	0.036	/	/	Cr-cross on Fe
V10	0.039	0.036	/	/	Fe-cross on Cr
V11	/	0.035	0.046	/	Cr-cross on Co
V12	/	0.035	0.046	/	Co-cross on Cr
V13	0.036	/		0.062	Fe-cross on Zn
V14	0.036	/		0.062	Zn-cross on Fe
V15	/	0.035	0.046	0.062	Triple-cross Cr on Co on Zn

Table 9: Concentration of doping materials in the different samples for the doping elements used in the substrate and the printed cross structure. The resin of substrate and structure are doped with a single element.

Thin cross-structures (50 μm thickness) printed with resin doped with a single element were investigated (see figure 74). The structures are printed on a substrate of resin doped with a different element.

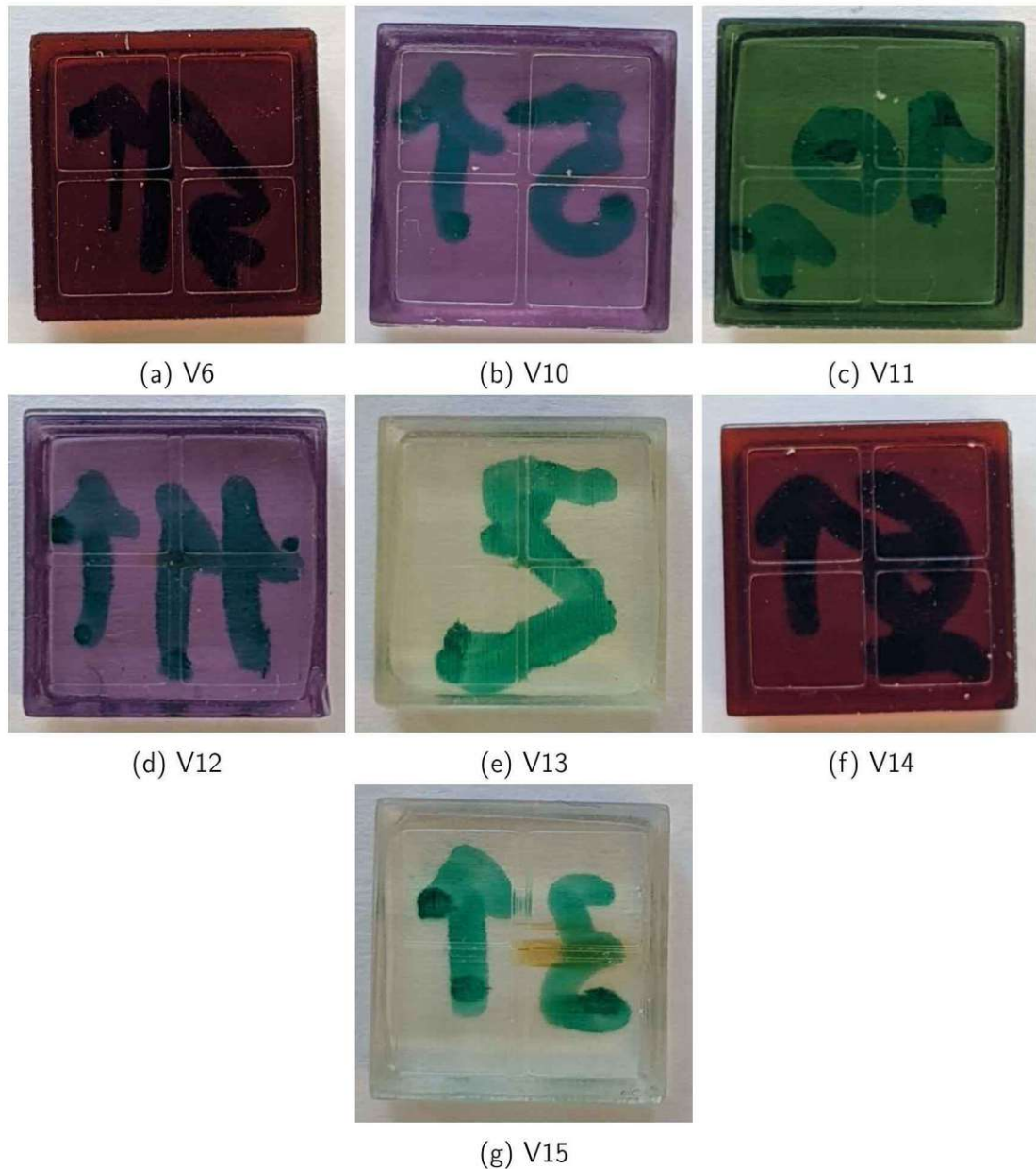


Figure 74: Samples printed with a resin based 3D-printer. The samples are crosses printed with resin doped with an element on a substrate of resin doped with a different element. The samples are (a) Cr-cross on Fe, (b) Fe-cross on Cr, (c) Cr-cross on Co, (d) Co-cross on Cr, (e) Fe-cross on Zn, (f) Zn-cross on Fe, (g) Triple-cross Cr on Co on Zn. Concentrations of the doping material are listed in table 9.

The investigated samples showed good homogeneity of the doping materials. Figures 75-80 show microscope images and heat maps of the $K\alpha$ signal of the doping element of the printed structure at the surface. All samples show good homogeneity of the doping material.

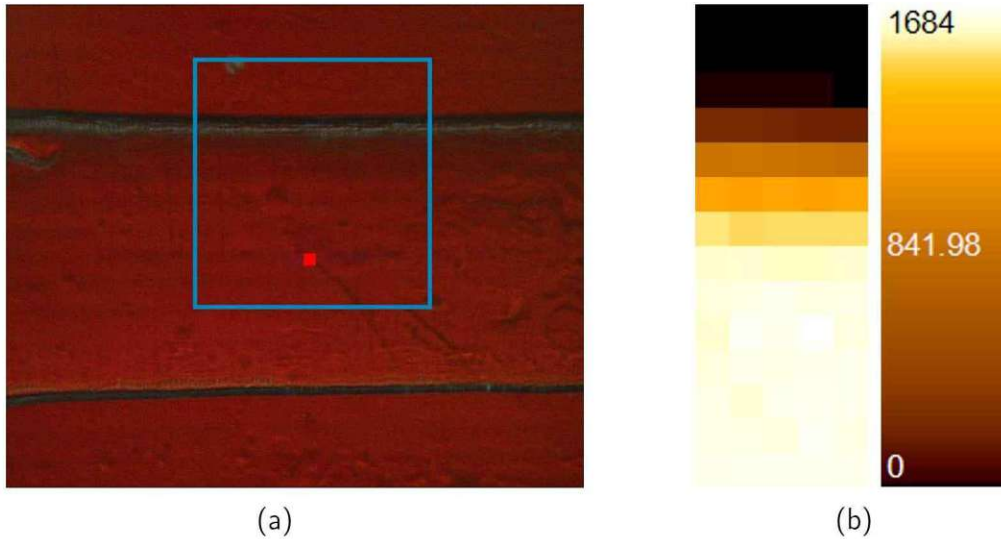


Figure 75: Sample V6 - Cr-cross on Fe: Microscope image of the investigated area (a) and heat map of the ROI of Cr- $K\alpha$ for the area scans in cps at the surface (b).

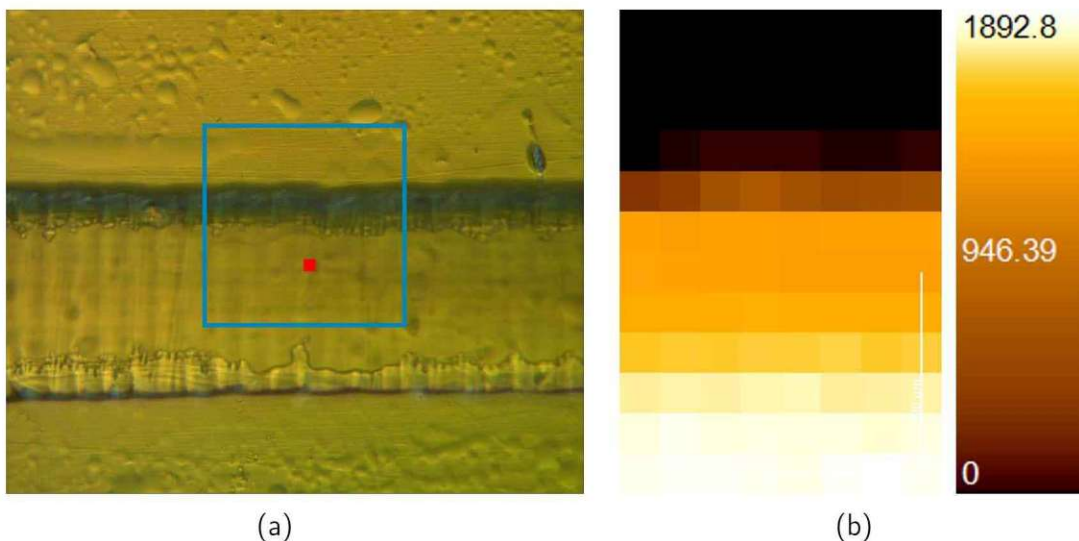


Figure 76: Sample V10 - Fe-cross on Cr: Microscope image of the investigated area (a) and heat map of the ROI of Fe- $K\alpha$ for the area scans in cps at the surface (b).

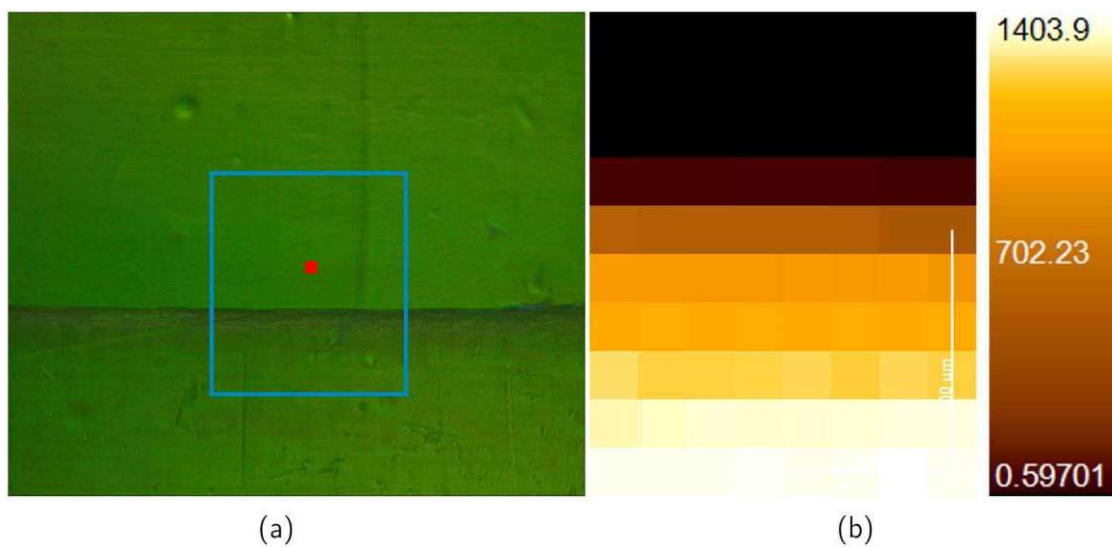


Figure 77: Sample V11 - Cr-cross on Co: Microscope image of the investigated area (a) and heat map of the ROI of Cr- $K\alpha$ for the area scans in cps at the surface (b).

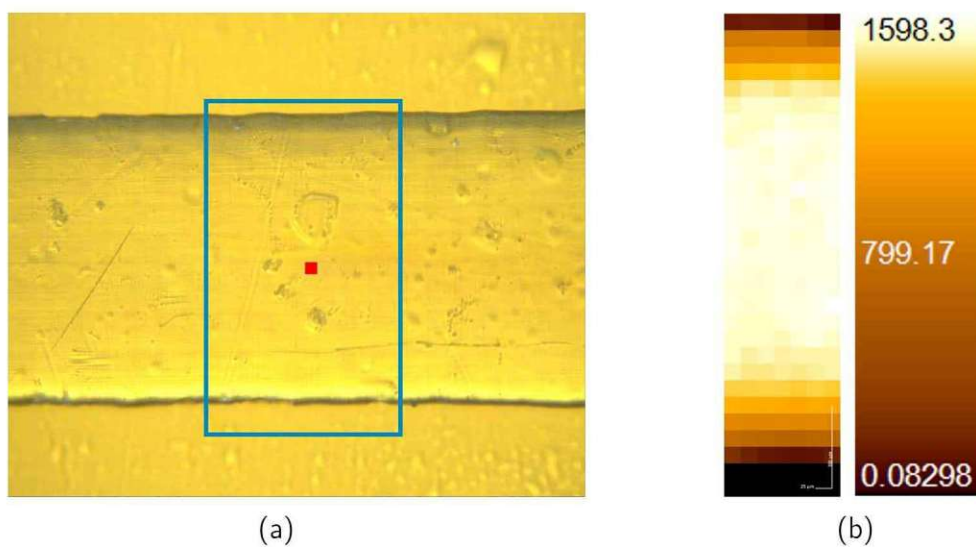


Figure 78: Sample V12 - Co-cross on Cr: Microscope image of the investigated area (a) and heat map of the ROI of Co- $K\alpha$ for the area scans in cps at the surface (b).

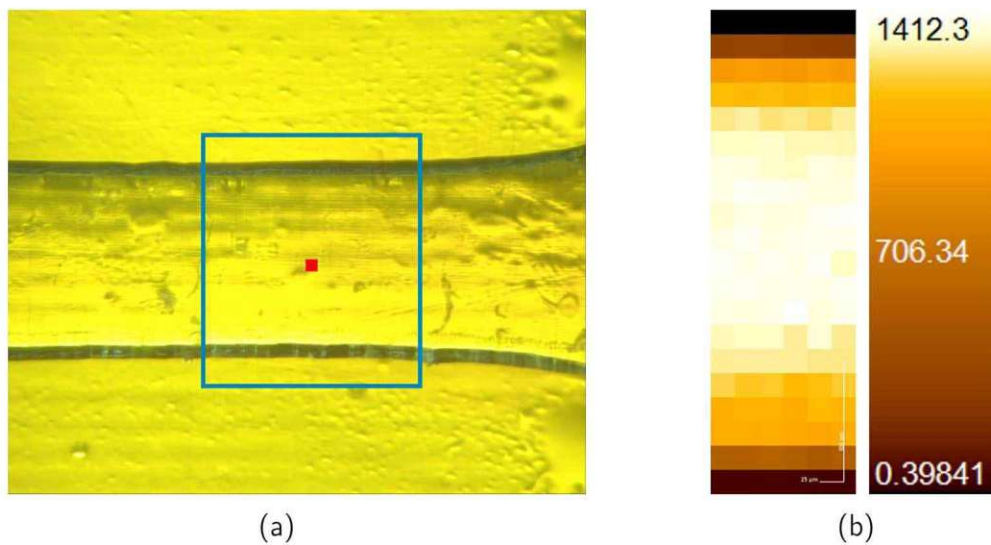


Figure 79: Sample V13 - Fe-cross on Zn: Microscope image of the investigated area (a) and heat map of the ROI of Fe- $K\alpha$ for the area scans in cps at the surface (b).

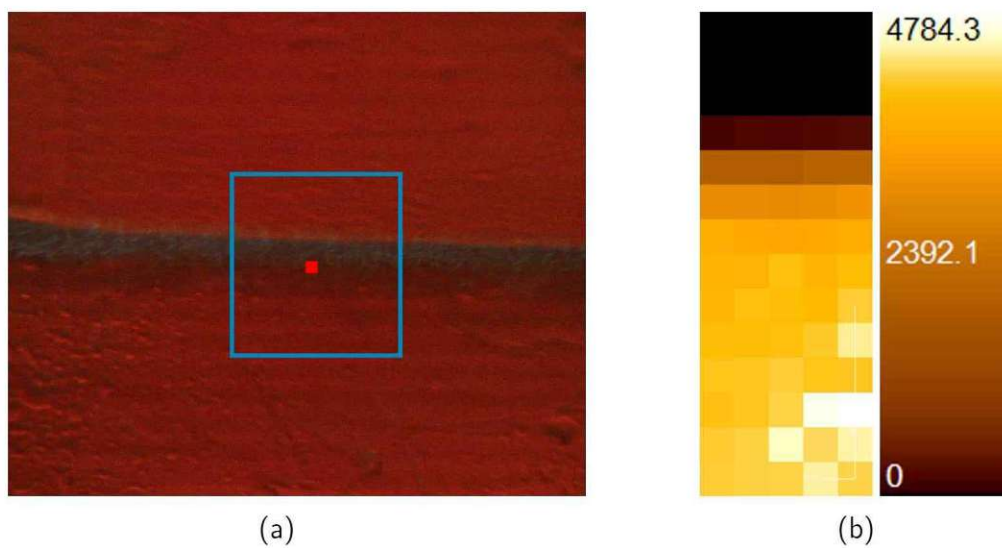


Figure 80: Sample V14 - Zn-cross on Fe: Microscope image of the investigated area (a) and heat map of the ROI of Zn- $K\alpha$ for the area scans in cps at the surface (b).

Figures 81-83 show the heat maps for the lines Cr- $K\alpha$, Co- $K\alpha$ and Zn- $K\alpha$ in the depths $0\ \mu\text{m}$, $45\ \mu\text{m}$ and $120\ \mu\text{m}$ of the triple-cross structure (see V15 in table 9) shown as a microscope image in figure 84.

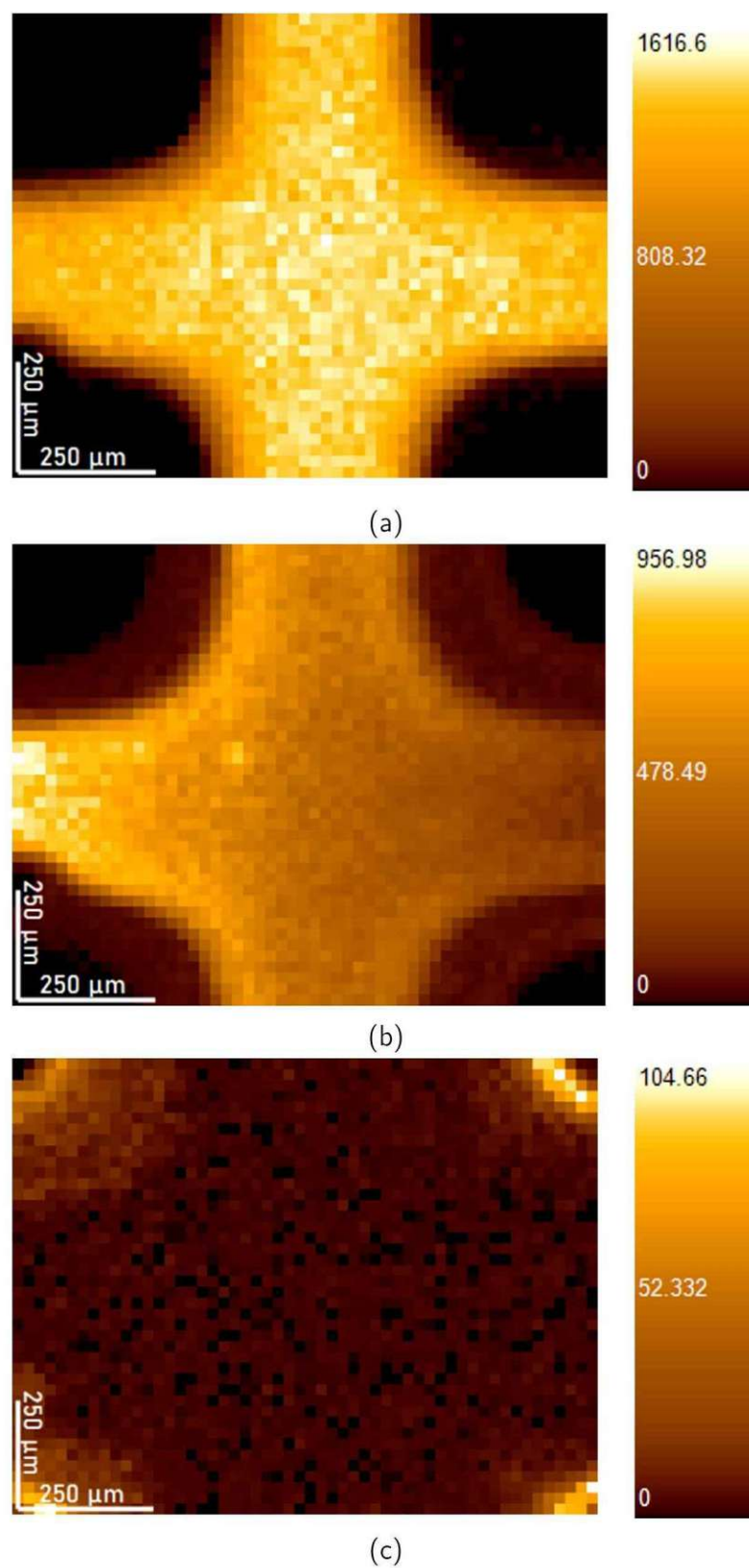


Figure 81: Heat map of the ROI of Cr-K α for the area scans in cps in the depths 0 μm (a), 45 μm (b) and 120 μm (c). The Cr distribution is visibly to homogeneous and performs best in the uppermost layer.

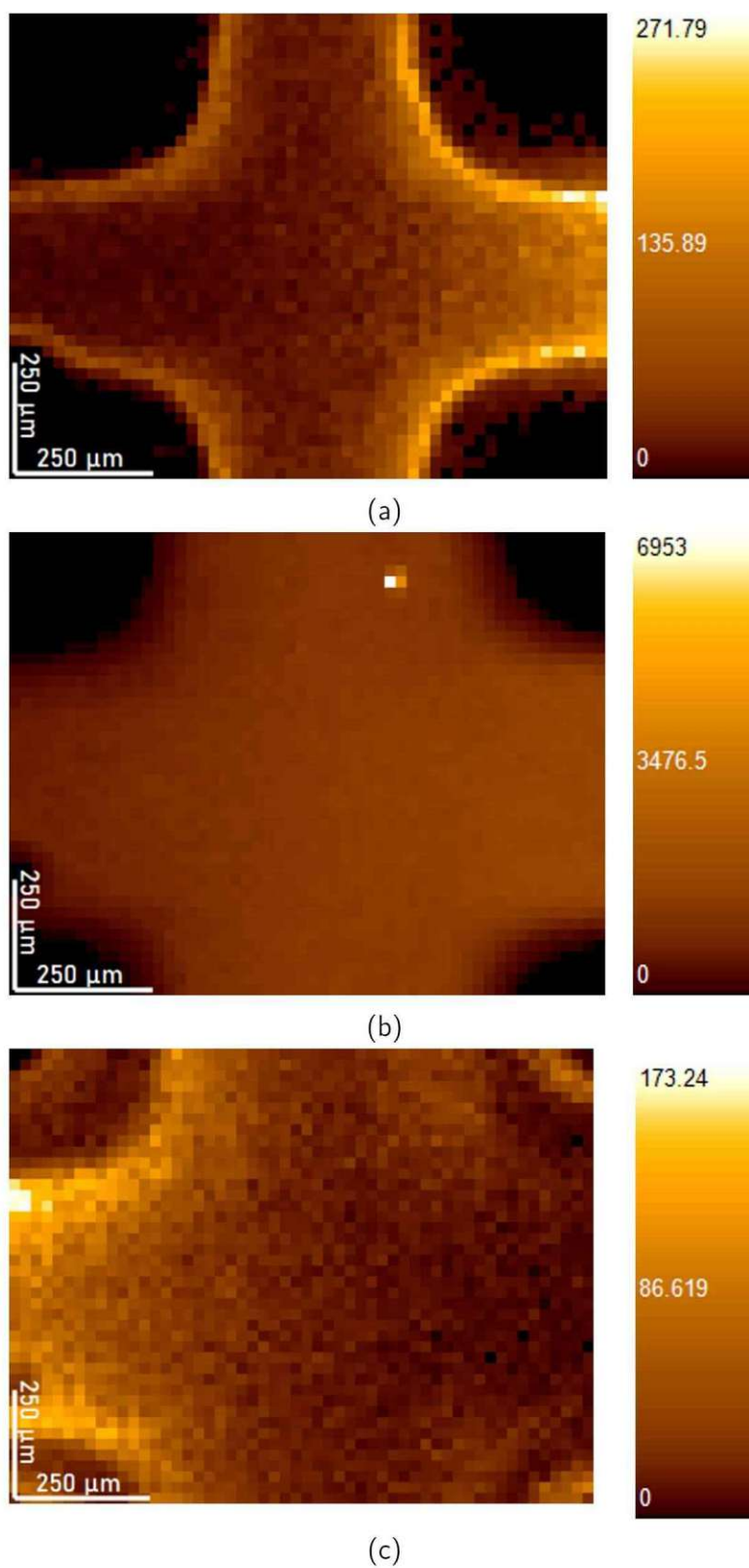


Figure 82: Heat map of the ROI of Co-K α for the area scans in cps in the depths 0 μm (a), 45 μm (b) and 120 μm (c). The Co distribution is visibly to homogeneous and performs best in the middle layer.

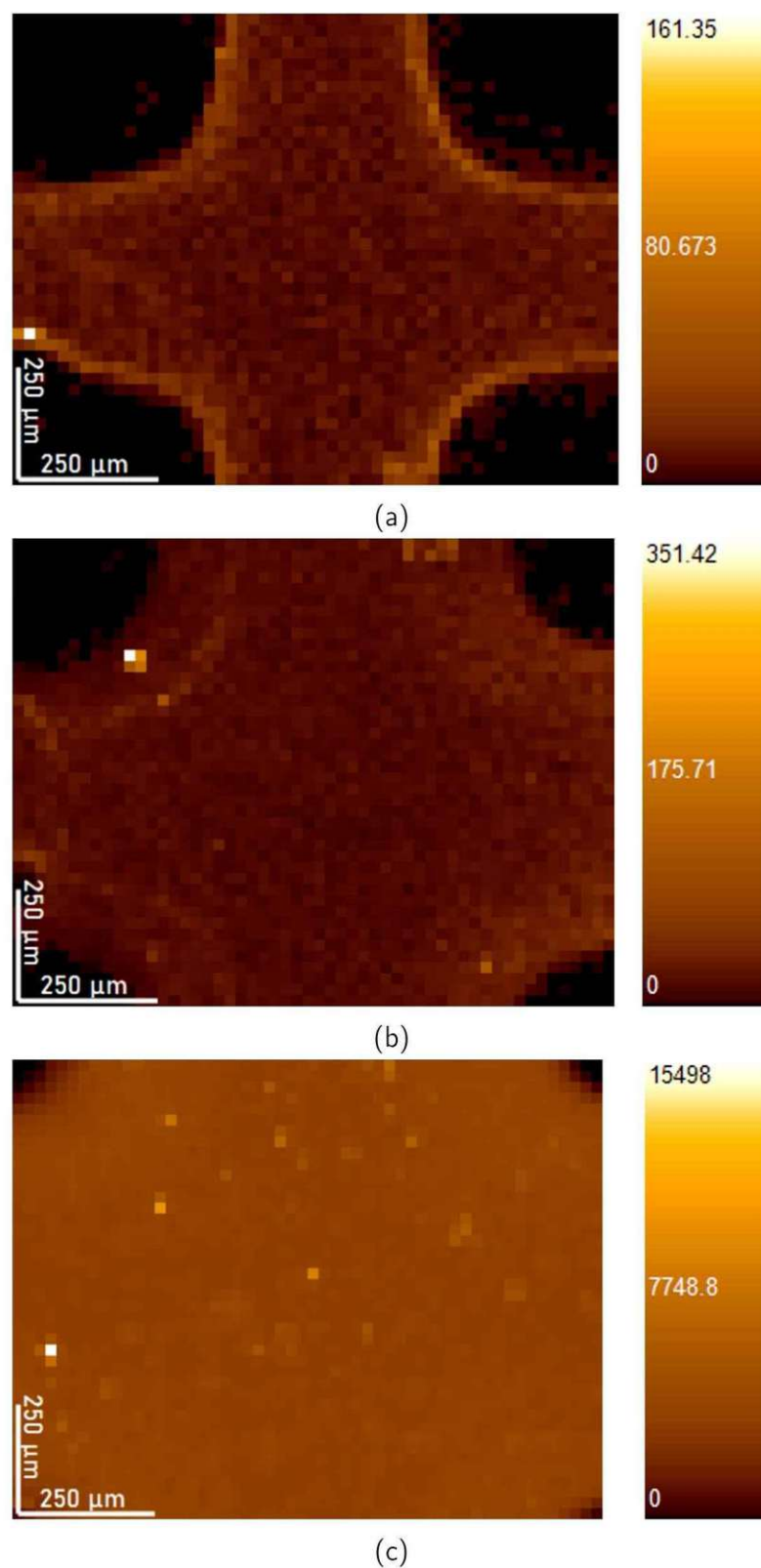


Figure 83: Heat map of the ROI of Zn-K α for the area scans in cps in the depths 0 μm (a), 45 μm (b) and 120 μm (c). The Zn distribution is visibly to homogeneous and performs best in the lowest layer.

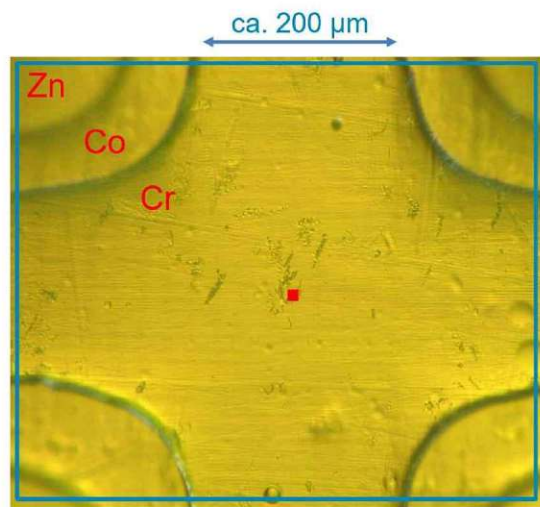


Figure 84: Microscope image of the investigated triple-cross structure, with a Cr-doped resin cross on a Co-doped resin cross on a Zn-doped resin cross (see V15 in table 9). Previously published in [61]

5.3.3 Simulation of the measured results with voxTrace

A depth scan of the triple cross structure was simulated with a layer thickness of 50 μm with concentration of the doping materials as given in table 9. The dark-matrix of the resin was modelled as pure carbon.

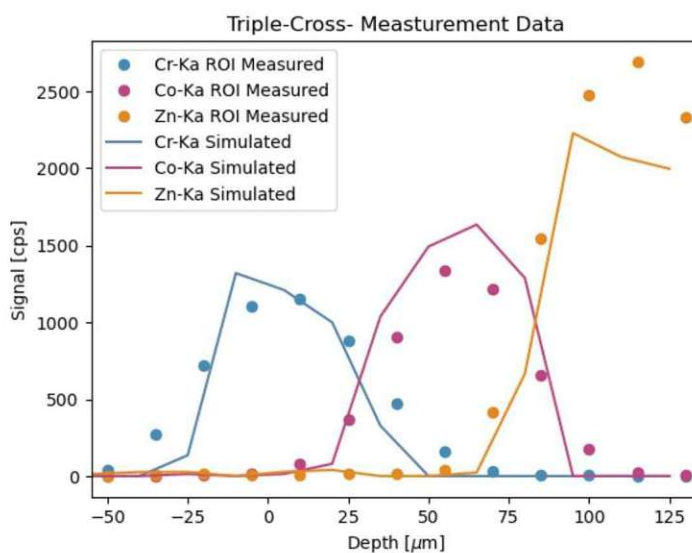


Figure 85: Plot of the $K\alpha$ -lines of the elements Cr, Co and Zn as a function of depth. Previously published in [61]

The simulation was performed on the Vienna Scientific Cluster. Simulation results are in good agreement with the measurements, with the ratios of the simulated maxima of the signals being similar to the measurements.

6 Conclusion and Outlook

During the work for this thesis a new fundamental voxel-based Monte-Carlo ray tracing software for the simulation of confocal Micro X-Ray fluorescence (CMXRF) measurements was developed. The software was implemented utilizing the parallelization power of graphic processing units (GPUs). This allows a fast simulation of complicated samples on high-performance-clusters and simple homogeneous or layered samples with a regular workstation with a suitable GPU. Benchmarks for the simulation were conducted on a single node of the Vienna Scientific Cluster 5 with 2 NVIDIA A40 GPUs and a dual socket with 8 cores AMD EPYC 7252 per node and a regular workstation PC with an AMD Ryzen 7 5800X, 8C/16T, 3.80-4.70 GHz CPU and a ZOTAC Gaming GeForce RTX 3060 Ti Twin Edge OC LHR, 8GB GPU proving a reasonable timeframe for the simulation.

Validity of the software was shown via the comparison of simulations with measurements of 3D-printed standard reference materials of well known composition with a three-dimensional structure. The measurements were conducted at the XRF beamline at the Elletra Sincrotrone Triest and B16 Test Beamline at the Diamond Light Source. Measurements and simulation supported the development of the printing process to establish SRMs with suitable properties. Further development of possible SRMs printed with a resin based 3D printer can be supported by the simulation of different (very low) element concentrations and their effect on the measurement results.

To support the development of the software the parameters of polycapillary half-lenses, vital for the exact simulation of the process were investigated in the lab and at the synchrotron. The investigations at Atominstut and at the BAMline beamline at the BESSY II Synchrotron of the Helmholtz-Zentrum-Berlin showed a good agreement between measurements, a new analytical model for the transmission as well as results simulated with the software *polycap* [1], used for the simulation of capillary half-lenses in *voxTrace*. Furthermore it was shown that a multivariate normal distribution is a good approximation for the beam transmitted by a polycapillary optic in focussing direction.

An object-oriented approach was chosen for the implementation to ensure readability and adaptability of the code, while keeping performance in mind. Future developments will include the implementation of global optimization algorithms, from common libraries such as *ensmallen* [72] to perform an optimization of the elemental composition of the voxels in the

sample model regarding to a fit of the simulated spectra with measured ones. For this an advanced modelling of the detector response function could prove beneficial for the comparability of the measured spectra with simulated ones.

The fundamental ray tracing approach should minimize the need for SRMs with similar properties as the measured sample and the effort for setup calibration. As shown in section 4.3, the software can also be used for the investigation of the setup itself, investigating possible outcomes of small misalignments.

Further future development could include flags for different processes. This makes a deconvolution of the spectrum in a previously impossible way feasible. The simulated spectra can be deconvoluted into radiation from second order excitation, multiple scattering etc. possible.

References

- [1] P. Tack et al. "An X-ray ray tracing simulation code for mono- and polycapillaries: Description, advances and application". In: *Spectrochimica Acta - Part B Atomic Spectroscopy* 173 (July 2020). Publisher: Elsevier, p. 105974. ISSN: 05848547. DOI: 10.1016/j.sab.2020.105974. URL: <https://doi.org/10.1016/j.sab.2020.105974>.
- [2] M. A. Kumakhov. "Channeling of photons and new X-ray optics". In: *Nuclear Inst. and Methods in Physics Research, B* 48.1 (1990), pp. 283–286. ISSN: 0168583X. DOI: 10.1016/0168-583X(90)90123-C.
- [3] M. A. Kumakhov. "Capillary optics and their use in x-ray analysis". In: *X-Ray Spectrometry* 29.5 (2000), pp. 343–348. ISSN: 00498246. DOI: 10.1002/1097-4539(200009/10)29:5<343::AID-XRS414>3.0.CO;2-S.
- [4] N. L. Cordes et al. "Three dimensional subsurface elemental identification of minerals using confocal micro-X-ray fluorescence and micro-X-ray computed tomography". In: *Spectrochimica Acta Part B: Atomic Spectroscopy* 103-104 (Jan. 1, 2015), pp. 144–154. ISSN: 0584-8547. DOI: 10.1016/j.sab.2014.12.006. URL: <https://www.sciencedirect.com/science/article/pii/S0584854714003255> (visited on 09/03/2023).
- [5] B. Bazi et al. "Trace-element analysis of mineral grains in Ryugu rock fragment sections by synchrotron-based confocal X-ray fluorescence". In: *Earth, Planets and Space* 74 (Nov. 1, 2022), p. 161. DOI: 10.1186/s40623-022-01726-y.
- [6] A. Roschger et al. "Differential accumulation of lead and zinc in double-tidemarks of articular cartilage". In: *Osteoarthritis and Cartilage* 21.11 (Nov. 1, 2013). Publisher: Elsevier, pp. 1707–1715. ISSN: 1063-4584, 1522-9653. DOI: 10.1016/j.joca.2013.06.029. URL: [https://www.oarsijournal.com/article/S1063-4584\(13\)00865-0/fulltext](https://www.oarsijournal.com/article/S1063-4584(13)00865-0/fulltext) (visited on 09/03/2023).
- [7] S. Hirano et al. "Elemental depth imaging of solutions for monitoring corrosion process of steel sheet by confocal micro X-ray fluorescence". In: *X-Ray Spectrometry* 43.4 (2014), pp. 216–220. ISSN: 00498246. DOI: 10.1002/xrs.2542. URL: <http://doi.wiley.com/10.1002/xrs.2542> (visited on 09/07/2015).

- [8] T. Lachmann et al. "Combined 1D, 2D and 3D micro-XRF techniques for the analysis of illuminated manuscripts". In: *Journal of Analytical Atomic Spectrometry* 31.10 (2016). Publisher: Royal Society of Chemistry, pp. 1989–1997. ISSN: 13645544. DOI: 10.1039/c6ja00220j. URL: <http://dx.doi.org/10.1039/C6JA00220J>.
- [9] M. Eveno et al. "Confocal XRF depth profiling nondestructively reveals the original blue pigments in a Renaissance painting by Caroto". In: *Studies in Conservation* 61.2 (2016), pp. 102–112. ISSN: 20470584. DOI: 10.1080/00393630.2016.1142059.
- [10] K. Tsuji et al. "Secondary excitation process for quantitative confocal 3D-XRF analysis". In: *Powder Diffraction* 30.2 (2015), pp. 109–112. ISSN: 0885-7156. DOI: 10.1017/S0885715615000251. URL: http://www.journals.cambridge.org/abstract_S0885715615000251.
- [11] G. J. Chen et al. "Ray-tracing of X-ray focusing capillaries". In: *Nuclear Inst. and Methods in Physics Research, A* 347.1 (1994), pp. 407–411. ISSN: 01689002. DOI: 10.1016/0168-9002(94)91918-6.
- [12] D. Hampai et al. "X-ray propagation through polycapillary optics studied through a ray tracing approach". In: *Spectrochimica Acta Part B: Atomic Spectroscopy* 62.6 (2007), pp. 608–614. ISSN: 05848547. DOI: 10.1016/j.sab.2007.03.002. URL: <http://linkinghub.elsevier.com/retrieve/pii/S0584854707000560>.
- [13] R. Jenkins et al. "Nomenclature, symbols, units and their usage in spectrochemical analysis - VIII. Nomenclature system for X-ray spectroscopy (Recommendations 1991)". In: *Pure and Applied Chemistry* 63.5 (1991). Publisher: International Union of Pure and Applied Chemistry, pp. 735–746. ISSN: 0033-4545, 1365-3075. DOI: 10.1351/pac199163050735. URL: <https://publications.iupac.org/pac/63/5/0735/index.html> (visited on 07/11/2023).
- [14] O. Hemberg, M. Otendal, and H. M. Hertz. "Liquid-metal-jet anode electron-impact x-ray source". In: *Applied Physics Letters* 83.7 (Aug. 12, 2003), pp. 1483–1485. ISSN: 0003-6951. DOI: 10.1063/1.1602157. URL: <https://doi.org/10.1063/1.1602157> (visited on 05/31/2023).
- [15] U. Pietsch, V. Holý, and T. Baumbach. *High-Resolution X-Ray Scattering*. Advanced Texts in Physics. New York, NY: Springer, 2004. DOI: 10.1007/978-1-4757-4050-9. URL: <http://link.springer.com/10.1007/978-1-4757-4050-9> (visited on 07/10/2023).

- [16] C. Streli, P. Wobrauschek, and P. Kregsamer. "X-Ray Fluorescence Spectroscopy, Applications". In: *Encyclopedia of Spectroscopy and Spectrometry (Third Edition)*. Ed. by J. C. Lindon, G. E. Tranter, and D. W. Koppenaal. Oxford: Academic Press, Jan. 1, 2017, pp. 707–715. ISBN: 978-0-12-803224-4. DOI: 10.1016/B978-0-12-803224-4.00315-0. URL: <https://www.sciencedirect.com/science/article/pii/B9780128032244003150> (visited on 07/10/2023).
- [17] R. Klockenkämper and A. v. Bohlen. *Total-reflection X-ray fluorescence analysis and related methods*. 2nd ed. Publication Title: Hoboken: John Wiley & Sons, 2015. ISBN: 978-1-118-46027-6.
- [18] R. E. Van Grieken and A. A. Markowicz. *Handbook of X-Ray Spectrometry*. 2001. ISBN: 0-8247-0383-9.
- [19] A. Brunetti et al. "A library for X-ray-matter interaction cross sections for X-ray fluorescence applications". In: *Spectrochimica Acta - Part B Atomic Spectroscopy* 59.10 (2004). ISBN: 0584-8547, pp. 1725–1731. ISSN: 05848547. DOI: 10.1016/j.sab.2004.03.014.
- [20] T. Schoonjans et al. "The xraylib library for X-ray-matter interactions. Recent developments". In: *Spectrochimica Acta - Part B Atomic Spectroscopy* 66.11 (2011). Publisher: Elsevier B.V., pp. 776–784. ISSN: 05848547. DOI: 10.1016/j.sab.2011.09.011. URL: <http://dx.doi.org/10.1016/j.sab.2011.09.011>.
- [21] J. H. Hubbell et al. "Atomic form factors, incoherent scattering functions, and photon scattering cross sections". In: *Journal of Physical and Chemical Reference Data* 4 (July 1, 1975). ADS Bibcode: 1975JPCRD...4..471H, pp. 471–538. ISSN: 0047-2689. DOI: 10.1063/1.555523. URL: <https://ui.adsabs.harvard.edu/abs/1975JPCRD...4..471H> (visited on 08/27/2023).
- [22] D. Cullen, J. Hubbel, and L. Kissel. *EPDL97: the evaluated photon library*. Lawrence Livermore National Laboratory Report Technical Report UCRL-50400 Vol.6 Rev.5. 1997. URL: <https://www.osti.gov/servlets/purl/295438> (visited on 08/27/2023).
- [23] M. Haschke. *Micro-X-Ray Fluorescence Spectroscopy - Instrumentation and Applications*. Publication Title: Springer-Verlag Berlin Heidelberg GmbH ISSN: 09315195. 2014. 367 pp. ISBN: 978-3-319-04863-5. DOI: 10.1007/978-3-319-04864-2.

- [24] B. Kanngießner, W. Malzer, and I. Reiche. "A new 3D micro X-ray fluorescence analysis set-up – First archaeometric applications". In: *Nuclear Instruments and Methods in Physics Research Section B: Beam Interactions with Materials and Atoms* 211.2 (Oct. 1, 2003), pp. 259–264. ISSN: 0168-583X. DOI: 10.1016/S0168-583X(03)01321-1. URL: <https://www.sciencedirect.com/science/article/pii/S0168583X03013211> (visited on 08/02/2023).
- [25] L. Vincze et al. "Three-dimensional trace element analysis by confocal X-ray microfluorescence imaging". In: *Analytical chemistry* 76.22 (2004). ISBN: 3238202359, pp. 6786–91. ISSN: 0003-2700. DOI: 10.1021/ac0492741. URL: <http://www.ncbi.nlm.nih.gov/pubmed/15538804>.
- [26] J. Sherman. "The theoretical derivation of fluorescent X-ray intensities from mixtures". In: *Spectrochimica Acta* 7 (Jan. 1, 1955), pp. 283–306. ISSN: 0371-1951. DOI: 10.1016/0371-1951(55)80041-0. URL: <https://www.sciencedirect.com/science/article/pii/0371195155800410> (visited on 08/03/2023).
- [27] Ž. Šmit et al. "Confocal μ -XRF depth analysis of paint layers". In: *Nuclear Instruments and Methods in Physics Research Section B: Beam Interactions with Materials and Atoms* 219-220 (2004), pp. 35–40. ISSN: 0168583X. DOI: 10.1016/j.nimb.2004.01.024.
- [28] B. Kanngießner et al. "Three-dimensional micro-XRF investigations of paint layers with a tabletop setup". In: *Spectrochimica Acta Part B: Atomic Spectroscopy* 60.1 (2005), pp. 41–47. ISSN: 05848547. DOI: 10.1016/j.sab.2004.10.012. URL: <http://linkinghub.elsevier.com/retrieve/pii/S0584854704003027> (visited on 10/03/2013).
- [29] K. Nakano and K. Tsuji. "Nondestructive elemental depth profiling of Japanese lacquerware 'Tamamushi-nuri' by confocal 3D-XRF analysis in comparison with micro GE-XRF". In: *X-Ray Spectrometry* 38.5 (2009), pp. 446–450. ISSN: 1097-4539. DOI: 10.1002/xrs.1163. URL: <https://onlinelibrary.wiley.com/doi/abs/10.1002/xrs.1163> (visited on 08/03/2023).
- [30] R. D. Perez et al. "Latest developments and opportunities for 3D analysis of biological samples by confocal μ -XRF". In: *Radiation Physics and Chemistry* 79.2 (2010), pp. 195–200. ISSN: 0969806X. DOI: 10.1016/j.radphyschem.2009.04.034.

- [31] Q. Xu et al. "Determination of Hepatic Iron Deposition in Drug-Induced Liver Fibrosis in Rats by Confocal Micro-XRF Spectrometry". In: *ACS Omega* 7.4 (Jan. 24, 2022), pp. 3738–3745. ISSN: 2470-1343. DOI: 10.1021/acsomega.1c06476. URL: <https://www.ncbi.nlm.nih.gov/pmc/articles/PMC8811927/> (visited on 08/02/2023).
- [32] S. J. Van Malderen et al. "Three-Dimensional Reconstruction of the Tissue-Specific Multielemental Distribution within *Ceriodaphnia dubia* via Multimodal Registration Using Laser Ablation ICP-Mass Spectrometry and X-ray Spectroscopic Techniques". In: *Analytical Chemistry* 89.7 (2017), pp. 4161–4168. ISSN: 15206882. DOI: 10.1021/acs.analchem.7b00111.
- [33] T. Trojek and M. Hložek. "Confocal XRF imaging for determination of arsenic distribution in a sample of historic plaster". In: *Radiation Physics and Chemistry*. The 15th International Symposium on Radiation Physics (ISRP15), 6 - 10 December, 2021, Sunway University, Malaysia 200 (Nov. 1, 2022), p. 110201. ISSN: 0969-806X. DOI: 10.1016/j.radphyschem.2022.110201. URL: <https://www.sciencedirect.com/science/article/pii/S0969806X22002432> (visited on 08/02/2023).
- [34] T. Trojek et al. "Confocal X-ray fluorescence spectrometer for in-situ analyses of paintings". In: *Radiation Physics and Chemistry*. Proceedings of the 13th International Symposium on Radiation Physics 137 (Aug. 1, 2017), pp. 238–242. ISSN: 0969-806X. DOI: 10.1016/j.radphyschem.2016.02.031. URL: <https://www.sciencedirect.com/science/article/pii/S0969806X16300743> (visited on 08/02/2023).
- [35] R. Prokeš et al. "Investigation of color layers of Bohemian panel paintings by confocal micro-XRF analysis". In: *Radiation Physics and Chemistry* 151 (Oct. 1, 2018), pp. 59–64. ISSN: 0969-806X. DOI: 10.1016/j.radphyschem.2018.05.006. URL: <https://www.sciencedirect.com/science/article/pii/S0969806X18300835> (visited on 08/02/2023).
- [36] K. Nakano et al. "Depth elemental imaging of forensic samples by confocal micro-XRF method". In: *Analytical Chemistry* 83.9 (2011), pp. 3477–3483. ISSN: 00032700. DOI: 10.1021/ac1033177.
- [37] T. Nakazawa and K. Tsuji. "Depth-selective elemental imaging of microSD card by confocal micro XRF analysis". In: *X-Ray Spectrometry* 42.3 (2013), pp. 123–127. ISSN: 00498246. DOI: 10.1002/xrs.2442.

- [38] K. Nakano et al. "Visualizing a black cat drawing hidden inside the painting by confocal micro-XRF analysis". In: *Microchemical Journal* 126 (May 1, 2016), pp. 496–500. ISSN: 0026-265X. DOI: 10.1016/j.microc.2016.01.007. URL: <https://www.sciencedirect.com/science/article/pii/S0026265X16000084> (visited on 08/03/2023).
- [39] K. Tsuji, T. Yonehara, and K. Nakano. "Application of confocal 3D micro-XRF for solid/liquid interface analysis". In: *Analytical Sciences: The International Journal of the Japan Society for Analytical Chemistry* 24.1 (Jan. 2008), pp. 99–103. ISSN: 0910-6340. DOI: 10.2116/analsci.24.99.
- [40] X. Ding, N. Gao, and G. J. Havrilla. "Monolithic polycapillary x-ray optics engineered to meet a wide range of applications". In: *Advances in Laboratory-based X-Ray Sources and Optics*. Advances in Laboratory-based X-Ray Sources and Optics. Vol. 4144. SPIE, Nov. 2, 2000, pp. 174–182. DOI: 10.1117/12.405891. URL: <https://www.spiedigitallibrary.org/conference-proceedings-of-spie/4144/0000/Monolithic-polycapillary-x-ray-optics-engineered-to-meet-a-wide/10.1117/12.405891.full> (visited on 08/02/2023).
- [41] X. Lin et al. "Characterization and applications of a new tabletop confocal micro X-ray fluorescence setup". In: *Nuclear Instruments and Methods in Physics Research Section B: Beam Interactions with Materials and Atoms* 266.11 (June 1, 2008), pp. 2638–2642. ISSN: 0168-583X. DOI: 10.1016/j.nimb.2007.12.064. URL: <https://www.sciencedirect.com/science/article/pii/S0168583X0701823X> (visited on 08/02/2023).
- [42] K. Janssens, K. Proost, and G. Falkenberg. "Confocal microscopic X-ray fluorescence at the HASYLAB microfocus beamline: characteristics and possibilities". In: *Spectrochimica Acta Part B: Atomic Spectroscopy*. 17th International Congress on X-Ray Optics and Microanalysis 59.10 (Oct. 8, 2004), pp. 1637–1645. ISSN: 0584-8547. DOI: 10.1016/j.sab.2004.07.025. URL: <https://www.sciencedirect.com/science/article/pii/S058485470400206X> (visited on 08/02/2023).
- [43] A. Woll et al. "Development of confocal X-ray fluorescence (XRF) microscopy at the Cornell high energy synchrotron source". In: *Applied Physics A* 83.2 (May 1, 2006), pp. 235–238. ISSN: 1432-0630. DOI: 10.1007/s00339-006-3513-4. URL: <https://doi.org/10.1007/s00339-006-3513-4> (visited on 08/02/2023).

- [44] I. Mantouvalou, W. Malzer, and B. Kanngießer. “Quantification for 3D micro X-ray fluorescence”. In: *Spectrochimica Acta - Part B Atomic Spectroscopy* 77 (2012), pp. 9–18. ISSN: 05848547. DOI: 10.1016/j.sab.2012.08.002.
- [45] I. Mantouvalou et al. “Reconstruction of confocal micro-x-ray fluorescence spectroscopy depth scans obtained with a laboratory setup”. In: *Analytical Chemistry* 86.19 (2014), pp. 9774–9780. ISSN: 15206882. DOI: 10.1021/ac502342t.
- [46] W. Malzer and B. Kanngießer. “A model for the confocal volume of 3D micro X-ray fluorescence spectrometer”. In: *Spectrochimica Acta Part B: Atomic Spectroscopy* 60.9 (2005), pp. 1334–1341. ISSN: 05848547. DOI: 10.1016/j.sab.2005.07.006. URL: <http://linkinghub.elsevier.com/retrieve/pii/S0584854705002107>.
- [47] F. Förste et al. “Quantification routines for full 3D elemental distributions of homogeneous and layered samples obtained with laboratory confocal micro XRF spectrometers”. In: *Journal of Analytical Atomic Spectrometry* 37.8 (2022), pp. 1687–1695. ISSN: 13645544. DOI: 10.1039/d2ja00119e.
- [48] M. Czyzycki, M. Bielewski, and M. Lankosz. “Quantitative elemental analysis of individual particles with the use of micro-beam X-ray fluorescence method and Monte Carlo simulation”. In: *X-Ray Spectrometry* 38.6 (2009), pp. 487–491. ISSN: 1097-4539. DOI: 10.1002/xrs.1203. URL: <https://onlinelibrary.wiley.com/doi/abs/10.1002/xrs.1203> (visited on 09/02/2023).
- [49] M. Czyzycki et al. “Monte Carlo simulation code for confocal 3D micro-beam X-ray fluorescence analysis of stratified materials”. In: *X-Ray Spectrometry* 40 (Mar. 1, 2011), pp. 88–95. DOI: 10.1002/xrs.1300.
- [50] M. Czyzycki et al. “The perspective of new multi-layer reference materials for confocal 3D micro X-ray fluorescence spectroscopy”. In: *X-Ray Spectrometry* 41.4 (2012), pp. 273–278. ISSN: 00498246. DOI: 10.1002/xrs.2395.
- [51] B. Golosio et al. “Monte Carlo simulation of X-ray imaging and spectroscopy experiments using quadric geometry and variance reduction techniques”. In: *Computer Physics Communications* 185.3 (Mar. 1, 2014), pp. 1044–1052. ISSN: 0010-4655. DOI: 10.1016/j.cpc.2013.10.034. URL: <https://www.sciencedirect.com/science/article/pii/S0010465513003834> (visited on 09/02/2023).

- [52] A. Brunetti and B. Golosio. "A new Monte Carlo code for simulation of the effect of irregular surfaces on X-ray spectra". In: *Spectrochimica Acta Part B: Atomic Spectroscopy* 94-95 (Apr. 1, 2014), pp. 58–62. ISSN: 0584-8547. DOI: 10.1016/j.sab.2014.03.007. URL: <https://www.sciencedirect.com/science/article/pii/S0584854714000366> (visited on 09/02/2023).
- [53] L. Vincze, K. Janssen, and F. Adams. "A general Monte Carlo simulation of energy-dispersive X-ray fluorescence spectrometers-I. Unpolarized radiation, homogeneous samples". In: *Spectrochimica Acta Part B: Atomic Spectroscopy* 48.4 (1993), pp. 553–573. ISSN: 05848547. DOI: 10.1016/0584-8547(93)80060-8.
- [54] L. Vincze et al. "A general Monte Carlo simulation of ED-XRF spectrometers. II: Polarized monochromatic radiation, homogeneous samples". In: *Spectrochimica Acta Part B: Atomic Spectroscopy* 50.2 (1995), pp. 127–147. ISSN: 05848547. DOI: 10.1016/0584-8547(94)00124-E.
- [55] L. Vincze et al. "A general Monte Carlo simulation of energy-dispersive X-ray fluorescence spectrometers. Part 3. Polarized polychromatic radiation, homogenous samples". In: *Spectrochim. Acta* 50 (1995), pp. 1481–1500. DOI: 10.1016/0584-8547(95)01361-X.
- [56] L. Vincze et al. "Monte Carlo simulation of X-ray fluorescence spectra: Part 4. Photon scattering at high X-ray energies". In: *Spectrochimica acta, Part B: Atomic spectroscopy* 54.12 (1999), pp. 1711–1722. ISSN: 05848547. DOI: 10.1016/S0584-8547(99)00094-4.
- [57] T. Schoonjans et al. "A general Monte Carlo simulation of energy dispersive X-ray fluorescence spectrometers - Part 5: Polarized radiation, stratified samples, cascade effects, M-lines". In: *Spectrochimica Acta - Part B Atomic Spectroscopy* 70 (2012). Publisher: Elsevier B.V., pp. 10–23. ISSN: 05848547. DOI: 10.1016/j.sab.2012.03.011. URL: <http://dx.doi.org/10.1016/j.sab.2012.03.011>.
- [58] T. Schoonjans et al. "A general Monte Carlo simulation of energy-dispersive X-ray fluorescence spectrometers - Part 6. Quantification through iterative simulations". In: *Spectrochimica Acta - Part B Atomic Spectroscopy* 82 (2013). Publisher: Elsevier B.V., pp. 36–41. ISSN: 05848547. DOI: 10.1016/j.sab.2012.12.011. URL: <http://dx.doi.org/10.1016/j.sab.2012.12.011>.

- [59] P. Van Espen, K. Janssens, and J. Nobels. "AXIL-PC, software for the analysis of complex X-ray spectra". In: *Chemometrics and Intelligent Laboratory Systems* 1.1 (Nov. 1, 1986), pp. 109–114. ISSN: 0169-7439. DOI: 10.1016/0169-7439(86)80031-4. URL: <https://www.sciencedirect.com/science/article/pii/0169743986800314> (visited on 08/03/2023).
- [60] V. a. Solé et al. "A multiplatform code for the analysis of energy-dispersive X-ray fluorescence spectra". In: *Spectrochimica Acta Part B: Atomic Spectroscopy* 62.1 (2007). ISBN: 05848547, pp. 63–68. ISSN: 05848547. DOI: 10.1016/j.sab.2006.12.002. URL: <http://linkinghub.elsevier.com/retrieve/pii/S0584854706003764>.
- [61] M. Iro et al. "voxTrace: A voxel-based Monte-Carlo ray-tracing code for the simulation of X-ray fluorescence spectra". In: *SoftwareX* (July 25, 2023), p. 101481. ISSN: 2352-7110. DOI: 10.1016/j.softx.2023.101481. URL: <https://www.sciencedirect.com/science/article/pii/S2352711023001772> (visited on 07/25/2023).
- [62] M. Sanchez Del Rio et al. "SHADOW3: A new version of the synchrotron X-ray optics modelling package". In: *Journal of Synchrotron Radiation* 18.5 (2011). Publisher: International Union of Crystallography, pp. 708–716. ISSN: 09090495. DOI: 10.1107/S0909049511026306.
- [63] M. Iro et al. "Investigation of polycapillary half lenses for quantitative confocal micro-X-ray fluorescence analysis". In: *Journal of Synchrotron Radiation* 29.6 (2022). Publisher: International Union of Crystallography, pp. 1376–1384. ISSN: 16005775. DOI: 10.1107/s1600577522009699.
- [64] C. Sanderson and R. Curtin. "Armadillo: a template-based C++ library for linear algebra". In: *Journal of Open Source Software* 1.2 (June 10, 2016), p. 26. ISSN: 2475-9066. DOI: 10.21105/joss.00026. URL: <https://joss.theoj.org/papers/10.21105/joss.00026> (visited on 09/02/2023).
- [65] D. Ingerle et al. "A monochromatic confocal micro-x-ray fluorescence (XRF) spectrometer for the lab". In: *Review of Scientific Instruments* 91.12 (2020). Publisher: AIP Publishing, LLC. ISSN: 10897623. DOI: 10.1063/5.0028830. URL: <https://doi.org/10.1063/5.0028830>.
- [66] K. Tsuji and K. Nakano. "Development of a new confocal 3D-XRF instrument with an X-ray tube". In: *Journal of Analytical Atomic Spectrometry* 26.2 (2011), p. 305. ISSN: 0267-9477. DOI: 10.1039/c0ja00138d. URL: <http://xlink.rsc.org/?DOI=c0ja00138d> (visited on 10/15/2013).

- [67] M. Nakae et al. "Mathematical considerations for evaluating X-ray beam size in micro-XRF analysis". In: *X-Ray Spectrometry* n/a (n/a). ISSN: 1097-4539. DOI: 10.1002/xrs.3325. URL: <https://onlinelibrary.wiley.com/doi/abs/10.1002/xrs.3325> (visited on 07/13/2023).
- [68] I. Wolfram Research. *Mathematica*. Version 12.1. 2019. URL: <https://www.wolfram.com/mathematica>.
- [69] J. Schindelin et al. "Fiji: An open-source platform for biological-image analysis". In: *Nature Methods* 9.7 (2012), pp. 676–682. ISSN: 15487091. DOI: 10.1038/nmeth.2019.
- [70] P. Virtanen et al. "SciPy 1.0: fundamental algorithms for scientific computing in Python". In: *Nature Methods* 17.3 (2020), pp. 261–272. ISSN: 15487105. DOI: 10.1038/s41592-019-0686-2. arXiv: 1907.10121.
- [71] C. A. MacDonald. "Focusing polycapillary optics and their applications". In: *X-Ray Optics and Instrumentation* 2010.1 (2010), p. 17. ISSN: 16877632. DOI: 10.1155/2010/867049.
- [72] R. R. Curtin et al. *The ensmallen library for flexible numerical optimization*. Aug. 29, 2021. DOI: 10.48550/arXiv.2108.12981. arXiv: 2108.12981 [cs, math]. URL: <http://arxiv.org/abs/2108.12981> (visited on 09/02/2023).